Chair of Thermal Processing Technology

Master's Thesis

Phosphorus behaviour during carbo-thermal reduction of iron-, chromium-, and manganese-rich slags

Christoph Gatschlhofer, BSc

May 2022

MONTANUNIVERSITÄT LEOBEN
www.unileoben.ac.at

EIDESSTATTLICHE ERKLÄRUNG

Ich erkläre an Eides statt, dass ich diese Arbeit selbständig verfasst, andere als die angegebenen Quellen und Hilfsmittel nicht benutzt, und mich auch sonst keiner unerlaubten Hilfsmittel bedient habe.

Ich erkläre, dass ich die Richtlinien des Senats der Montanuniversität Leoben zu "Gute wissenschaftliche Praxis" gelesen, verstanden und befolgt habe.

Weiters erkläre ich, dass die elektronische und gedruckte Version der eingereichten wissenschaftlichen Abschlussarbeit formal und inhaltlich identisch sind.

Datum 17.05.2022

Unterschrift Verfasser/in
Christoph Gatschlhofer

LEHRSTUHL FÜR THERMOPROZESSTECHNIK
Lehrstuhlleiter:
Univ.Prof. Dipl.-Ing. Dr.techn. Harald Raupenstrauch
Montanuniversität Leoben
Franz-Josef-Strasse 18
A-8700 Leoben
www.unileoben.ac.at

Master's Thesis

Phosphorus behaviour during carbo-thermal reduction of iron-, chromium-, and manganese-rich slags

compiled by

Chair of Thermal Processing Technology

Submitted by:
Christoph Gatschlhofer, BSc
01235025

Supervisor:
Dipl.-Ing. Dr. mont. Klaus Doschek-Held
Univ. Prof. Dipl.-Ing. Dr. techn. Harald Raupenstrauch

Leoben, 25.05.2022

Acknowledgement

First, I would like to thank both of my supervisors, Christoph Ponak at the beginning and Klaus Doschek-Held at the end, for their assistance during the preparation of this master thesis. They were always supportive on a professional level and coincidently create a pleasant work environment with their openness and cordial manner.

Special thanks go to Prof. Harald Raupenstrauch for welcoming me in his open-hearted team. From the beginning I felt very well integrated – this circumstance is not a matter of course for me! I owe this particularly to all members of the Chair of Thermal Processing Technology. Nevertheless, I would like to emphasize Alexandra Holzer, Stefan Windisch-Kern, Lukas Wiszniewski, Wolfgang Reiter, and Valentin Mally: Thank you for your open ear, the constructive discussions, and the uncomplicated admission into your workgroup.

In my family environment I would like to thank my parents, Karin, and Helmut in terms of all the little things in daily life, you had taken from me, but also for the constant support in more difficult situations. Furthermore, I would also give thanks to my siblings, Hannes, Elvira, and Michael. Finally, I want to thank my other half, my girlfriend Maria for the patience, strength, and motivation she gave me in every moment of this challenging time.

Danksagung

Zuerst möchte ich mich bei meinen beiden Betreuern, zu Beginn Christoph Ponak und abschließend Klaus Doschek-Held für die stetige Unterstützung bei der Erstellung dieser Masterarbeit bedanken. Ihr wart nicht nur auf fachlicher Ebene kompetent, sondern habt auch stets auf menschlicher Ebene mit eurer Offenheit und den herzlichen Umgang ein angenehmes Arbeitsklima geschaffen.

Besonderer Dank kommt Prof. Harald Raupenstrauch für die Aufnahme in sein Team zu. Von Beginn an fühlte ich mich bei der Bewältigung der Aufgaben gut aufgehoben – dieser Umstand stellt für mich keine Selbstverständlichkeit dar! Dies habe ich vor allem den Kolleginnen und Kollegen des Lehrstuhls für Thermoprozesstechnik zu verdanken. Hervorheben möchte ich Alexandra Holzer, Stefan Windisch-Kern, Lukas Wiszniewski, Wolfgang Reiter und Valentin Mally: Danke für euer offenes Ohr, den konstruktiven Diskussionen und die unkomplizierte Eingliederung in die Arbeitsgruppe.

In meinem familiären Umfeld möchte ich meiner Mutter Karin und meinem Vater Helmut neben den unerlässlich kleinen Dinge im Leben, die ihr mir abgenommen habt, aber auch für den stetigen Rückhalt in schwierigeren Zeiten danken. Dank gebührt auch meinen Geschwistern Hannes, Elvira und Michael. Zu guter Letzt danke ich meiner besseren Hälfte, meiner Freundin Maria, für Geduld, Kraft und Motivation die sie mir in jedem Moment dieser herausfordernden Zeit gespendet hat.

Funding

The author gratefully acknowledges any financial support of each project partner, which generally enabled the creation of this master thesis. This work was funded in the course of the Austrian Competence Centre Programme of the "Competence Centre for Excellent Technologies in Advanced Metallurgical and Environmental Process Development" (COMET K1-MET) which is funded from the Federal Ministry for Climate Protection, Environment, Energy, Mobility, Innovation and Technology (BMK), the Federal Ministry for Digitalization and Economic Affairs (BMDW), the provinces of Upper Austria, Styria and Tyrol, as well as the Styrian Business Promotion Agency (SFG). In addition to funding from the COMET programme of the K1-MET GmbH, additional financial support comes from the Montanuniversitaet Leoben and industrial partners such as Primetals Technologies Austria GmbH, SCHOLZ Austria GmbH, voestalpine Stahl GmbH, and voestalpine Stahl Donawitz GmbH.

Förderung

Der Autor dankt grundsätzlich allen Projektpartnern für jegliche finanzielle Unterstützung, die die Erstellung dieser Arbeit überhaupt ermöglicht hat. Diese Arbeit wurde im Zuge des österreichischen Kompetenzzentren-Programms der „Competence Center for Excellent Technologies in Advanced Metallurgical and Environmental Process Development“ (COMET K1-MET) mit Mitteln des Bundesministeriums für Klimaschutz, Umwelt, Energie, Mobilität, Innovation und Technologie (BMK), des Bundesministeriums für Digitalisierung und Wirtschaftsstandort (BMDW), der Länder Oberösterreich, Steiermark und Tirol, sowie der steirischen Wirtschaftsförderung (SFG) gefördert. Neben der Finanzierung durch das COMET Programm der K1-MET GmbH kommen zusätzliche finanzielle Mittel von der Montanuniversität Leoben, sowie den Industriepartnern Primetals Technologies Austria GmbH, SCHOLZ Austria GmbH, voestalpine Stahl GmbH und voestalpine Stahl Donawitz GmbH.

Kurzfassung:

Trotz der andauernden Covid-19 Pandemie wurden 2020 auf globaler Ebene mit 1878 Mt produziertem Rohstahl ein erneuter historischer Höchstwert erzielt. Dabei entfielen 73.2% auf die konventionelle Hochofen/Konverter Route. Während des Frischens im Konverter werden unerwünschte Begleitelementen wie Schwefel, Phosphor und Silizium aus dem Roheisen entfernt. Außerdem werden beträchtliche Mengen an wertvollen Metallen wie Eisen, Chrom und Mangan oxidiert und ebenso in eine Calcium-Silikat-Schlacke, der sogenannten LD-Schlacke, eingebunden. Die erheblichen Mengen an jährlich produziertem Rohstahl, mit einer Schlackenrate von 100 – 150 kg pro Tonne im Konverter, zeigt eindrucksvoll das enorme Potential an wiederverwertbaren Schlackenkomponenten auf. Die anfallenden Mengen an LD-Schlacke sollten im Zuge einer effizienten Kreislaufwirtschaft einer entsprechenden Behandlung zugeführt werden, um die darin oxidisch gebundenen Wertmetalle wieder verfügbar zu machen. Eine Möglichkeit zur Wertmetallrückgewinnung von LD-Schlacke wäre der Weg über einen pyrometallurgischen Prozessschritt mittels carbo-thermischer Reduktion. Dabei stellt die Affinität zwischen hochreaktivem gasförmigem Phosphor und reduzierten Metallen unter Bildung unerwünschter Phosphide die größte Herausforderung dar, da sie die Möglichkeit der Wiederverwertung einschränken.

Neben dem Eisenanteil in der LD-Schlacke spielen für den Bildungsmechanismus von Phosphiden während der carbo-thermischen Behandlung auch Metalle wie Chrom und Mangan eine wesentliche Rolle. Um die Phosphidbildung in Abhängigkeit unterschiedlicher Metallkonzentrationen von Eisen, Chrom oder Mangan in LD-Schlacke besser zu verstehen, werden in dieser Arbeit Ergebnisse aus Reduktionsversuchen dargelegt. Schlacken derartiger Zusammensetzung sind nicht verfügbar. Deshalb wurden als Ausgangsmaterial in einem MgO-Tiegel Proben phosphorreicher Calcium-Silikat-Schlacke mit einer Basizität von $B_2 = 1.4$ synthetisch hergestellt. Dazu dienen insgesamt sechs Proben von jeweils niedriger (4 m.-%) und hoher Konzentration (17 m.-%) von Eisen, Chrom oder Mangan. Anschließend wurden die Schlacken mithilfe von Kohlenstoffpulver in einem MgO-Tiegel bei 1873 K unter Inertgas carbo-thermisch reduziert. Die Ergebnisse unterstreichen die Komplexität der carbo-thermischen Behandlung von Schlacke. Alle Proben mit geringen Gehalten von Eisen, Chrom oder Mangan konnten nicht reduziert werden. Bei jenen Proben mit hoher Konzentration ist das unterschiedliche Verhalten von Eisen, Chrom und Mangan erkennbar. Damit wurde für weiterführende Untersuchungen die Basis zur Versuchsoptimierung gelegt. Letztlich sollen Schlackenmischungen für die carbo-thermische Behandlung identifiziert werden, die den Austrag von gasförmigem Phosphor maximieren, um gleichzeitig ein möglichst phosphorfreies Metallprodukt rückzugewinnen.

Abstract:

Despite the Covid-19 pandemic steelmaking in 2020 climbs up again to an anew production maximum with a volume of 1878 Mt crude steel. Therefrom 73.2% can be attributed to the production via the blast furnace/basic oxygen furnace route. During the refining step in the converter unwanted steel-constituents such as sulphur, phosphorus, and silicon are transferred in their oxidic state into a calcium-silicate-slag, better known as basic oxygen furnace slag. Inevitably metal oxides of iron, chromium, and manganese are also incorporated to a large extent into the converter slag during refining. The considerable annual quantities of crude steel, for which 100 – 150 kg of basic oxygen furnace slag accumulates for each tonne produced, demonstrate the enormous potential of recyclable valuable slag-components. In the light of a zero-waste steel production towards an efficient circular economy further processing steps for the converter slag valorisation are recommendable. The slag should be separated into different usable fractions by returning each stream to a suitable reuse possibility with defined product qualities to competitive market prices. One approach for the treatment of basic oxygen furnace slag can be pyrometallurgical high temperature reduction. The main challenge of this method poses the affinity between highly reactive gaseous phosphorus, and metals, resulting in the formation of unwanted phosphide species, which restricted the reuse possibilities of converter slag.

In addition to the iron content in the basic oxygen furnace slag, metals such as chromium and manganese are also involved in the formation mechanism of phosphides during carbo-thermal treatment. As a result, this thesis deals with the outcome of an executed carbo-thermal reduction experiment. Since slag mixtures with such compositions are not available, slag samples with a basicity $B_2 = 1.4$ of lower (4 m.-%) and higher (17 m-%) metal concentrations of either iron, chromium, or manganese need to be produced synthetically. Subsequently, all slag samples are processed in MgO-crucibles with the help of fine carbon powder by carbo-thermal reduction at 1873 K under inert gas. The results emphasize the complexity behind carbo-thermal treatment of a multi-component system such as slag. All samples with lower metal-content of iron, chromium, or manganese couldn’t be reduced at all. For high concentrated slag samples, a characteristic behaviour for iron, chromium, and manganese can be determined. However, the results serve as a firm basis for the optimization of follow-up experiments. The final objective results in the identification of suitable slag-mixtures for carbo-thermal treatment in order to maximize the phosphorus gasification by simultaneously minimize the phosphide content in the obtained metal product.

Table of contents

Lists of abbreviations, formulae, and symbols

General Abbreviations

BF	Blast furnace
BFS	Blast furnace slag
BOF	Basic oxygen furnace
BOFS	Basic oxygen furnace slag
EAF	Electric arc furnace
DRM	Degree of reduced metal
cf.	Latin: confer/conferatur
EU	European Union
EF	Elevator furnace
HM	Heating microscope
ICP-OES	Inductively coupled plasma optical emission spectrometry
LD	Linz-Donawitz
ME	Metal phase
MG	Metallisation grade
MI	Mineral phase
MUL	Montanuniversitaet Leoben

PGD	Phosphorus gasification degree
RD	Reduction degree
SR	Stochiometric ratio
SEM	Scanning electron microscope
TC	Thermocouple
TPT	Thermal Processing Technology
XRD	X-ray diffraction
XRF	X-ray fluorescence analysis

Chemical formulae

Fe	Iron
Cr	Chromium
Mn	Manganese
P	Phosphorus
S	Sulphur
Si	Silicon
Mg	Magnesium
Ca	Calcium
F	Fluorine
C	Carbon
V	Vanadium
Cu	Copper
Pb	Lead
Ar	Argon
O^{2-}	Oxygen ion
PO_4^{3-}	Phosphate ion
P^{3-}	Phosphide ion

Formulae symbols

$B_{2,3,4}$	Basicity
L_P	De-Phosorisation coefficient
K	Chemical equilibrium
p_i	Partial pressure of component i
a_i	Activity of component i
γ_i	Activity coefficient of component i
x_i	Concentration of component i
m.-%	Weight percentage
ΔG	Free Gibb's energy
ΔG^0	Free Gibb's energy at standard conditions
p^0	Pressure at standard conditions
ΔH^0	Enthalpy change at standard conditions
ΔS^0	Entropy change at standard conditions
γ_i^0	Henrian coefficient of component i

Aggregate state and phase indication

(g)	Gaseous state
(l)	Liquid state
(s)	Solid state
{ }	Gaseous phase
[ ]	Molten bath (dissolved in liquid metal phase)
( )	Slag phase

C	CaO
S	SiO_2
F	FeO
P	P_2O_5
C_2S	$2CaO \cdot SiO_2$ (Ca_2SiO_4)
C_3S	$3CaO \cdot SiO_2$ (Ca_3SiO_5)
C_3P	$3CaO \cdot P_2O_5$ ($Ca_3(PO_4)_2$)
F_3P	$3FeO \cdot P_2O_5$ ($Fe_3(PO_4)_2$)

List of illustrations

List of tables

1 Challenge outline

Iron and steel are one of the main drivers for the global economy. Due to the various properties of steel, it is a suitable material for a large variety of applications, e.g., in the fields of construction, agriculture, energy infrastructure, machines, medicine, and in households amongst others. [1] Especially in recent years, a rapid growth of the annual global crude steel production is noticeable and can be illustrated in Figure 1, which has increased almost tenfold over the past 70 years. Since the beginning of this century, the development has even intensified due to China's rising presence in the global steel market. [1,2]

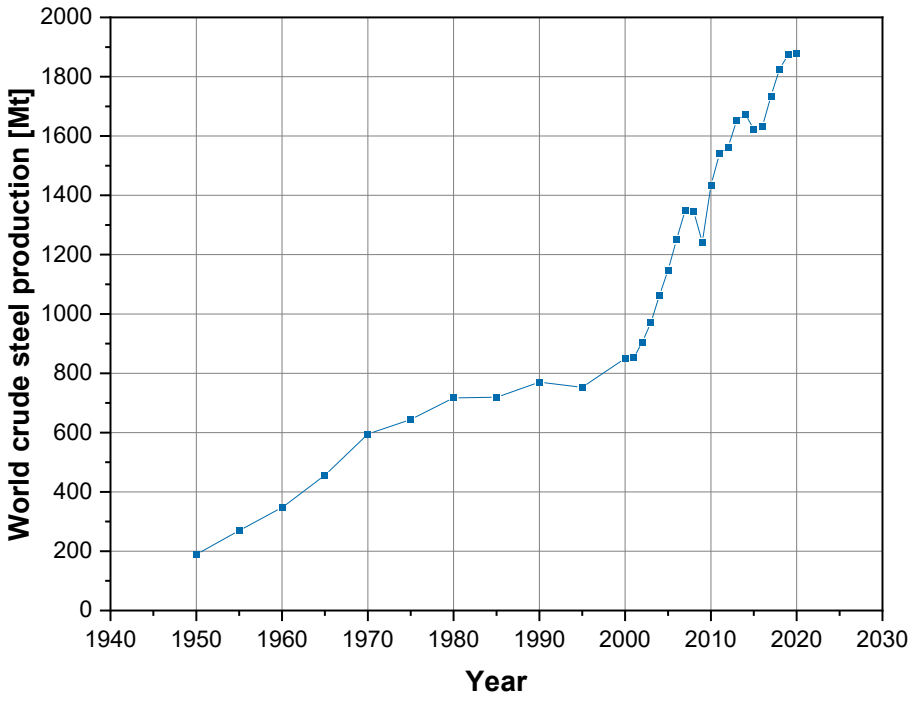

Figure 1: World crude steel production from 1950 – 2020, cf. [2]

Figure 2 impressively show the global amount of produced crude steel in 2020 divided into regions and related allocation in million tonnes [Mt] mainly to the two dominant main routes of steelmaking, which are the blast furnace (BF)/basic oxygen furnace (BOF) route and the method via the electric arc furnace (EAF). With a total of 1388.7 Mt, Asia is responsible for 74% of the whole global crude steel production, whereas the European Union contributes merely 7.4%, with an additional involvement of CIS-countries and other European countries including Turkey does not exceed 14.8%. While in Europe, Asia, Australia, South, and Central America the BF/BOF route is dominant, North America, Middle East, and Africa rely on the manufacturing in an EAF. Nevertheless, the world-wide leading steel production route with 73.2 % is still the reduction of iron ore in a BF and subsequent refining in the BOF. This explicitly expose the current and near future relevance of steelmaking via the converter and the associated accumulation of by-products, which in turn requires a convenient processing and a subsequent supply to an appropriate utilisation. [2]

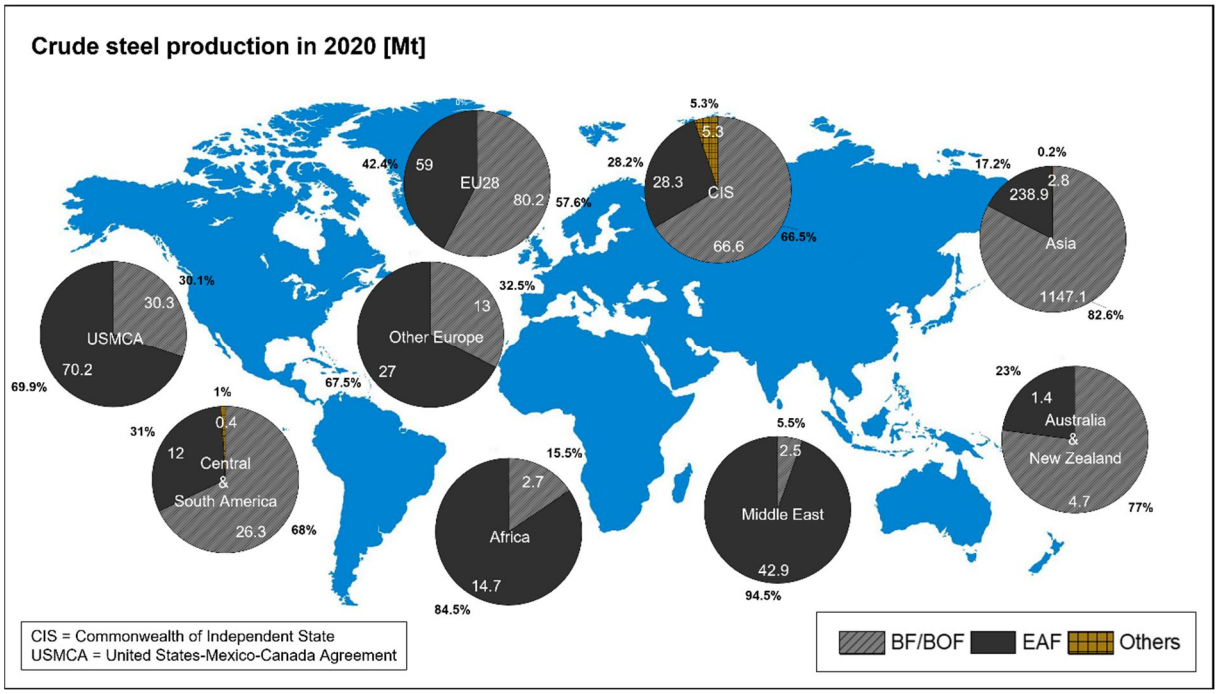

Figure 2: World crude steel production – allocation of production routes by regions, cf. [2]

Based on a significant energy demand combined with a prevalent share of fossil fuels in the supplied energy mix, the steel industry emits large amounts of climate-effective emissions. 2.18 tonnes of CO_2 are released per tonne crude steel produced during the BF/BOF route. Steel manufacturers generally face challenging times because of growing pressure regarding societal, environmental, and legislative aspects. Aside from limiting greenhouse gas emissions, circular economy is also becoming increasingly crucial in climate protection.

However, it should be mentioned that great efforts have already been made by the steel plant operators, especially in the past decades. For example, the implementation of an emission monitoring and management measures of accrued greenhouse gases is already mandatory. Furthermore, in relation to circular economy, solely 650 Mt of recycled steel is already fed back to the manufacturing process in 2016, saving 900 Mt CO_2 emissions. Considering the amount of weight, steel is by far the most recycled material worldwide. [3–5]

In the last 50 years, the weight of steel products could be partially saved up to 40%. Referring to one tonne of steel, this results in a significant decrease of raw material- and energy demand for their production. Concretely, with the help of sophisticated steel products lighter consumer goods can be produced and hence less energy is consumed along their entire operating lifetime resulting in additional hidden CO_2 savings. In 2016, merely 40% of energy is required for each produced tonne of steel compared to 1960, with reported energy savings of 24 GJ/t. In 2014 a mean of 18.7 GJ/t (15.8 GJ/t – 22.8 GJ/t) of cast steel for the BF/BOF route and between 5.3 – 8.7 GJ/t via the production of steel feeding 100% scrap into an EAF were needed on a global-scale. However, despite the reduction of greenhouse gas emissions in terms of technological advances, this effect is compensated by the simultaneous rapid increase of steel demand. [3,4]

By pursuing the way steel is doing either from iron ore reduction in a BF, refining the emerging pig iron in a BOF or melting scrap in an EAF in order to obtain crude steel, various by-products such as slag, sludge, dust, and gases are generated substantially. Regarding their accumulation, slag is by far the most common one, which makes up 90% of the total mass, depicted for both main routes of steelmaking in Figure 3. [3,4,6,7]

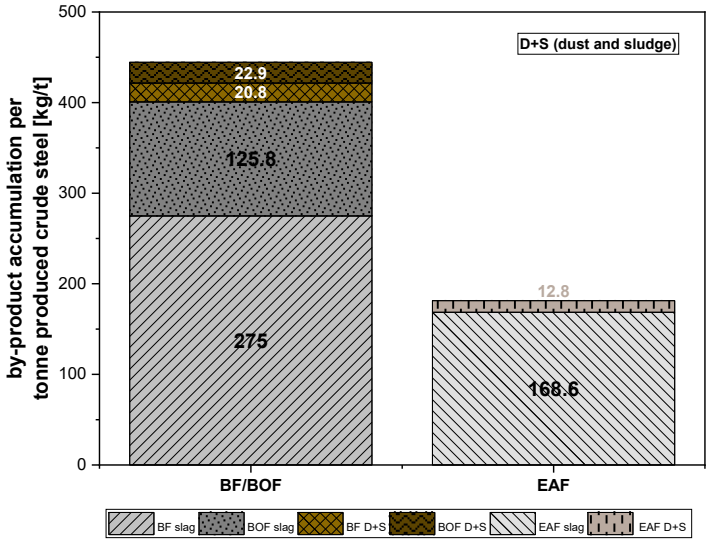

Figure 3: Comparison of by-product accumulation including slag, dust, and sludge between the two main crude steel production routes: BF/BOF and EAF, cf. [3]

While slag from ironmaking is almost completely recovered, the percentage of reused steelmaking slag is around 80%. Innovative technology developments and synergies with other industries have vastly enhanced the recovery rate during the last second decades. Hence, the way to a zero-waste steel industry in agreement with legislation requires highest material efficiency and quality criteria to avoid landfilling, keep by-products in continuous loops, and identify proper reuse possibilities. For this reason, by-products can be either utilized in the steelworks internally or sold to different fields of industries, fostering partnerships and synergies. [3,4,6,7]

The residue of interest in the course of this thesis is slag from the BOF, which is formed in the refining step of the most widely used way of steel production – the BF/BOF route. Slag generally fulfils vital functions during steelmaking. One of them is the so-called dephosphorisation process – the integration of phosphorus into the slag. Apart from minor special applications, phosphorus in crude steel is highly undesirable because it affects steel properties adversely. Besides the typical slag forming compounds and impurities like phosphorus and sulphur, slag also takes up considerable amounts of valuable metals. However, due to growing prize pressure in the steel industry an increasing application of less noble iron ore sources and diminishing coal quality can be expected. This, in turn leads to the fact that higher rates of phosphorus enter the BF, posing higher requirements to the dephosphorisation-process during the refining step in the BOF. [6,8–10] Concerning the composition of slag from the converter, a high potential of reusable metal contents can be identified. Furthermore, the non-metal-containing slag is ideally applicable in the construction sector as binder. Although only minor amounts of phosphorus are bound into the converter slag, giant masses of slag accumulate annually, revealing an enormous recycling-potential even for this utterly critical element phosphorus. For an enhanced recovery rate of by-products from the steel industry, combined with an efficient re-use, it will be necessary to split up the slag into different fractions, keeping them in closed material-loops - either internally or by creating synergies with respective industry branches.

1.1 Motivation and research relevance

Considering that around 73% of the total crude steel production (1878 Mt) is originated from the BF/BOF route, approximately 400 kg slag for each produced tonne of crude steel is generated. [2,6] Thereof, between 100 – 150 kg accounts for slag from the refining step in the converter. That represents the substantial amounts of reusable materials and highlights their massive potential. [6] However, the limitation of slag-reuse applications can be attributed to

tightened legislation, which means that at the moment a lot more slag is produced than recycled. [11]

Besides slag formers and undesired impurities, basic oxygen furnace slag (BOFS) consists of high amounts of valuable metals. [5,12] Integrated recycling of BOFS within the steelworks is unfavourable because of an accumulation of phosphorus along the production route of crude steel. [13] For this purpose, the Chair of Thermal Processing Technology (TPT) at the Montanuniversitaet Leoben (MUL) has succeeded in developing the so-called InduRed reactor, which can meet the challenges of pyrometallurgical treatment of BOFS. This process enables an almost entire separation of BOFS into an almost metal-free slag-phase and a metal-phase. Additionally, a heat-value-rich gas phase containing gaseous phosphorus can be separated, reaching high phosphorus gasification degrees. [14]

Phosphate rock and phosphorus are listed with 30 other materials by the European Union (EU) as critical raw materials assessed by the relation between their supply risk and economic importance. The InduRed process could also potentially contribute to diminishing the European dependency on phosphate rock imports. [15] In general, during high-temperature reduction process of BOFS, phosphides tend to be formed as soon as gaseous phosphorus gets in contact with liquid iron. [13] On the other hand, for a preferably high internal reuse of the metal phase, the formation of phosphides needs to be oppressed. First, it was assumed that only iron plays a significant role in the undesired phosphide formation. However, results from respective literature indicate that manganese and chromium also significantly reduce the gasification rate of phosphorus. [14] For a total and efficient utilization of BOFS it is therefore of utmost importance to understand the interaction behaviour between phosphorus and certain species during pyrometallurgical treatment.

1.2 Research objective and assumptions related to this work

This work aims for a better understanding of high-temperature reduction treatment of phosphorus-containing slags. The emphasis is set on the phosphide formation behaviour between phosphorus (P) and metals like iron (Fe), chromium (Cr), and manganese (Mn). Thus, each of six synthetic slag samples, composing of typical slag constituents and characteristic amounts of either Fe, Cr, or Mn are produced, which eliminates the disruptive influence of other metals. Then all mixtures are examined after carbo-thermal reduction experiments. Altogether, three samples with high metal concentrations (Fe_{high}, $Mn_{high,}$ and Cr_{high}) and three samples with lower amounts (Fe_{low}, $Mn_{low,}$ and Cr_{low}) were investigated. The basicity (B_2 – see

Equation 2-6 in chapter 2.3.1) and ratios between slag forming components are kept constant. Afterwards, the phosphorus distribution between emerging slag- and metal-phase can be evaluated to ascertain which metal shows the highest affinity to phosphorus under the same conditions. Compared to theoretical outcomes obtained from the literature, it can be determined if the gained experimental results are in accordance with the derived assumptions made below:

- Higher amounts of iron, chromium, or manganese in the synthesised initial slag are expressed in a lower De-Phosphorisation coefficient L_P after carbo-thermal treatment at 1873 K: $L_P(Fe, Cr, Mn)_{high} < L_P(Fe, Cr, Mn)_{low}$.
- Iron, and chromium show a stronger affinity to phosphorus, compared to that of manganese, which results in the following De-Phosphorisation coefficient sequence after carbo-thermal treatment at 1873 K: $L_P(Fe)$ and $L_P(Cr) < L_P(Mn)$.
- The evaluation of the present slag samples concerning the relevant temperature range, chemical aspects, and thermodynamic considerations, implies that the following phosphides are most likely to be formed: Fe_2P, $Cr_{12}P_7$, and Mn_3P_2.

1.3 Methodology

For an adequate experimental design, and the choice of eligible experimental parameters relevant knowledge must be gained. For this reason, appropriate literature covering the issues related to the processing of BOFS with associated challenges is studied. Therefore, the results of an extensive literature research are first exposed in the theoretical fundamentals of chapter 2. This includes general and detailed findings of BOFS with special attention on the accompanying difficulties of carbo-thermal treatment of phosphorus-containing slags. Furthermore, especially at the end of theoretical fundamentals this thesis is primarily based on important outcomes of recent research work.

The following practical part comprises the description, execution, and results from a smelting and a reduction experiment, simultaneously processing six samples. In a first step, Fe-, Cr- and Mn-rich slags are produced synthetically. Afterwards, they are reduced with carbon as a reductant at a maximum temperature of 1873 K. Outcomes will give a better insight into the behaviour between phosphorus and metals like Fe, Cr, or Mn. The experimental setup and obtained results are compared with findings from literature, and possible deviations are interpreted and discussed, which can be found in chapter 3.

2 Theoretical fundamentals

In the following chapter, fundamental theoretical principles relevant to the course of this thesis are elaborated. Based on extensive literature research, a comprehensive insight into occurring issues around the processing of BOFS with particular emphasis on the behaviour of phosphorus should reveal the urgent need for a technical solution in this field.

In the beginning, the main routes of crude steel production are introduced, focusing on the BF/BOF route. Enormous amounts of emerging slag and included mass streams of valuable elements will be supported with the aid of meaningful figures. To understand the slag origination process inside the BOF this process is covered, and the inclusion process of phosphorus into the slag during the refining step is highlighted. Furthermore, utilisation possibilities and associated issues are also described in this sub-chapter. Subsequently, thermodynamic basics relevant for a further understanding are given.

The primary purpose of this thesis is to deal with difficulties related to the treatment of BOFS, aiming at a separation into reusable fractions by minimizing waste accumulation. Due to the interaction between phosphorus and slag constituents, restrictions of recyclability are among the critical challenges in slag processing. For this reason, a highly innovative method for the carbo-thermal treatment, which can meet the indicated requirements, was developed at the Chair of TPT at the MUL. In addition to that, BOFS, amongst other different residues, can be treated in a high-temperature process, which is introduced afterwards.

A lot of attention must be paid to the influence of specific slag components on the behaviour of phosphorus during reduction under high temperatures. Unwanted phosphide formation was first assumed to occur only between iron and phosphorus. However, literature already states that other metals like chromium or manganese are suspected of being involved in reaction processes with phosphorus. Results of prior literature concerning simulations carried out in FactSage™ should support these findings and are summarized at the end of this chapter. Finally, required assumptions for the followed practical part are derived and formulated.

2.1 Production of crude steel

No steel without slag – slag inevitably occurs during steel production and fulfils vital functions for steelmaking. The relevance of steel products can be emphasised regarding their formidable amounts produced each year. Therefore, this chapter devotes attention to numbers and figures of steelmaking and should give an overview of the main production routes of crude steel.

In 2020, a new maximum amount of 1878 Mt of crude steel was reached with China being the largest steel-producer (1064,8 Mt) followed by India (100,3 Mt) and Japan (83,2 Mt). Austria is listed on 25th place with a quantity of 6.8 Mt. Since the beginning of the Covid-19 pandemic, steelmaking generally was declining in most countries. However, despite economic impairments, few excepted countries could increase their production volume between 2019 and 2020. The flagship for this trend is China, which is almost solely accountable, boosting their production by 69.4 Mt. Consequently, despite the pandemic, China guaranteed an all-time high of produced crude steel in 2020. [2] The four main routes for crude steel production are given in Figure 4.

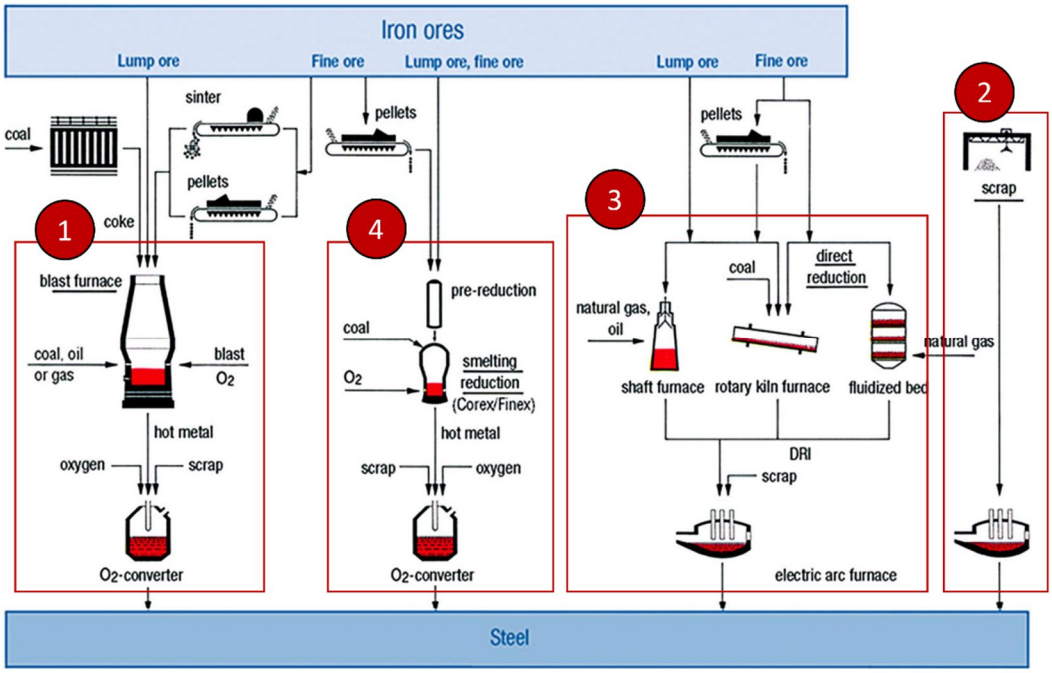

Figure 4: Crude steel production methods – (**1**) BF/BOF route, (**2**) EAF route, (**3**) direct reduction, and (**4**) smelting reduction, cf. [16]

By far, the highest amount of steel is produced through the BF/BOF route (**1**). On average, to produce 1000 kg steel via this route, raw materials including iron ore (1370 kg), coal

(780 kg), limestone (270 kg) and recycled steel (125 kg) are needed. Crude steel can also be made by smelting scrap in an electric arc furnace, while for this way, 710 kg of recycled steel, 586 kg of iron ore, 150 kg of coal, 88 kg of limestone and 2.3 GJ of electricity are required to produce 1000 kg of steel (**2**). Furthermore, direct reduction (**3**) and smelting reduction (**4**), the last two mentioned main steelmaking routes, generally play a minor role in the global steel market. In 2020, 73.2% of the total global crude steel production can be attributed to the BF/BOF route, and 26.3% is produced via the EAF. [1,2,17]

2.2 Basic oxygen furnace

This thesis deals with the treatment of slag originating from the refining step of the BOF. Therefore, this unit is explained in this chapter. The carbon-rich molten pig iron produced from the BF contains undesirable impurities like silicon (Si), manganese, sulphur (S), and phosphorus (P). To ensure a defined steel quality, these elements must be removed in a further process step. For this purpose, a refining of the hot metal is required in a BOF, which aims to remove undesired constituents through oxidation. The Linz-Donawitz (LD) process is the most widely used method, in which pure oxygen is blown through a lance onto the molten bath, reduces the carbon content and binds unwanted elements into an emerging slag phase. Exothermic oxidation reactions supply enough energy to maintain high temperatures ranging between 1873 – 1923 K, which are needed for chemical reactions depicted in Table 1, which means that no external heat input is necessary. [1]

Table 1: Main chemical reactions during the oxidation process in a BOF, cf. [1]

Oxidation process	Chemical reaction
Carbon elimination	$[C] + [O] \leftrightarrows \{CO\}$
	$[CO] + [O] \leftrightarrows \{CO_2\}$
Oxidation of accompanying and trace elements	
▪ Desiliconisation	$[Si] + 2[O] + 2\,[CaO] \leftrightarrows (2CaO \cdot SiO_2)$
▪ Manganese reaction	$[Mn] + [O] \leftrightarrows (MnO)$
▪ Dephosphorisation	$2[P] + 5[O] + 3\,[CaO] \leftrightarrows (3CaO \cdot P_2O_5)$
Deoxidation	
Removal of residual oxygen through ferro-silicon	$[Si] + 2\,[O] \leftrightarrows (SiO_2)$
Aluminium reaction	$2[Al] + 3\,[O] \leftrightarrows (Al_2O_3)$

Scrap and iron ore for cooling are added to the process as well. Due to turbulent conditions during operation, CO, CO_2, dust, and vaporized traces of metals like Fe, Cr, copper (Cu), lead (Pb) and Mn leave the BOF through the off-gas stream. As a result of the process, crude

steel and slag, consisting mainly of oxides, are formed inside the BOF and because of density differences, the lighter slag floats on the metal bath. [1,18] Generally, during crude steel manufacturing via the BOF due to exothermic reactions, more energy can be gained than consumed, demonstrating an exception in steelmaking, with a potential for energy recovery of 0.234 GJ/t. [3] Summarized, the objectives of the oxidation process in a BOF are the reduction of the carbon content (from approximately 4 – 5% to 0.01 – 0.4%), the adjustment of desired elements and oxidation of impurities. According to Table 1, the reaction mechanism of dephosphorisation is shown, which will be discussed in more detail in chapter 2.3.2. P, Si, Mn, aluminium (Al), and other elements enter the slag in their oxidic states. [1,19] The characteristics and the formation of BOFS are covered in the next chapter.

2.3 Basic oxygen furnace slag

In the EU (28), the BF/BOF route accounts for 57.6% of crude steel production (139.2 Mt). Considering the situation in Austria, it is even 90% (~6.1 Mt). [2] For 1000 kg crude steel in a BOF, around 100 – 150 kg of slag occur, which means substantial amounts of BOFS accumulate continuously. [6] Based on the mentioned values, a mass stream of BOFS between 8 – 12 Mt for the EU (28) and approximately 0.6 – 0.9 Mt in the case of Austria can be expected every year.

2.3.1 BOFS: Characteristics, formation, and function

As described in chapter 2.2 BOFS composed predominantly of oxidic components and is accompanied by oxides from valuable metals such as Fe, Cr, and Mn. Due to deviations in quality and constituents of charged materials during the production route, characteristics and composition of BOFS can be widely fluctuating. [20] Table 2 summarizes the composition of five different BOFS-samples from voestalpine. [12] The ranges of the shown values are in a reasonable agreement with different BOFS-analyses from other steelworks presented in respective literature. [5,14,19,21]

Table 2: Composition of BOFS samples from analysis of voestalpine, cf. [12]

Fe [m.-%]	CaO [m.-%]	SiO_2 [m.-%]	MnO [m.-%]	P_2O_5 [m.-%]	MgO [m.-%]	V [m.-%]	TiO_2 [m.-%]	Cr [m.-%]	CaO/SiO_2 [-]
18.70	35.00	11.20	4.50	0.80	5.60	0.01	0.30	0.21	2.90
-	-	-	-	-	-	-	-	-	-
29.00	40.00	12.70	6.80	1.50	7.90	0.06	0.40	0.41	3.40

In addition, slag components such as Al_2O_3 (2.17 m.-%) or MnS (0.11 m.-%) are mentioned. [14] Fe in Table 2 is expressed as the total amount of iron in the slag and can occur as metallic Fe, FeO or Fe_2O_3. The same is true for Cr, mainly present as Cr_2O_3 or CrO, respectively. [14,18,22,23] However, significant components in BOFS are CaO, FeO and SiO_2, which can be supported by Table 2. A high CaO/SiO_2 ratio is preferred and can be ensured by adding lime (CaO, $CaCO_3$) or dolomite ($MgCa(CO_3)_2$). [18]

Two theories can describe slags: The ion and the molecular theory, whereby the latter has been replaced by the former. The principle of the ion theory states that a liquid slag is composed of positively or negatively charged ions, which are in constant interaction with each other, whereby the relation between ion radius and charge is essential. According to their behaviour in the liquid slag, compounds can donate or accept oxygen ions (O^{2-}), which results in their distinction between basic or acidic components. As a result, CaO, a basic oxide, is capable of donating O^{2-}, whereas P_2O_5 and SiO_2 (acidic oxides) in turn accept O^{2-}. [24] A compound such as Al_2O_3 can act simultaneously as an oxygen-donator and an oxygen-acceptor and is referred to as an amphoteric oxide. Basic, acidic, and amphoteric examples are shown in Equation 2-1 – 2-5. Fundamentally, slags are build-up of plain anionic complexes like $[SiO_4]^{4-}$, $[PO_4]^{3-}$, $[AlO_3]^{3-}$, and $[FeO_2]^{-}$ (network formers), anions including O^{2-}, S^{2-}, and F^{-}, cations like Ca^{2+}, Fe^{2+}, Fe^{3+}, magnesium cation (Mg^{2+}), and Mn^{2+} (network modifiers) and intermediate (amphoteric) cations like Al^{3+}, Pb^{2+}, and zinc cation (Zn^{2+}). [25] The notation indicates that species in parenthesis are bound in the slag phase, square brackets denote the metal phase, and curly brackets signalize compounds in the gas phase.

$$(CaO) \leftrightarrows (Ca^{2+}) + (O^{2-}) \quad \textbf{2-1}$$

$$(P_2O_5) + 3(O^{2-}) \leftrightarrows 2(PO_4^{3-}) \quad \textbf{2-2}$$

$$(SiO_2) + 2(O^{2-}) \leftrightarrows (SiO_2^{4-}) \quad \textbf{2-3}$$

$$(Al_2O_3) \leftrightarrows 2(Al^{3+}) + 3(O^{2-}) \quad \textbf{2-4}$$

$$(Al_2O_3) + 3(O^{2-}) \leftrightarrows 2(AlO_3^{3-}) \quad \textbf{2-5}$$

The ratio between basic and oxidic components within the slag is known as the basicity. According to Equation 2-6 – 2-8**,** several formulae for their determination exist by considering the influence of different compounds. [25] If not otherwise stated, the term B_2 is used to describe the basicity in the further course of this thesis.

$$B_2 = \frac{m.-\%\ (CaO)}{m.-\%\ (SiO_2)} \quad \textbf{2-6}$$

$$B_3 = \frac{m.-\%\ (CaO) + m.-\%\ (MgO)}{m.-\%\ (SiO_2)} \quad \textbf{2-7}$$

$$B_4 = \frac{m.-\%\ (CaO) + m.-\%\ (MgO)}{m.-\%\ (SiO_2) + m.-\%\ (Al_2O_3)} \quad \textbf{2-8}$$

Conclusive, slags generally consist of metal compounds with oxygen, sulphur, phosphorus, and fluorine (F). Additionally, slags accomplish very important tasks in steelmaking: [25]

- Removal of detrimental accompanying elements like phosphorus and sulphur from the metal; integrating and transferring it into the slag.
- Protecting the metal from uncontrolled oxidation after tapping.
- Protects the metal from undesired intake of detrimental elements (sulphur, hydrogen (H_2), and nitrogen).
- Minimizing heat losses because of thermal insulation of the liquid metal bath.
- Good separability owing to differences in density, and viscosity. [25]

2.3.2 Dephosphorisation process in a BOF

Phosphorus enters the steelmaking process as a constituent of coke- and coal-ash, gangue content and aggregates, in the form of P_2O_5, $3CaO{\cdot}P_2O_5$ (C_3P), and $3FeO{\cdot}P_2O_5$ (Fe_3P) and is bound into the crude iron, which is then post-processed in the BOF. [25] Although phosphorus is found only in minor amounts (0.1 – 2 m.-%) in the pig iron, its adverse impact on steel properties causes brittleness and ultimately leads to the reduction of toughness and ductility. [26,27] The steady decrease of iron ore and scrap quality intensifies the P-accumulation, posing greater challenges to the BOF process. [8] For this reason, the mechanism behind dephosphorisation is very well-investigated and can be expressed by the De-Phosorisation coefficient L_P, which is an indicator for the distribution of P between slag and metal. Different definitions are stated in respective literature (Equation 2-9 and 2-10), while higher values for both, $L_{P(0)}$, and $L_{P(1)}$ imply that more P is bound into the slag. Thus, it can be achieved by lower temperatures, FeO contents between 15 – 20 m.-%, higher basicity (up to 4.0), and lower magnesium and carbon contents. [9] Moreover, higher Al_2O_3 and Mn contents reduce the De-Phosorisation coefficient, while an optimum range between 25 – 30 m.-% of FeO at higher basicity values (3.9 – 4.2) can be observed. [28,29] However, it can be

concluded that slag composition and temperature significantly impact the phosphorus partition. [28]. In addition, it must be considered that high oxygen concentrations lead to a lower carbon amount and increase the FeO content in the slag. Owing to the high melting point of CaO (>2800 °C), FeO is applied to keep the slag in a liquid state. [9] $L_{P(1)}$ is used in this thesis if not otherwise stated.

$$L_{P(0)} = \frac{(\%P_2O_5)}{[\%P]} \quad \textbf{2-9}$$

$$L_{P(1)} = \frac{(\%P)}{[\%P]} \quad \textbf{2-10}$$

In general, it can be presumed that P is preferably found as solved phosphate ions (PO_4^{3-}) in the hot liquid slag, while the contribution of phosphide ions (P^{3-}) can be omitted. [30,31] The path phosphorus is making from the metal into the slag can be described using the molecular theory (Equation 2-11 and 2-12). First, FeO is reduced, forming metallic iron while phosphorus in the metal is oxidized and integrated as Fe_3P. With the help of CaO, phosphorus is finally bound into the slag as $3CaO \cdot P_2O_5$. On the other hand, also the ion theory can be used to describe the same process (Equation 2-13). Afterwards C_3P emerged by the attendance of solved Ca^{2+}-ions. [10,25,29] However, it should be noted that in both slag theories, phosphorus is mainly incorporated into the BOFS in the form of C_3P. [14]

$$2[P] + 8(FeO) \leftrightarrows (3FeO \cdot P_2O_5) + 5[Fe] \quad \textbf{2-11}$$

$$(3\,FeO \cdot P_2O_5) + 3(CaO) \leftrightarrows (3\,CaO \cdot P_2O_5) + 3[FeO] \quad \textbf{2-12}$$

$$[P] + 2.5[FeO] + 1.5[O^{2-}] \leftrightarrows (PO_4^{3-}) + 2.5[Fe] \quad \textbf{2-13}$$

Concerning Equation 2-14, Equation 2-15 ($a_{[Fe]} = 1$) shows the appropriate equilibrium constant. In general, removing phosphorus involves exothermic reaction processes ($-\Delta H$). High dephosphorisation-rates can be obtained at a ratio between $CaO/P_2O_5 > 3$ owing to a high P-distribution. For effective dephosphorisation, an early formation of a CaO-slag is vital. In sum, crucial parameters for a satisfying dephosphorisation are: [25]

- Oxidizing conditions (higher FeO-activity).
- High CaO-activity.
- Lower temperature (promotes exothermic reactions). [25]

$$2n[P] + 5n(FeO) + n(CaO) \leftrightarrows n(\ CaO \cdot P_2O_5) + 5n[Fe] \quad \textbf{2-14}$$

$$K_{[P]} = \frac{a_{(nCaO \cdot P_2O_5)}}{a_{[P]}^2 a_{(FeO)}^5 a_{CaO}^n} \quad \textbf{2-15}$$

Phosphorus in the pig iron is incorporated in a metal and is transferred with the aid of refining within the BOF into the slag in their oxidic state as phosphates. Therefore, the processing of BOFS discriminates from the refinement process in the converter owing to the different presence of phosphorus-species, which will be discussed in chapter 2.5.

2.3.3 Slag utilisation

Steel slag can be divided into slag from the BOF, EAF, and ladle metallurgy. In 2016, the EU generated around 20 Mt of steel slag, whereby 56.6 m.-% of the total slag production can be allocated to BOFS. [32–34] This massive accumulation of residues in the form of steel slag illustrates the necessity of a meaningful utilisation. The continuous increase in the development of global steel production requires environmental regulations, which results in the limitation of industrial waste landfilling, promoting the recycling and reuse of by-products such as slag, dust, sludge, and gases. [32] Results from various literature manifest that processing BOFS aiming in construction applications, especially as binder material in the cement industry by the simultaneous recovery of valuable metals. Slag in steelmaking generally can be used in various utilisation possibilities with strong differences across national boundaries. This includes for example an internal steelworks recycling, construction material, cement clinker substitute, and agricultural fertilizer, although the use of the latter has declined sharply in the EU during past decades. [35] Owing to the abundance of primary resources and differences in legislation, the recycling rate of slag can be subject to strong international fluctuations. Issues with volume stability and the worry about toxic elements were also mentioned. [36,37] Slag commonly accumulates at different temperatures, dependent on the production route, which accounts to 1723 K for blast furnace slag (BFS), 1573 K for BOFS, and 1823 K for slags from an EAF. These different temperature ranges combined with varying compositions results in a slag enthalpy of 1.6 GJ/t for BFS, 1.3 GJ/t for BOFS, and 1.8 GJ/t for EAF slag. However, low thermal conductivity of 1 – 3 W/K·m concerning solid slag and even tenfold lower values of 0.1 – 0.3 W/K·m for liquid slag at temperatures between 1673 K – 1773 K poses great challenges in utilising their high waste heat recovery potential. [38–40]

Commonly, ironmaking slag products can be classified dependent on their cooling conditions into air cooled, granulated, and pelletised products. The formers deployment

possibilities range from a construction additive, concrete products, asphalt concrete, road construction over to clinker raw material, roof covering, until mineral wool among others, while granulated slag, glassy solidified is widely used in the cement industry. Slower strength formation is reported for concretes containing granulated slag compared to concrete mixed with Portland cement, the widely distributed sort of cement. If processed properly, pelletised, or expanded slag, similarly to volcanics indicates cement-like properties. Slag from the BOF, or EAF in turn is cooled comparable to that of air-cooled ironmaking slag, which results in the same scope of application, while characteristics can be distinguished to slag from the BF, facing a lot more restrictions due to the content of more problematic species. In total, approximately 50% of steelmaking slag is used externally, particularly in road construction. High amounts of CaO and MgO in steelmaking slag, unfavourable for construction utilisation, is one of the main obstacles. For this reason a pre-treatment by adding SiO_2 or oxygen to the liquid slag is necessary in order for free-lime binding to prevent a volume expansion, and finally guaranteeing the concretes stability. [6,41]

The major phase observed in an unprocessed BOFS is larnite (β-C_2S) followed by wustite mixed crystals (Fe_{1-x-y}, Mg_x, $Mn_y)O_z$. [36,42] The slag must meet certain quality criteria for concrete or cement addition. Hence, resemblances regarding chemical composition as well as mineralogical characteristics are highlighted. In the case of BOFS, it is indicated that the main distinction to Portland cement is the missing C_3S-phase and high wustite contents. [43] Moreover, hydraulic minerals are crucial, which can be improved by a higher glass content due to increasing amorphous structures. Thus, it can be achieved by treating BOFS at higher cooling rates resulting in the encapsulation of metals and oxides by a simultaneous solubility reduction of heavy metals. [44] Leaching behaviour also plays a vital role in BOFS utilisation because of the occurrence of Cr, and vanadium (V). In terms of Cr, it is stated that Cr^{6+}, which is mainly of anthropogenic origin, is by far more toxic than the natural occurring Cr^{3+}. Thus it can be concluded that pollution of solely Cr^{6+} is expected after the BOFS leaching. [45,46] Despite high Cr-concentrations in BOFS, several experiments in respective literature show a low leaching behaviour. [36,37,42,47] However, structural suitability and environmental compatibility of the accumulating slag must be considered, with legal limit values being steadily tightened by legislation. [42] In summary, the utilisation of BOFS as a construction material requires certain quality criteria concerning material properties. For this reason, it can be satisfied by modifying the slag using different processing methods. Looking at the values of Fe, and MnO, depicted in Table 2, the noticeably high amounts would also be incorporated into the product slag, remaining unused. For this reason, the treatment's purpose should result in a separation of the initial BOFS into a useable product slag with defined properties and a metal phase consisting preferably of Fe, Mn, and Cr. Additionally, high slag temperatures

reveal an enormous waste heat recovery potential. In compliance with legal regulations, both material- and energy efficiency improvements can save resources and would lead to the reduction of CO_2 emissions.

2.4 Relevant thermodynamic fundamentals

As outlined in chapter 2.3.1, the ion theory can be used to define the behaviour of liquid slags, describing positive and negative charged ions, which are in constant interaction with each other. The ability of each ion (dissociated species) to react with other substances in the liquid slag is referred to as the activity a, which is affected by pressure, temperature, and slag composition. Their calculation can be seen in Equation 2-16 with γ_i, and x_i describing the activity coefficient and concentration of the respective component i. The activity coefficient can generally be greater or lower than 1, representing an ideal state's deviation indicator and is 1 in the ideal state. [25]

$$a_i = \gamma_i \cdot x_i \qquad \textbf{2-16}$$

Quantitative characterisation of chemical equilibrium can be done by the free energy or free enthalpy. The latter, the free enthalpy, is favoured since most processes occur under constant pressure. According to Equation 2-17, the equilibrium of a chemical reaction is reached when the reaction rate between product formation (C and D) and reactant formation (A and B) is equal. By referring to Equation 2-17, the ratio between products and reactants is called the equilibrium constant (K), which is shown in Equation 2-18, with the stochiometric coefficients (a, b, c, and d) appearing as exponents. Under equilibrium conditions, Equation 2-19 is fulfilled. [25]

$$a \cdot A + b \cdot B \leftrightarrows c \cdot C + d \cdot D \qquad \textbf{2-17}$$

$$K = \frac{a_C^c \cdot a_D^d}{a_A^a \cdot a_B^b} \qquad \textbf{2-18}$$

$$\Delta G = 0 \qquad \textbf{2-19}$$

Equation 2-20 can be derived and Equation 2-21 is valid as well, the free Gibb's energy can also be defined by the enthalpy change ΔH^0, entropy change ΔS^0, and temperature T. [25] In the case of processes taking place under constant pressure and temperature, the Gibb's energy aims for a minimum. [48].

$$\Delta G^0 = -R \cdot T \cdot \ln\left(\frac{a_C^c \cdot a_D^d}{a_A^a \cdot a_B^b}\right) = -R \cdot T \cdot \ln(K) \quad \textbf{2-20}$$

$$\Delta G^0 = \Delta H^0 - T \cdot \Delta S^0 \quad \textbf{2-21}$$

This thesis's reactions of great interest are reduction and oxidation reactions; see a general oxidation reaction in Equation 2-22. By means of such processes, the notion of the chemical potential can be used. Under the condition that all activities in Equation 2-23 correspond to that of pure substances ($a_{Me}, a_{Me_xO_2} = 1$) and the standard pressure p^0 is 1 atm, Equation 2-24 follows. [25] A "0" in the exponent indicates standard conditions.

$$x \cdot Me_{solid,liquid} + O_2 \leftrightarrows Me_xO_{2solid,liquid} \quad \textbf{2-22}$$

$$K = \frac{a_{Me_xO_2}}{a_{Me}^x \cdot \frac{p_{O_2}}{p^0}} \quad \textbf{2-23}$$

$$K = \frac{1}{p_{O_2}} \quad \textbf{2-24}$$

Regarding Equation 2-20 and substituting it with the expression of K in Equation 2-24, Equation 2-25 can be expressed, whereas p_{O_2}must be used in bar. The term $R \cdot T \cdot \ln(p_{O_2})$ is better known as the oxygen potential. The more negative the free enthalpy, the more stable are the formed reaction products, and as a result by considering Equation 2-22, the oxide is more stable with a more negative logarithm or a lower value of the oxygen potential, respectively. [25]

$$\Delta G^0 = -R \cdot T \cdot \ln\left(\frac{1}{p_{O_2}}\right) = R \cdot T \cdot \ln(p_{O_2}) \quad \textbf{2-25}$$

2.4.1 Richardson Ellingham diagram

In the Richardson Ellingham diagram shown in Figure 5, the free Gibb's energy (ΔG) [kJ/mol] is plotted against the temperature [°C] and represents the oxygen potential of oxidation reactions as a function of the temperature. When looking at Equation 2-21, the lines in the diagram can be determined, whereby phase changes occur and must be considered. Consequently, the straight lines are characterized by the y-intercept (ΔH^0) and the slope (ΔS^0), whereby all reactions relate to the oxidation of one mole of oxygen at an oxygen partial

pressure of 1 atm. [25,49] Regarding a Richardson Ellingham diagram, the following statements can be derived:

- Metals with a lower oxygen potential reduce oxides with a more positive oxygen potential value (e.g., Mg reduces FeO).
- Nearly all metal oxidation reactions show approximately the same slope because of the negative entropy change.
- Due to increased entropy during a phase change, the straight-line slope is not uniform over the entire temperature range.
- In addition, two scales, one for the oxygen partial pressure p_{O_2}, and a second for the CO/CO_2 ratio are given to read the needed values for reduction. [25]

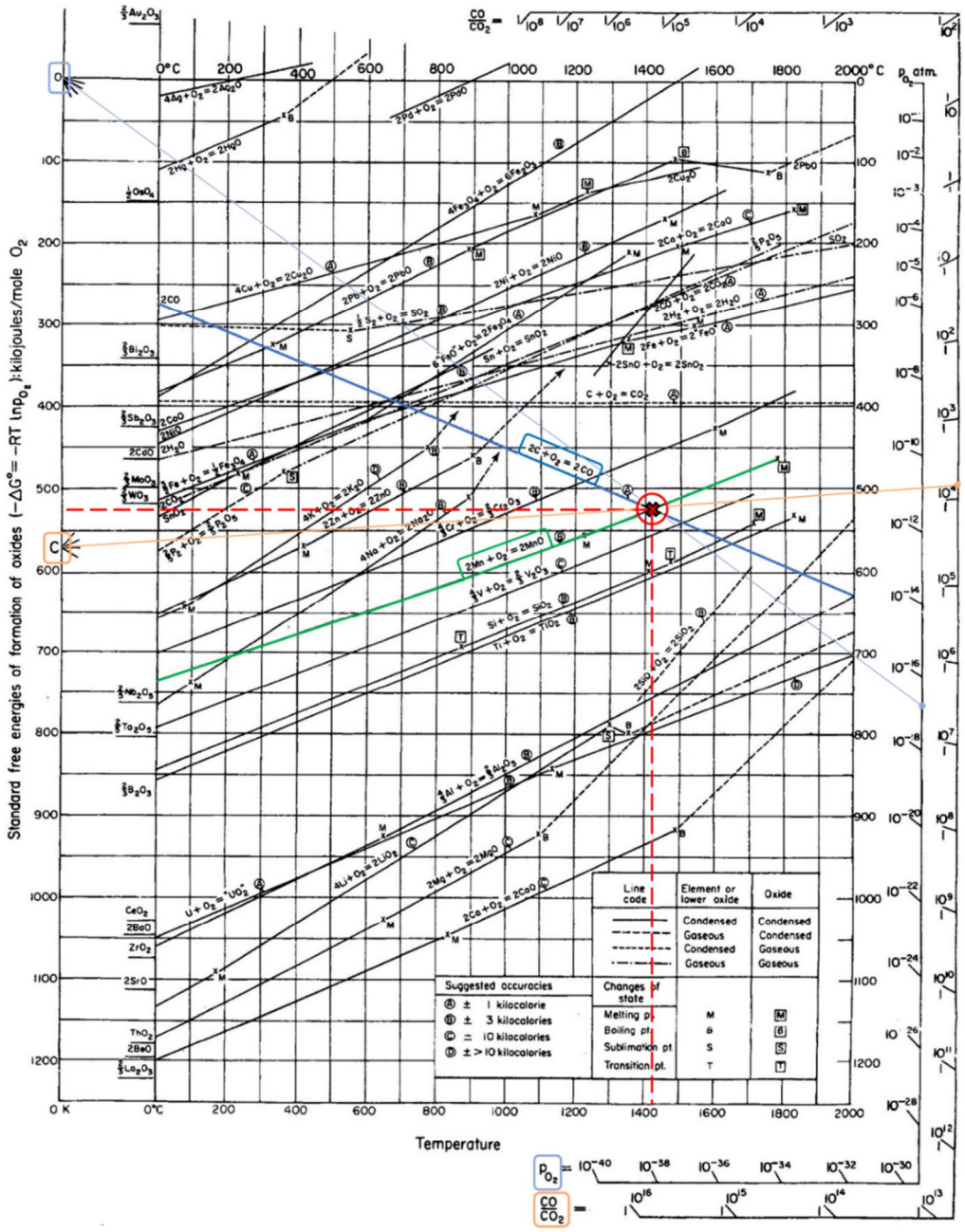

Figure 5: Richardson Ellingham diagram, cf. [49]

Three exemplary lines of oxidation reactions, given in Equation 2-26 – 2-28, show different temperature dependencies. Almost all straight lines in the diagram have a positive slope, which also applies to the oxidation of Fe. In other words, one mole of gas is consumed to form an oxide resulting in a negative entropy change. However, entirely different behaviour can be observed for the oxidation of carbon. Regarding Equation 2-27, one mole of gas on both the left and right-hand side of the reaction leads to an almost horizontal line. If, instead of CO_2, CO is formed, more mole gases are produced, and the slope of the line is falling owing to increasing entropy (see Equation 2-28). [49]

$$2Fe + O_2 \leftrightarrows 2FeO \quad \textbf{2-26}$$

$$C + O_2 \leftrightarrows CO_2 \quad \textbf{2-27}$$

$$2C + O_2 \leftrightarrows 2CO \quad \textbf{2-28}$$

Relevant direct reduction reactions for the further course of this thesis are expressed in Equations 2-29 – 2-32. [23,50]

$$(FeO) + [C] \leftrightarrows [Fe] + \{CO\} \quad \textbf{2-29}$$

$$(MnO) + [C] \leftrightarrows [Mn] + \{CO\} \quad \textbf{2-30}$$

$$(CrO) + [C] \leftrightarrows [Cr] + \{CO\} \quad \textbf{2-31}$$

$$(Cr_2O_3) + [3C] \leftrightarrows [2Cr] + \{3CO\} \quad \textbf{2-32}$$

For example, direct reduction of MnO through carbon as a reduction agent is introduced, representing the deduction of fundamental parameters from the Richardson Ellingham diagram according to Figure 5. At the point of intersection between the oxidation of carbon (dark blue line) and the oxidation of Mn (green line), the minimum reduction temperature (~1693 K), as well as the Gibb's energy (~525 kJ/mol), can be derived from the red dashed lines. Additionally, the oxygen partial pressure that occurs during equilibrium and the minimum ratio of CO/CO_2 can be determined. For this purpose, the point indicating "0" (orange line) or "C" (light blue) must be interconnected with the intersection (red cross). Afterwards, the line needs to be extended until it cuts the appropriate scale on the right-hand side of the diagram. [49]

The reduction degree (RD) is generally a useful parameter for describing reduction reactions, defining the percentage of removed oxygen from the original oxide (see Equation 2-33). O and Fe_{tot} possesses the unit mole into the equation, whereas Fe_{tot} is the total amount of iron. [25]

$$RD = \left(1 - \frac{O}{1{,}5 \cdot Fe_{tot}}\right) \cdot 100 \quad \textbf{2-33}$$

This can be illustrated using the example of iron oxides according to Table 3. [25]

Table 3: RD for iron oxides, cf. [25]

Species	RD [%]
Fe_2O_3	0.0
Fe_3O_4	11.1
FeO	33.3
Fe	100.0

The metallisation grade (MG) can be determined by Equation 2-34. Fe_{met} represents the metallic iron content in the sample. [25]

$$MG = \frac{Fe_{met}}{Fe_{tot}} \cdot 100 \qquad \textbf{2-34}$$

There is a common cohesion between RD and MG, which can be seen in Figure 6. The determination of the MG sometimes yields different results because different iron species can be found in the composite (Fe, Fe^{2+}, and Fe^{3+}). As an example, a material with 33% RD may be consist of pure wustite (FeO) but can also be a mixture of hematite (Fe_2O_3 – RD = 0%), wustite (FeO – RD = 33.3%) and metallic iron (Fe – RD = 100%). In both cases, the MG differs, while MG = 0% for pure wustite, MG > 0% for a mixture. [25]

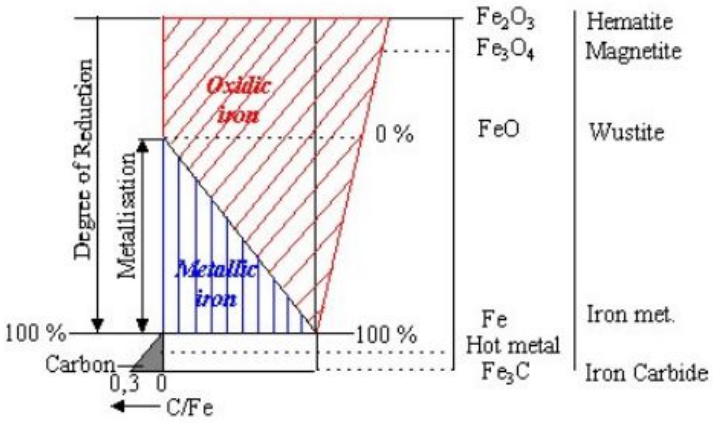

Figure 6: Coherence between RD, MG, and carburisation to cementite [25]

2.4.2 Ternary phase diagram

Phase-, or state diagrams can be used as a helpful tool for the evaluation of phases at the basis of a defined slag composition. In addition, the melting point can also be estimated. Both, binary and ternary systems, can be used for this purpose. As aforementioned in chapter 2.3.1 main components of BOFS are FeO, CaO, and SiO_2. Hence, a CaO-FeO_x-SiO_2 ternary system

is shown in Figure 7 and it is stated that they are subject to noticeable fluctuation in their composition for many reasons. [25]

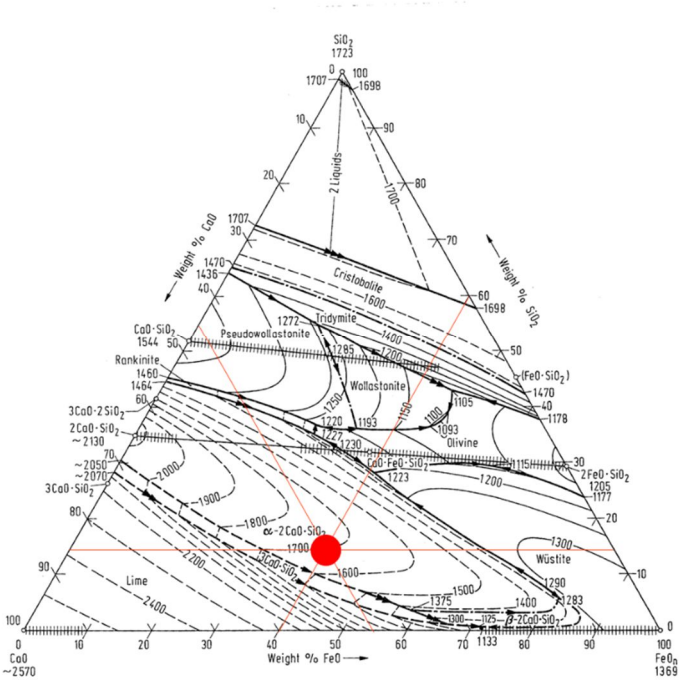

Figure 7: Ternary oxide system (CaO-FeO_n-SiO_2), cf. [51]

The coloured marking in the ternary system is intended to give an overview of the possible area of a representative BOFS composition. A basicity of 3.0, and a CaO-content of 45% are assumed. Throughout this thesis, denotations (abbreviations) for components in slag compounds are used, which should represent the following meaning: C (CaO), S (SiO_2), F (FeO) and P (P_2O_5) – summarized in Table 4.

Table 4: Relevant slag compounds and denotation, cf. [25]

Species	Compound	Denotation
Silicates	$CaSiO_3$ | Ca_2SiO_4 | Ca_3SiO_5	CS | C_2S | C_3S
	$FeSiO_3$ | Fe_2SiO_4	FS | F_2S
Phosphates	$Ca_3(PO_4)_2$ | $Ca_4P_2O_9$ | $Fe_3(PO_4)_2$	C_3P | C_4P | F_3P

2.5 Treatment of BOFS

The treatment of BOFS can be classified into mechanical-, hydrometallurgical- and pyrometallurgical processing methods. [14] While the first two are not further discussed in this thesis, this work aims at the pyrometallurgical treatment of BOFS, including all

high-temperature processes for metal extraction carried out under the exclusion of oxygen. As mentioned, a goal of treating slags is the generation of an active hydraulic material used as binder in the field of construction. However, a crucial approach using the principle of reduction is to split up the initially modified slag into a product slag and a metal phase by the simultaneous separation of P. Consequently, this offers accessing metals that are currently unused. In the following chapter, the state-of-the-art treatment of BOFS, the principle of carbo-thermal reduction, is explained in more detail. Afterwards, the InduRed process and a smaller experimental plant, the so-called InduMelt, are introduced.

2.5.1 Carbo-thermal treatment of BOFS

According to the literature, BOFS consists of two major phases: On the one hand, a P-containing $2CaO{\cdot}SiO_2$-$3CaO{\cdot}P_2O_5$ (C_2S-C_3P) solid solution and on the other hand a CaO-SiO_2-FeO phase. [52,53] By the carbo-thermal reduction of BOFS, the separation into slag and a metal alloy is feasible. However, the accumulation of P within the metal limits their re-use. P supports the stabilization of the β-C_2S phase, and a complete removal of P would inevitably lead to a degradation of the slag owing to the phase change of β-C_2S into γ-C_2S, arising from an increasing volume during slow cooling-rates. However, cooling happens commonly quicker, which has the most significant impact on phase transformation processes. Furthermore, this phenomena was only observed at experiments in the subsequent discussed InduMelt plant, where cooling rates of treated material is very slow. [36] A high proportion of a C_3S phase in the slag is favoured to match hydraulic activity properties. Thus, it can be enabled by the split of P-O bonds in the C_2S-C_3P phase during the reduction of BOFS. Owing to the attendance of calcium ions, and silicate, the desired C_3S phase originates from the slag, and it can be assumed that the C_3S-formation is enhanced with the aid of reduction. P-reduction process using solid carbon or CO as a reducing agent and the corresponding C_3S-formation is shown in Equation 2-35 and 2-36. [54]

$$5C(5CO) + 3Ca_2SiO_4 + Ca_3(PO_4)_2 \leftrightarrows 3Ca_3SiO_5 + 5CO(5CO_2) + 2[P] \qquad \textbf{2-35}$$

$$5C(5CO) + 3Ca_2SiO_4 + Ca_3(PO_4)_2 \leftrightarrows 3Ca_3SiO_5 + 5CO(5CO_2) + P_2(g) \qquad \textbf{2-36}$$

Several carbo-thermal reduction experiments were conducted by increasing the quantity of added carbon to a modified BOFS. The carbon amount, which is crucial for the reduction behaviour in the slag, is preferably first consumed to reduce wustite (FeO) forming metallic iron. With an increasing carbon addition, a higher reduction degree of P-containing compounds is noticeable, and therefore P accumulates in the iron phase. [5] However, the reduction

reaction occurs in a specific sequence and P-inclusion with an increasing carbon amount into metallic iron can be observed. To maximize the rate of reduced iron by simultaneously minimising the unwanted P-enrichment in the metal, the molar amount of carbon is stated to be three times higher than that of iron oxides ($C/Fe_2O_3 = 3$). [54] By reducing synthetically produced slags in a graphite crucible at 1823 K, similar results would be obtained regarding the reduction behaviour between FeO and P_2O_5. 80% of both compounds were reduced after only 20 min, while FeO is reduced much faster than P_2O_5. The course of reduction for both species differs significantly, while for FeO it is fast at the beginning and becomes flatter at the end, it is continuously increasing compared to P_2O_5 reduction. Higher slag basicity values of around 1.4 and higher temperatures support the reduction. From a thermodynamic point of view, P_2 gas is produced during P_2O_5 reduction. [55] This thesis will show that P also has an affinity for other metallic slag components like Cr, and Mn. Meeting the requirements just mentioned, the following objectives should be achieved using carbo-thermal reduction for an optimal BOFS utilisation: [14]

- Extraction of a metal alloy consisting of Fe, Cr, and Mn.
- Avoidance of contact between gaseous P and potential reaction partners.
- Creation of a proper slag phase for the field of cement industry. [14]

Therefore, a reactor concept facing all these challenges, constructed at the Chair of TPT (MUL) will be discussed in the next chapter.

2.5.2 InduRed process

For an efficient circular reuse of residues in the steel industry, the recovery of valuable metals like Fe, Cr, and Mn in BOFS is of utmost importance. Their occurrence in the slag as oxides after the refining step in a BOF requires the removal of bound oxygen through reduction. If the reduction occurs, for instance, in an EAF, Fe, Cr, Mn, and P compounds are reduced and highly reactive gaseous and elementary P is formed, reacting subsequently with the metal bath, which leads to the formation of undesired phosphides. For this reason, the return of the emerging metal phase in the steel works is not beneficial, owing to an accumulation of P in the produced steel. [13]

To meet the requirements associated by high temperature reduction of phosphorus bearing materials, the RecoPhos process for the treatment of sewage sludge ash for P-recovery was constructed on the TPT at MUL. Continuous advancement leads finally to the introduction of the InduRed process, arising from an intermediate plant called Indu-Carb. The former, the InduRed process, introduced in this chapter is originally a pilot-scale plant for the

carbo-thermal reduction of sewage sludge ashes, but the main principle is also applicable to the utilisation of other different industrial and municipal residues such as BOFS. Furthermore, Li-ion battery recycling using the same reactor concept is just becoming the subject of research efforts, demonstrating the flexibility by processing different critical residues with a similar experimental setup. The InduRed reactor concept imposes a proper solution for the presented challenges of carbo-thermal high temperature reduction. However, its operation is time- and cost-intensive as well as a lot of staff is required, which leads to the construction of a smaller laboratory-scale plant called InduMelt, which is explained in the next sub-chapter 2.5.3. Since this work focuses on BOFS, only this material's treatment, and related challenges are discussed.

Core part of the InduRed plant is a packed bed reactor consisting of an inductively heated column filled with pieces of graphite, whereby the bulk was replaced by graphite cubes in the subsequent explained InduMelt plant. The outer shell of the reactor is made of ceramic, and an insulation layer shall keep heat losses low. An illustration of the InduRed reactor is shown in Figure 8. [14,56]

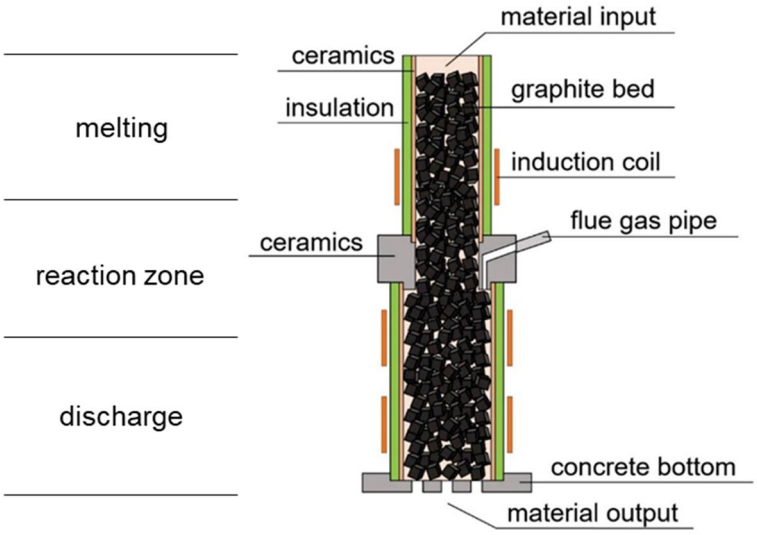

Figure 8: Structure of the InduRed reactor and classification into melting, reaction zone and discharge depending on the reactors height, cf. [14]

The simultaneous presence of P, and Fe in BOFS and their high affinity for each other leads to the undesired formation of phosphides and to the related problems already described above. Consequently, the desorption of P in the liquid metal must be promoted, which can be done by setting an under pressure at very high temperatures. [56] Three water-cooled induction coils, arranged at different heights around the reactor, ensure the heat input into the system,

adjusting the specific temperature along the reactors height profile. During operation, the induction coils create a high-frequency alternating field that induces eddy currents beneath the surface of the graphite pieces. As a result of the ohmic losses (Joule's law), the packed column is heated up to temperatures around 1900 K. The graphite pieces suitably meet the requirements as bed material in terms of their thermal properties. Furthermore, they provide the structure but do not act as a reductant and are not consumed during operation. For this reason, sufficient carbon powder is added to the BOFS. However, two crucial reactor properties play a vital role in the operation: An atmosphere that is poor in oxygen with a very high CO/CO_2 ratio and a large reaction surface provided by the graphite bed. [56,57]

The cold BOFS mostly modified with additives for basicity adjustment, and C-powder as reductant enter the process at the top of the reactor. The mixture melts instantly upon contact with the hot surface of graphite pieces happened and moves towards the bottom of the reactor as a molten film. In addition, liquefied metal is formed as spheric droplets on the graphite-cube's surface after reduction. During the reaction zone phosphorus-containing compounds and specific metals are reduced. Gaseous phosphorus is formed, whereas the thin layer of molten bath limits their transportation path and hence reduces the contact time with potential reaction partners (e.g., metals like iron). Furthermore, gaseous species like P_2 and CO as a product of direct reduction are removed at the reaction zone steadily during operation. Therefore, all parameters which favoured undesired phosphide formation mechanism can be restricted according to the special reactor design. At the bottom liquid metal and slag are discharged continuously from the process. Argon (Ar), which enters the reactor at the top and the bottom, acts as a purge gas to provide an inert atmosphere inside the packed bed. Moreover, it prevents the suction of false air and reinforces the contact between graphite pieces and reagents. The inert gas and the resulting product gas, mainly consisting of CO and P_2, leave the reactor in the middle part. A negative pressure of 0.3 mbar provides the continuous suction of gaseous compounds enabled by an induced draft fan. After leaving the reactor via an exhaust pipe, the gas stream is post-burned with air in a combustion chamber. Afterwards, the resulting flue gas, containing P_2O_5, is hydrolysed to phosphoric acid in a scrubber. The reactor dimensions are 1 m in height, and it has an inner diameter of approximately 0.20 m. An illustration of the main components of the InduRed pilot plant is shown in Figure 9. [14,56]

Figure 9: Main components of the InduRed pilot plant – (**1**) reactor, (**2**) post combustion chamber, and (**3**) gas scrubber [14]

The primary focus of the InduRed plant in the case of the treatment of sewage sludge ash is phosphoric acid production of a defined quality. [56] The main requirements for the treatment of BOFS again are accessing valuable metals resulting in an almost P-free metal alloy. Moreover, a P- and metal-free slag is preferred to be produced, while in terms of the criticality of P, phosphoric acid during operation can also potentially be produced; a relief from the dependency on European imports on phosphate rock could therefore be achievable. [14]

2.5.3 InduMelt plant

The setup of the InduMelt plant, which specifically is an induction furnace for batch operation at smaller scale is depicted in Figure 10**.** It consists of an oscillating circuit (single coil inductor and capacitors), a cooling circuit with water as coolant, a power supply unit, a Royer converter, and a microcontroller. [14]

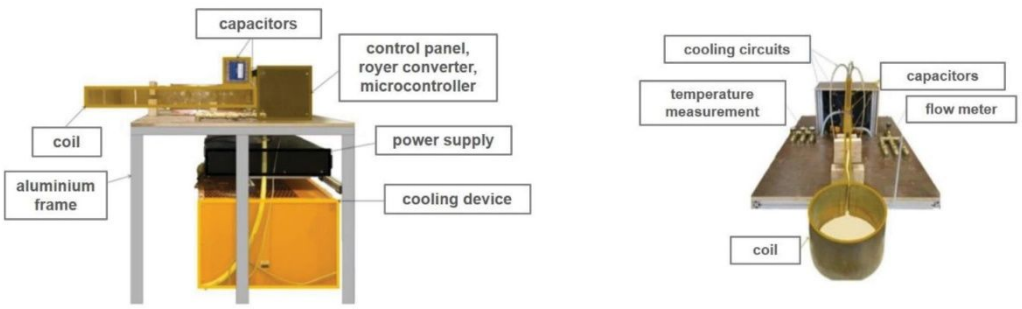

Figure 10: Component description of the InduMelt plant [14]

The coil of the InduMelt plant, which can be operated with a maximum power of 10 kW, is made of copper, and has a diameter of 0.20 m and a height of 0.12 m. It runs with a frequency of 50 kHz, and at this value, the maximum power loss is 3.1 kW. For safety reasons, the cooling inlet flow is split up into three sections so that the capacitors, the power electronics, and the induction coil have their cooling water supply. Volume flow-rate measurements at each cooling water circuit and the outlet temperature are measured. The schematic setup of the InduMelt plant, according to Figure 11, is shown below. [14]

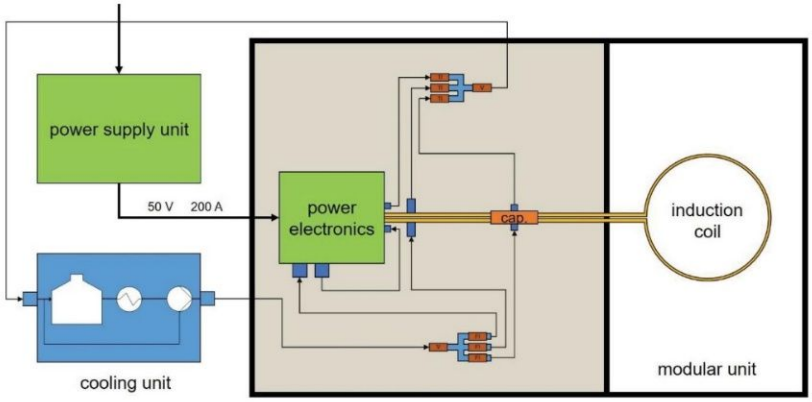

Figure 11: Schematic setup of the InduMelt plant [14]

In addition to reduction experiments, the InduMelt plant can also be used for smelting processes by changing the shape and position of the susceptor. For instance, the susceptor for the smelting experiments is a graphite ring arranged between a crucible construction and induction coil. In contrast, graphite cubes inside the crucible provide direct heat input for the reduction experiments. In the case of the smelting setup, contact between material and susceptor is undesired. The induction of eddy currents beneath the surface of the susceptor enables the heat input. Both designs can be seen in Figure 12. [14,58]

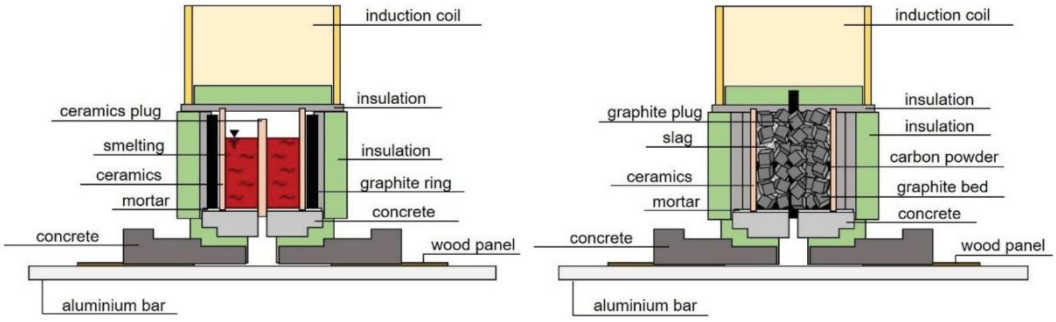

Figure 12: Setup for smelting and reduction experiments in the InduMelt plant [58]

2.6 Proposed process route for internal BOFS recycling [14]

According to respective literature, it is mentioned that the process of phosphide formation preferably takes place between Fe, and P during the carbo-thermal reduction of BOFS. Furthermore, it is stated that the amount of FeO in BOFS is a primary driver for the limitation of P gasification (see chapter 2.3). For this purpose, an altered proposed process route for the internal recycling of BOFS is given in this chapter and is depicted in Figure 13.

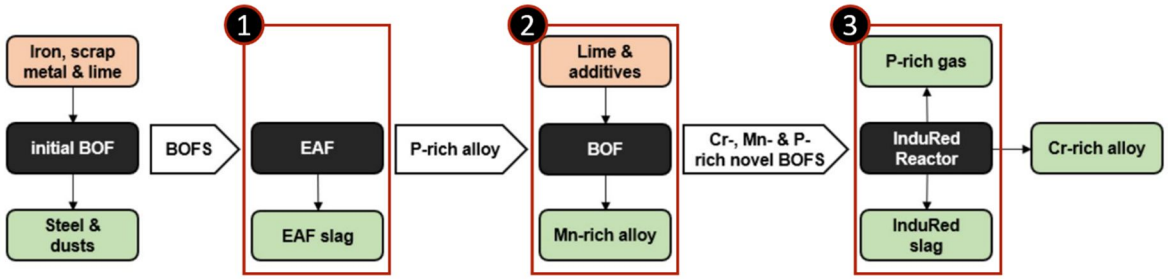

Figure 13: Proposed process route for the internal recycling of BOFS, cf. [59]

It can be derived from Figure 13 that in addition to the already known InduRed reactor, several sub-steps in different units need to be integrated. The new investigated process route includes the following steps: [14]

- (**1**) Processing of BOFS in an EAF.
- (**2**) Treatment of the emerging metal phase from the EAF in an additional BOF.
- (**3**) The slag phase from the BOF in step (**2**) is finally fed into the InduRed reactor. [14]

For a better understanding of the occurring phases, the three process operation units, as shown above, are introduced in more detail. First, the resulting slag from the refining step in the converter is reduced in an EAF and almost all P accumulates in the emerged metal phase. Afterwards, the resulting P-rich metal is fed simultaneously with additives such as lime, magnesia or FeO and slag forming components (B_2 adjustment) into a second BOF to transfer refining products into the slag matrix. A metal product, mainly composed of Fe, and Mn, is separated from a Cr-containing slag. Lastly, the generated slag from the second BOF enters the InduRed reactor, whereby the objective of treating the Cr-rich slag is to increase the phosphorus gasification degree (PGD) due to low FeO contents found in the input material. Moreover, a metal-alloy, which is rich in Fe, Mn, and Cr is generated from the InduRed reactor. [14]

As mentioned in chapter 2.5.2, the InduRed reactor is constructed as an inductively heated packed bed reactor filled with graphite pieces. Three fractions, a metal-, slag-, and a gas

phase, originates from the supplied feed slag. Summarizing the proposed internal recycling route, a Mn-alloy containing high amounts of iron is first separated. Then, the Cr-rich slag enters the InduRed reactor, resulting in the production of an alloy and gaseous P. It is assumed that by reducing the Fe-content in the slag, the PGD can be drastically increased, creating a usable, most widely P-free metal. The term novel BOFS, which will be used in the further course of this thesis, is the given name for the final slag product, which will be treated within the InduRed reactor in the proposed process route presented above.

2.6.1 Products composition from the altered process route [14]

First, it should be stated that the composition of products occurring during the suggested process route in Figure 13 had to be estimated. Relevant compositions of product streams, which will be described below, are depicted in Figure 14.

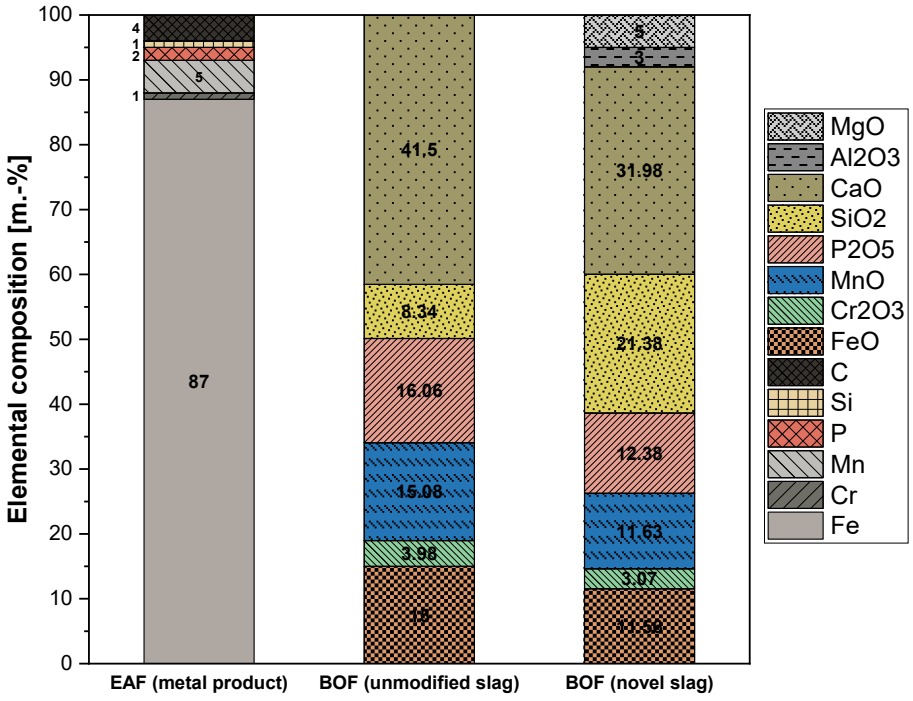

Figure 14: Assumed elemental composition of occurring product streams from the proposed process route, cf. [14]

In the case of the EAF, it is presumed by Ponak et al. (2019) that nearly the whole amount of P from the initial BOFS is transferred into the phosphorus rich alloy (metal product), which is composed of 87 m.-% Fe, 5 m.-% Mn, 1 m.-% Cr and further components like Si, C, and P. The metal from the EAF combined with calcium-silicate slag forming constituents is post-processed in a BOF, aiming for a re-oxidation of P and subsequent quick inclusion into a slag

product (unmodified slag). If 100 g of the modified mixture from the EAF are treated in a BOF, an aggregate slag amount of 25.66 g occurred. The required CaO amount can be evaluated by assuming that 90% of P and 100% of Si occurs as C_3P and C_2S, respectively. In addition, 20% of excess CaO were added and the assumed percental number of oxidised species in the slag from the BOF are 70% for Cr_2O_3, 60% for MnO, 90% for P_2O_5, and 100% for SiO_2. Moreover, FeO amount in the slag is 15 m.-%, considering that the ideal content is between 10 – 20 m.-%. The slag must then be modified by adding CaO, MgO, and Al_2O_3. Furthermore, SiO_2 for adjusting the basicity ($B_2 = 1.5$) is added, representing the final novel slag composition, which will be used as a reference for experiments results presented in chapter 2.6.2 below. [14] From Figure 14, it can be concluded that the novel BOFS is rich in P_2O_5 (12.38 m.-%) and contains considerably high amounts of MnO (11.63 m.-%) as well as FeO (11.56 m.-%). However, the content of Cr_2O_3 is still distinctly lower compared to the oxides of Fe, and Mn, while other typical slag forming components such as SiO_2, CaO, Al_2O_3, and MgO are also bound into the slag matrix.

2.6.2 Treatment of chromium- and phosphorus-rich slags [14]

According to Figure 14, the novel BOFS consists of substantial amounts of Fe-, Mn-, Cr-, and P-oxides. This chapter summarises the results of an experimental comparison by Ponak et al. (2019) between standard carbo-thermal reduction and reduction in the InduMelt plant using the concept described in 2.5.3. The objective of these experiments is to evaluate the behaviour of P regarding the difference in the expected novel BOFS composition compared to common BOFS. Therefore, a higher P-gasification rate is expected owing to lower FeO amounts. The novel BOFS, which is the same for both experiments, is obtained by producing a synthetic slag mixture. The experiments consist of a smelting and a subsequent reduction step, respectively. One of both experiments is carried out in an electrically heated furnace using a MgO-crucible as a melting unit. The results obtained are compared with the same experiment sequence conducted in the already described InduMelt plant. [14]

The desired amounts of chemicals representing the novel BOFS according to Figure 14 are blended. In a previous smelting step, the mixture is heated up to a temperature of 1873.15 K. Afterwards, the extracted and processed novel BOFS and sufficient C-powder are treated in a followed reduction step at the same temperature applied for the smelting. The results of the standard carbo-thermal reduction and the treatment in the InduMelt plant are summed up in Figure 15 and Figure 16. [14]

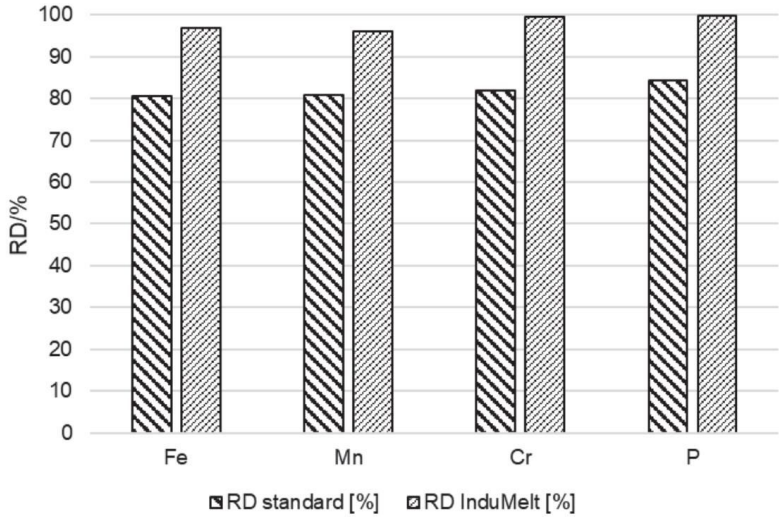

Figure 15: Comparison of the reduction degree achieved by standard carbo-thermal reduction and reduction in the InduMelt plant [14]

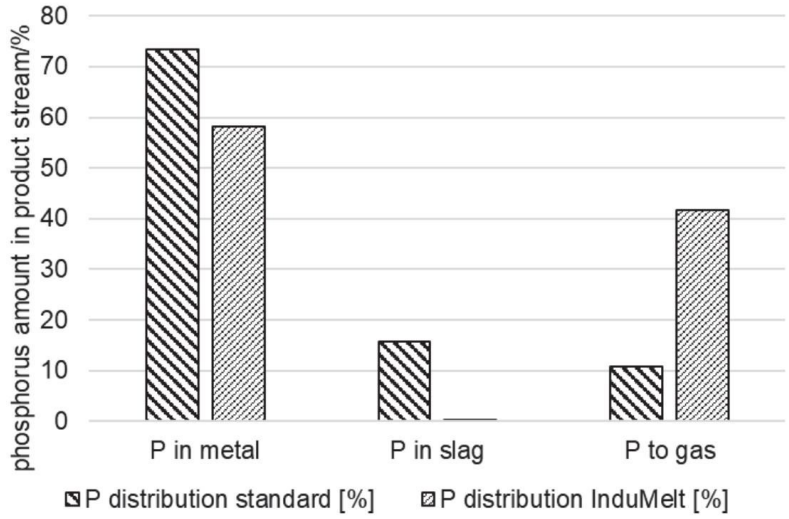

Figure 16: Comparison of phosphorus distribution achieved by standard carbo-thermal reduction and reduction in the InduMelt plant [14]

In general, it can be illustrated that the reduction degree of Fe, Mn, Cr, and P in the case of processed slag in the InduMelt plant are significantly higher than that of standard carbo-thermal reduction, which is depicted in Figure 15. Additionally, looking at Figure 16 and concerning the experiments conducted in the InduMelt plant, the distribution of P shows lower amounts in the metal, almost nothing in the slag and higher amounts in the gas. However, only 40% of the total P can be gasified, meaning that lower PGD-values compared to the treatment of conventional BOFS can be achieved. [14] Regarding these results, it is quite conceivable that the presence of Cr, and Mn in slags poses a challenge in addition to Fe. First, it was assumed that higher values of gasified P could be achieved by reducing the iron content in the

respective slag before processing it in the InduMelt plant. However, it could be shown that possibly Cr, and Mn also play a significant role during high temperature reduction.

2.7 Impact of metals during carbo-thermal reduction of phosphorus bearing slags

For increasing the yield of a utilisable metal-alloy by carbo-thermal treatment of BOFS at high temperatures based on the novel reactor concept, contact between gaseous P and liquid smelting should be reduced to a minimum. Consequently, a packed bed reactor filled with pieces or cubes of graphite including the introduced plants presented in chapter 2.5, provide a proper solution for the discussed challenge of phosphorus-containing material reduction. Whereas in previous experiments, it was first assumed that the undesired phosphide formation can be merely attributed to the existence of Fe, also Cr, and Mn are suspected of playing a major part in this process. [14] The behaviour between P and elements like Fe, Cr, and Mn need to be examined in greater detail, focusing on the mechanism behind phosphide formation.

2.7.1 Phosphide formation regarding Fe, Cr, and Mn

This chapter should give a better understanding of the reaction behaviour between P and certain metals during carbo-thermal treatment of slags by examining characteristic parameters. Therefore, it is required to identify those phosphides that are preferably originated based on thermodynamic and chemical aspects. This includes considerations concerning the free Gibb's energy at the maximum temperature inside the InduRed reactor (1900 K) and the activity of occurring slag species. Furthermore, the stochiometric ratio (SR), representing the relationship between corresponding metal and P in the predicted phosphide, needs to coincide with the presented slag composition in chapter 2.6.1.

First, the state and form of phosphorus should be determined in the investigated temperature range. Generally, different allotropic forms of phosphorus exist, which could commonly divide into three groups: White, black, and red (I, II, III, IV, and V) or violet phosphorus, where each of them has a great number of physical states and stabilities concerning thermodynamic considerations, which are until now not well understood. Since phosphides do not occur naturally and have only a small area of applications, little attention has been paid to them for a long time. Nevertheless, P reacts with many elements forming a wide variety of different solid

compounds. [60,61] Regarding ΔG, solid red phosphorus is most stable until 704 K. At this point, it vaporizes to a gas P_4(g), which exists in a range between 704 K – 1533 K. If the temperature exceeds, P_4(g) is converted into P_2(g), whereby the formation of monoatomic P-vapor P(g) requires very high temperatures beyond 2000 K. The stability of phosphorus is illustrated in Figure 17, while areas of negative Gibb's energy are generally denoted with -100 kJ/mol signalizing their occurrence. [61] For this reason, considering the sequence and temperature window for ongoing reduction reactions in addition to the maximum operating temperature of the InduRed reactor (1900 K), gaseous P as P_2(g) can be assumed.

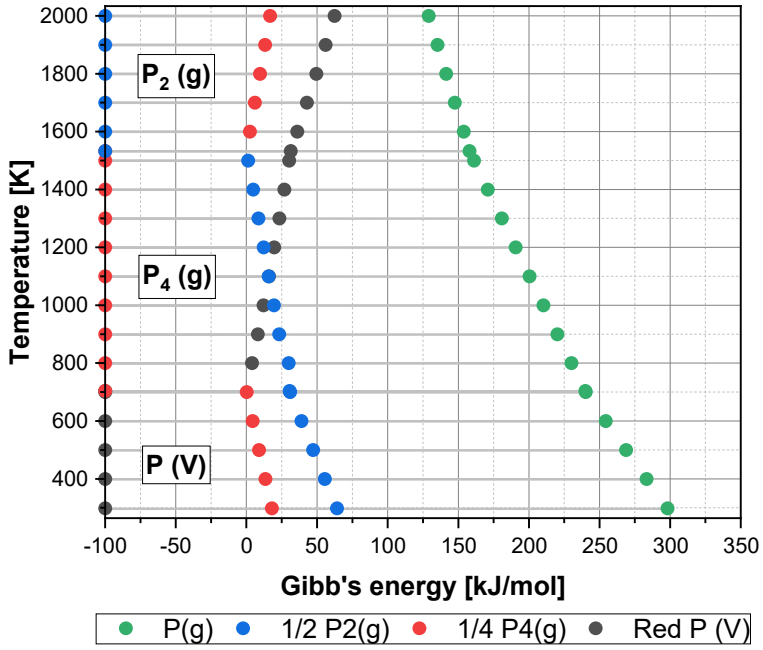

Figure 17: Gibb's energy [kJ/mol] of phosphorus species P(V), P_4(g), P_2(g), and P(g) in a temperature range between 298.15 K – 2000 K, cf. [61]

In general, phosphides during carbo-thermal treatment can be formed in two different ways (see Equation 2-37 - 2-39). [14] The appropriate equilibrium constant in Equation 2-40 and 2-41 indicates the strong impact of the metal (Me)- and P-activity or the partial pressure (p_{P_2}) of gaseous P on this process. Furthermore, it can be derived, that a stronger formation tendency of phosphides is related to higher activity coefficients ($\gamma_{P,Me} > 1$), whereas segregation is favoured at lower activities for the dissolved metal and P respectively ($\gamma_{P,Me} < 1$). [25] In fact, and supported by results from the literature, it can be stated that higher values of γ_P or γ_{Me} (higher activities) promotes the formation of phosphides.

$$\{P_2\} \leftrightarrows 2[P] \qquad \textbf{2-37}$$

$$x[Me] + y[P] \leftrightarrows [Me_xP_y] \quad \textbf{2-38}$$

$$x[Me] + y\{P_2\} \leftrightarrows [Me_xP_{2y}] \quad \textbf{2-39}$$

$$K_{Me_xP_y} = \frac{a_{Me_xP_y}}{a_{Me}{}^x \cdot a_P{}^y} \quad \textbf{2-40}$$

$$K_{Me_xP_{2y}} = \frac{a_{Me_xP_{2y}}}{a_{Me}{}^x \cdot p_{P_2}^y} \quad \textbf{2-41}$$

The strong interaction between P and Fe at high temperatures is well known. [62–64] This is also proven by experimental data showing a decreasing activity coefficient at higher Fe contents in Fe- and P-containing liquid solutions. [65–67] Activities of all compounds in a liquid molten bath of P-Fe-Mn increased with higher temperatures, whereby the greatest slope can be identified in the case of P. However, data of activities from different sources are inconsistent regarding the range of values. Owing to the minute content of P in slags, the Henrian activity coefficient γ_P^0 of P is applied to a Fe-Mn solution in a temperature range between 1400 – 1700 °C. Calculations show a lower $\ln(\gamma_P^0)$ in Mn compared to Fe with a higher deviation at lower temperatures, depicted in Figure 18. [66]

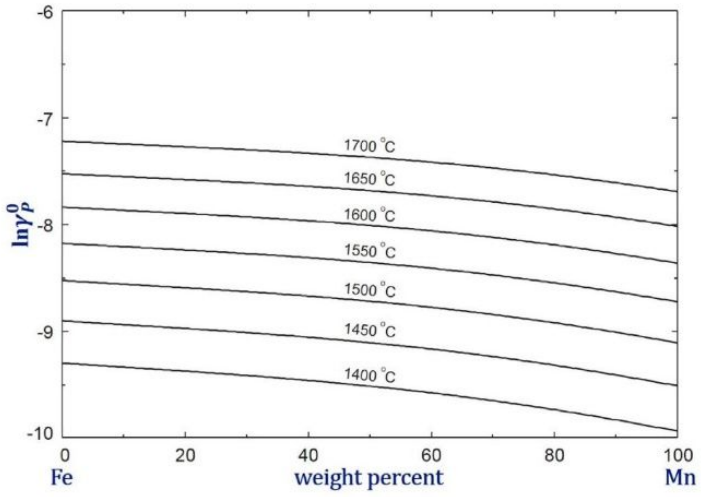

Figure 18: $ln\ (\gamma_P^0)$ of P in the Fe-Mn liquid smelting at different temperatures [66]

The activity coefficient of P (γ_P) and Mn (γ_{Mn}) were determined within equilibrium experiments by using silver and in carbon saturated smelting of Fe-P-Mn in a graphite crucible at 1673 K. Additionally, interaction parameters between Mn and P were depicted. [68] Figure

19 shows the dependence between $f_{P,}$ which is the activity coefficient related to mass fraction instead of mole fraction (γ_P), at an increasing content of Cr in the liquid molten bath and compared with various results from respective literature. [69]

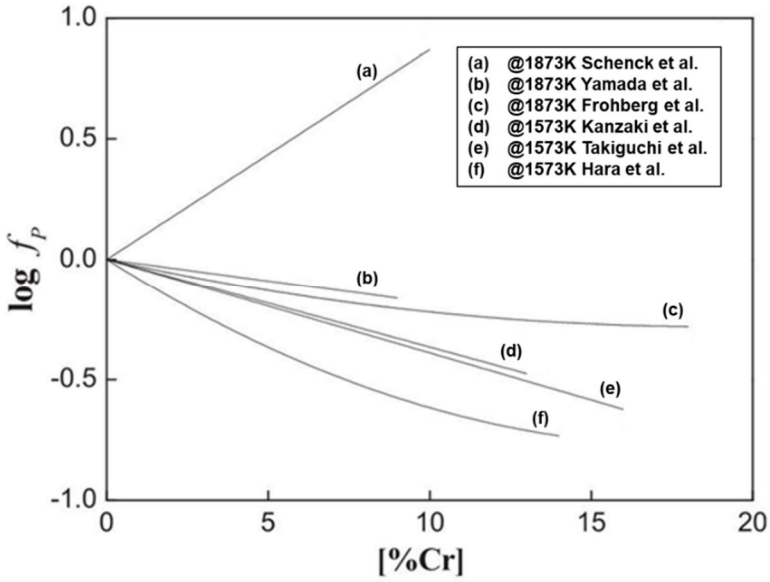

Figure 19: Dependence of f_P over a certain range of Cr-content in liquid iron at different temperatures - cited literature: (**a**) [70], (**b**) [71], (**c**) [72], (**d**) [73], (**e**) [74], (**f**) [75], cf. [69]

The results demonstrate that five out of six sources follow a downward tendency. All gathered data refers to temperatures of 1573 K, or 1873 K, respectively. Additionally, the impact of C-solubility on P is also named and examined. Lower amounts of C in the metal result in a considerable reduction of γ_{Cr}. The same effect can be seen at low Cr concentrations at higher Si contents in the metal phase. While higher temperatures promote and Si hinders the reduction of CrO, it can be stated that higher basicity values have an increasing effect on the activity of CrO. [23] However, Schlesinger et al. (2002) present a large database of relevant thermodynamic properties such as heat capacity, formation enthalpy, and Gibb's energy for a wide variety of different phosphides, including these of Fe, Cr, and Mn.

The evaluation of possible reactions which tend to result in the formation of phosphides are considered below. Since this thesis aims at the P-behaviour during carbo-thermal treatment of Fe-, Cr-, and Mn-bearing synthetically produced slags, the formation of Fe-phosphides is discussed first. Equation 2-42 – 2-45 should give an overview of potential phosphides resulting from an interaction between Fe and gaseous P_2. [59,61]

$$3[Fe] + \frac{1}{2}\{P_2\} \leftrightarrows [Fe_3P] \qquad \textbf{2-42}$$

$$2[Fe] + \frac{1}{2}\{P_2\} \leftrightarrows [Fe_2P] \quad \textbf{2-43}$$

$$[Fe_2P] + \frac{1}{2}\{P_2\} \leftrightarrows 2[FeP] \quad \textbf{2-44}$$

$$[FeP] + \frac{1}{2}\{P_2\} \leftrightarrows [FeP_2] \quad \textbf{2-45}$$

Regarding ΔG at 1900 K expressed in Figure 20, Fe_2P is most likely to be formed from a thermodynamic perspective owing to the most negative value of -88 kJ/mol. According to Equations 2-44 and 2-45, it can be derived that some reactants serve as an intermediate from preliminary phosphide reactions, and in turn, result in species like FeP or FeP_2. This fact and the positive value of ΔG makes the formation of FeP_2 hardly possible. However, kinetic phenomena were neglected in this chapter. Fe_3P has the largest Fe/P_2 ratio, six times higher than FeP_2. In general, based on the high contents of Fe in BOFS, it can be stated that this ratio is sufficient for all mentioned iron phosphides. However, considering the composition of the novel BOFS presented in chapter 2.6.1, a Fe/P_2 ratio of 3.32 is calculated. Therefore, it can be assumed that in the case of treating the novel BOFS, Fe_2P is most likely to be formed. [59]

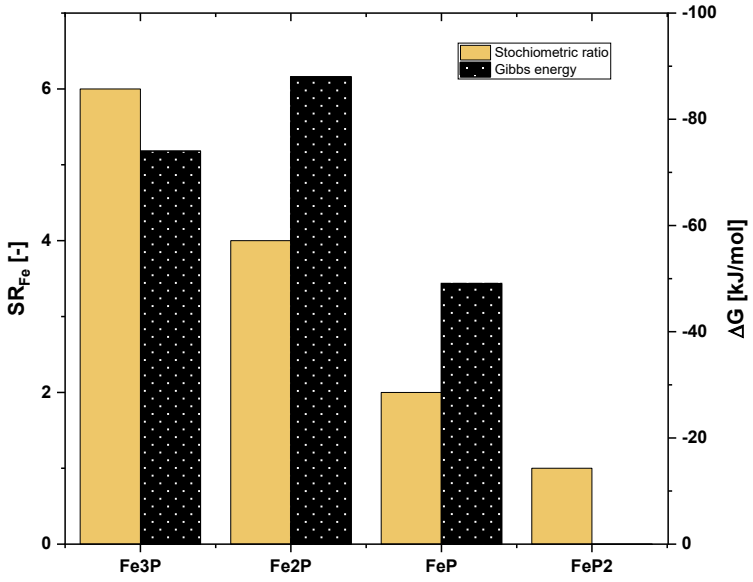

Figure 20: SR and Gibb's energy of Fe-phosphide formation at 1900 K, data from [61], cf. [59]

Considering Cr, the origination of potential phosphides (Cr_3P, $Cr_{12}P_7$ and CrP) are shown in Equations 2-46 - 2-48. [59,76]

$$3[Cr] + \frac{1}{2}\{P_2\} \leftrightarrows [Cr_3P] \quad \textbf{2-46}$$

$$\frac{8}{3}[Cr_3P] + \{P_2\} \leftrightarrows \frac{2}{3}[Cr_{12}P_7] \quad \textbf{2-47}$$

$$\frac{2}{5}[Cr_{12}P_7] + \{P_2\} \leftrightarrows \frac{24}{5}[CrP] \quad \textbf{2-48}$$

According to Figure 21, by far, the most negative value for ΔG can be seen for $Cr_{12}P_7$, whereas large amounts of Cr are needed because Cr_3P with a high SR_{Cr} as an intermediate must be formed first. Looking at the following reaction sequence, SR_{Cr} for CrP is even higher because of the former formation of Cr_3P and $Cr_{12}P_7$. However, a meagre Cr/P_2 ratio of 0.78 was calculated from the novel slag composition, depicted in Figure 14. In general, very low Cr-amounts compared to Fe, and Mn imply that a favoured formation of Fe-, or Mn-phosphides is very likely. [59]

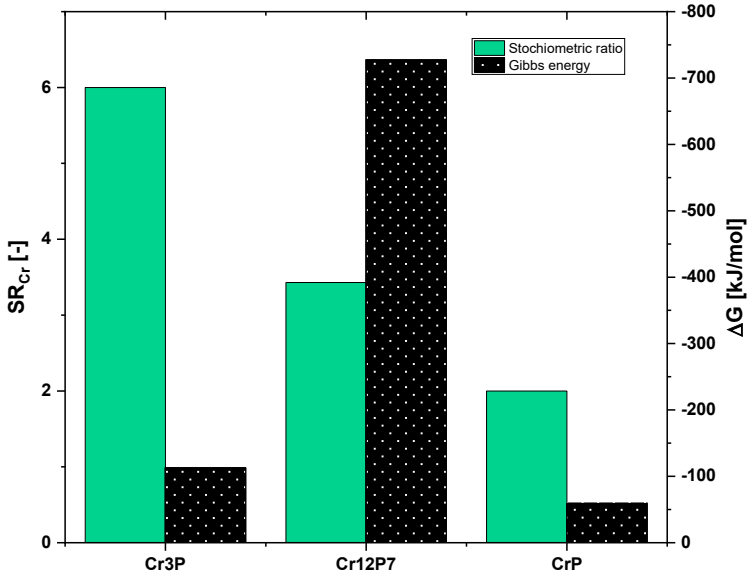

Figure 21: SR and Gibb's energy of Cr-phosphide formation at 1900 K, data from [61], cf. [59]

Concerning Mn-phosphides, except for Equation 2-53, Mn occurs as a gas in the remaining reactions (Equation 2-49 - 2-52). Another anomaly in the formation of MnP_3 is the presence of P_4(g) as a reactant. [59]

$$3\{Mn\} + \frac{1}{2}\{P_2\} \leftrightarrows [Mn_3P] \quad \textbf{2-49}$$

$$4\{Mn\} + \{P_2\} \leftrightarrows 2[Mn_2P] \quad \textbf{2-50}$$

$$3\{Mn\} + \{P_2\} \leftrightarrows [Mn_3P_2] \quad \textbf{2-51}$$

$$\{Mn\} + \frac{1}{2}\{P_2\} \leftrightarrows [MnP] \quad \textbf{2-52}$$

$$[MnP] + \frac{1}{2}\{P_4\} \leftrightarrows [MnP_3] \quad \textbf{2-53}$$

According to Figure 14**,** relatively high amounts of MnO are bound in the novel slag. Consequently, it led to an even higher calculated stochiometric ratio compared to Fe (SR_{Mn} = 3.34). However, by considering Figure 22**,** it can be concluded, that the formation of Mn_3P_2 is most likely. While the driving force (ΔG) for Mn_3P is also in an acceptable range, too much Mn is required (SR_{Mn} = 6.00). The origination of MnP_3 can almost certainly be excluded because of the prior formation of MnP and the simultaneous need for the attendance of P_4(g). [59]

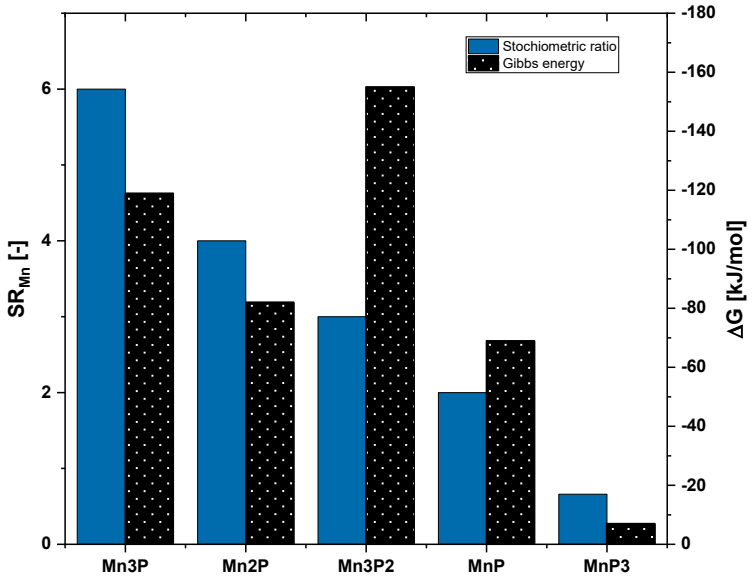

Figure 22: SR and Gibb's energy of Mn-phosphide formation at 1900 K, data from [61], cf. [59]

In conclusion, under the conducted considerations, the following phosphides are most likely to be formed during carbo-thermal treatment of the novel slag: Fe_2P and Mn_3P_2. In the case of Cr, it is hardly conceivable that any of the listed phosphides originates. However, it must be stated again that these considerations exclude kinetic phenomena. Furthermore, each single metal was examined separately and thus deviating results of phosphide formation processes

regarding an alloy of Fe, Cr, and Mn is highly probable. For the upcoming practical part, slag samples with different Fe, Cr, and Mn compositions are processed. As a result, for the occurring metal concentration, their reduction behaviour, and the stoichiometric ratio between P and the corresponding metal will be discussed in more detail.

2.7.2 Simulation results of slag reduction using FactSage™ [59]

This chapter includes comprehensive simulation results in FactSage™ ("FACT" stands for "Facility for the Analysis of Chemical Thermodynamics") conducted by Felix Breuer et al. (2021), simulating carbo-thermal treatment of Cr-, and Mn-bearing slags up to the maximum temperature of the InduMelt plant (1900 K). FactSage™ is a thermochemical software, modelling the behaviour of solutions in the field of thermodynamics and chemical engineering. In general, the adopted simulation module is based on achieving equilibrium. Thus, it limits the validity of gathered results since equilibrium is not reached during the application in the InduMelt. However, three different simulation series (A, B, and C) were carried out. By changing specific parameters, their impact on species allocation in the emerging phases is investigated. In addition, excess carbon ensured the complete reduction of all relevant species. The purpose of each simulation series is described below: [59]

- Simulation series A: Treatment of the novel slag presented in Figure 14 with coherent basicity of 1.5 within a temperature range between 1000 – 2000 K in 5 K steps is simulated, and the emerging phases are investigated.
- Simulation series B: The treatment of the novel slag from chapter 2.6.1 at 1900 K under varying Cr-, and Mn-quantities were simulated. Their amounts are changed in 5 m.-% steps in a range between 0 – 15 m.-%. Furthermore, the content is correlated to pure Cr, and Mn, whereas $B_2 = 1.5$ and kept constant in all simulations. Consequently, this series comprises of 16 simulations.
- Simulation series C: With the same slag composition as in simulation series A, the influence of B_2 on the reduction behaviour at a temperature of 1900 K is investigated. Therefore, B_2 values between 1.0 – 1.5 in 0.1 steps were altered. Hence, six simulations were carried out. [59]

For each simulation, 100 g of slag and an additional 50 g of carbon were selected, summing up to 150 g total input mass. Due to the deviation of the varying slag mixtures compared to the initial novel slag in series B and C, the remaining compounds stay in a constant ratio. [59]

2.7.2.1 Results from simulation series [59]

Results of simulation series A regarding the composition of the emerging slag-, metal- and gas-phase at 1900 K reveals the affinity between P and the liquid metal bath, which is shown in Table 5. Almost all P is bound in the metal, and only slight traces of P_2 can be detected. Mass balances resulted in 23.93 g gas, 43.22 g slag, and 25.05 g metal. [59]

Table 5: Simulation series A – Composition of the phases at 1900 K, cf. [59]

Gas phase species	m.-%	Slag phase species	m.-%	Metal phase species	m.-%
CO	98.330	CaO	49.31	Fe	35.66
Mg	0.750	SiO_2	33.85	Mn	34.48
Mn	0.540	MgO	8.42	P	20.77
P_2	0.330	Al_2O_3	6.77	Cr	8.22
SiO	0.030	MnO	0.42	C	0.46
CO_2	0.004	Ti_2O_3	0.39	Si	0.39

As depicted in Figure 23, the development of the P distribution from 1000 K until 2000 K indicates that the gasification is expected to start at 1600 K and increase rapidly at 1800 K. Moreover, the total amount of P, occurring as P_2O_5 in the initial slag, is 5.38 g. Until 1200 K P is predominantly bound in C_3P and gradually accumulates in the metal at higher temperatures. [59]

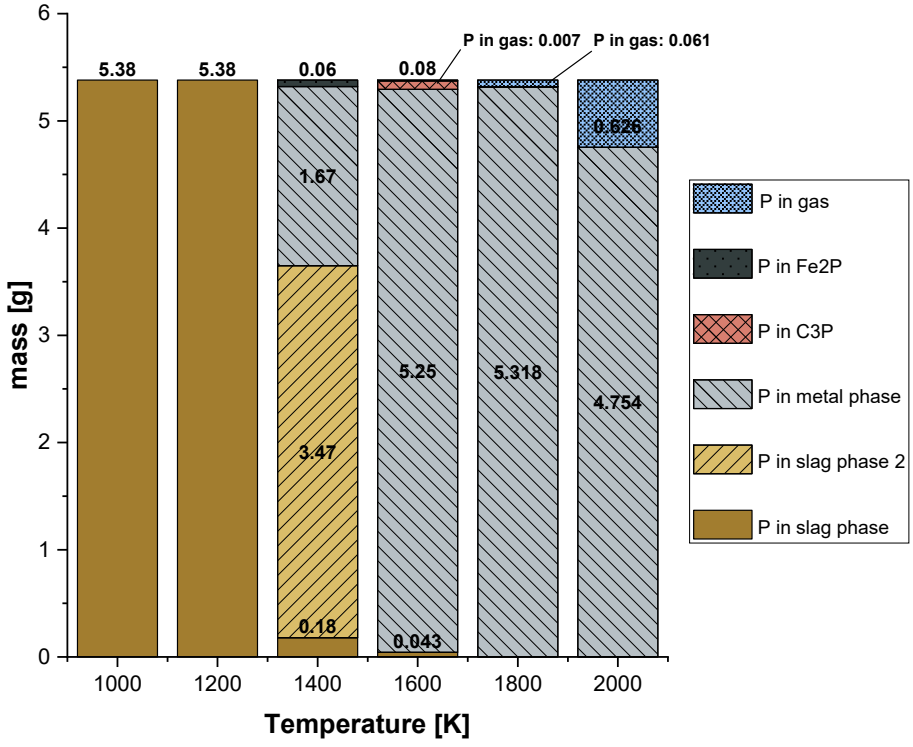

Figure 23: Results of simulation series A – P balance in a range between 1000 – 2000 K, cf. [59]

From the outcomes of 16 simulations in series B, higher Cr-, or Mn amounts lead to a significant deterioration of the PGD. As expected, the best results can be obtained without Cr, and Mn, which can be seen in Figure 24. At lower Mn contents (5 – 10 m.-%) without Cr (Sim5 and Sim9), the PGD compared to the reversed ratio (Sim2 and Sim3) is higher. However, the conversely phenomena can be observed regarding higher amounts of Mn (Sim13: 15 m.-% Mn and 0 m.-% Cr). In that case, less P is converted into the gas phase concerning Sim4 (0 m.-% Mn and 15 m.-%). By all other simulations (except Sim6), almost no phosphorus is gasified. [59]

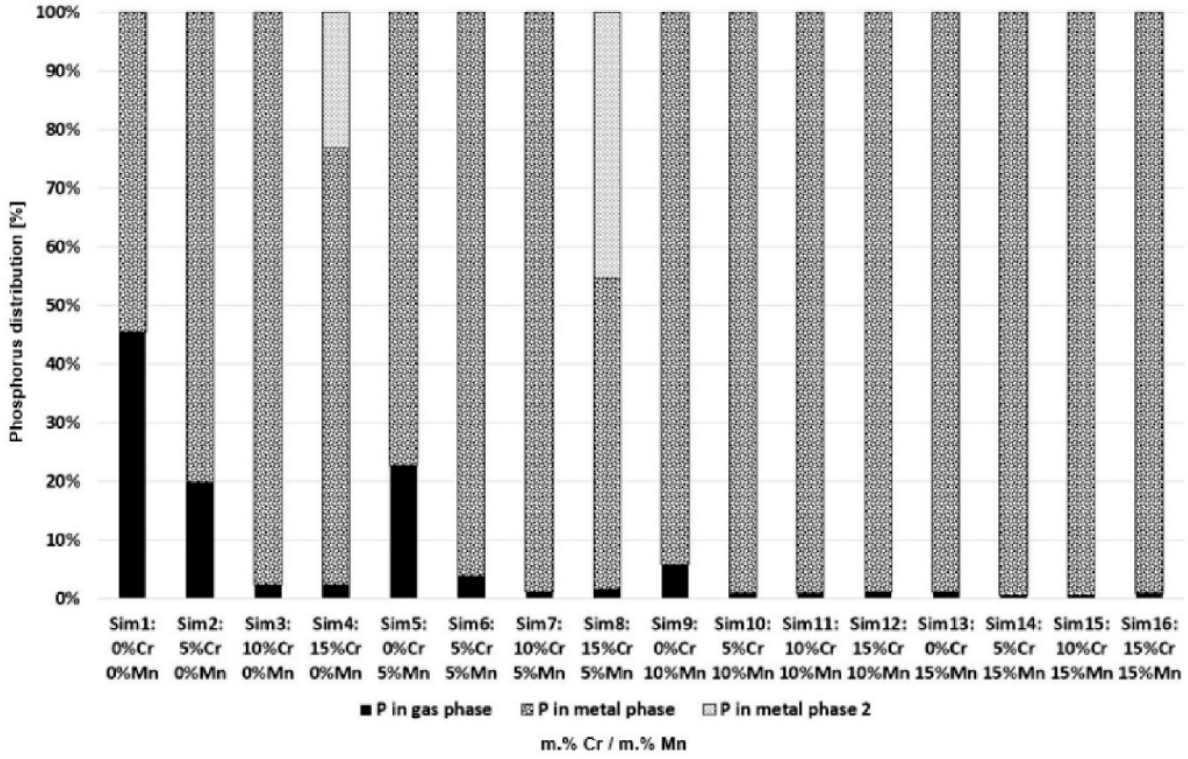

Figure 24: Results of simulation series B: P distribution between gas-, metal-, and metal phase 2 [59]

As already described, the activity of the involved compounds plays a considerable role in the formation process of phosphides. The lower the amount of Cr and Mn in the slag, the higher the P-activity, illustrated in Figure 25. In addition, the values from the heat map are in accordance with findings from various literature, as stated elsewhere. [59]

m.% Cr / m. % Mn	0 m.% Mn	5 m.% Mn	10 m.% Mn	15 m.% Mn
0 m.% Cr	Sim 1 0.023047	Sim 5 0.01562	Sim 9 0.0074478	Sim 13 0.0030873
5 m.% Cr	Sim 2 0.014105	Sim 6 0.0058418	Sim 10 0.0026971	Sim 14 0.0019688
10 m.% Cr	Sim 3 0.0045011	Sim 7 0.0028456	Sim 11 0.002324	Sim 15 0.0018749
15 m.% Cr	Sim 4 0.0040699	Sim 8 0.0031877	Sim 12 0.0024858	Sim 16 0.0019605

Figure 25: Results of simulation series B – Heat map of the P-activity regarding all 16 simulations [59]

Simulation series C exposes that a changing B_2 impacts the constitution between the metal and slag phase. Indeed, P in the gas phase is roughly the same for all conducted simulations, which is shown in Figure 26, and therefore no evident influence can be identified. [59]

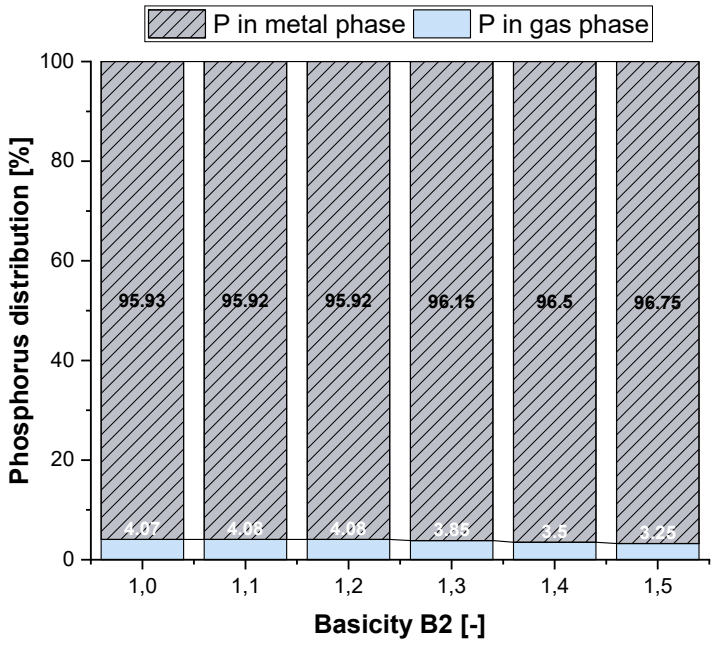

Figure 26: Results of simulation series C – P-distribution at different B_2 (1.0 – 1.5) of the novel slag cf. [59]

However, low B_2 values seem to hinder the P enclosure into the metal stronger than higher values, resulting in a slightly higher PGD. According to Figure 27 (Sima - B_2 = 1.0, Simf - B_2 = 1.5), this effect is even intensified significantly at higher temperatures (> 1800 K). [59]

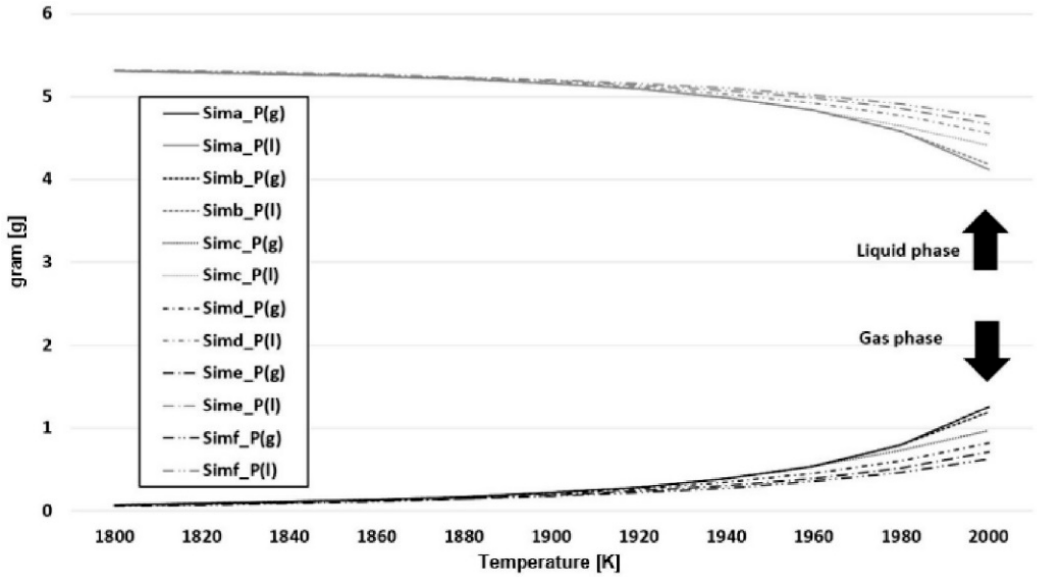

Figure 27: Results of simulation series C: Distribution of the P mass between liquid metal P(l) and gaseous P P(g) [59]

Important insights concerning thermodynamic simulation in FactSage™ were given in this chapter. Subsequently, a conclusion of the theoretical fundamentals summarizes the most important findings from the literature research. In a further step, obtained outcomes should serve as a reference and are validated by results from reducing Fe-, Cr-, and Mn-rich P-containing slags, which are produced synthetically in practical experiments (see chapter 3).

2.8 Conclusion from the theoretical fundamentals

Data from the global steel production reveals that giant amounts of slag from the BOF accumulate each year. Valuable metals with considerably high amounts of Fe, Cr, and Mn are bound into the slag matrix, remaining unused now. Merely minor P amounts in the BOFS prevent internal reuse in the steelworks because of their detrimental influence on steel properties. Furthermore, legal obstacles accelerate the necessity for a proper re-use solution. Carbo-thermal treatment using the InduRed concept, developed at the Chair of TPT at the MUL, is feasible, splitting up the input slag into three main mass streams: A nearly metal-free product slag, an almost pure metal-alloy, and a gas, consisting mainly of CO and P_2. However, problems related to the affinity between P and Fe has led to an approach of an altered process route for the internal recycling of BOFS. In two sub-steps, the initial slag from the converter must be modified, while an iron- and manganese-alloy is separated first before the novel BOFS enters the InduRed reactor. Despite lower iron-oxide contents in the input slag, results from

conducted experiments indicate that lower amounts of gasified phosphorus can be achieved. Moreover, more P is found in the obtained metal compared to treating common BOFS. These unexpected results reveal that the process of undesired phosphide-formation can also be attributed to metals like chromium or manganese. Assumptions made from these results could be supported by findings from various experiments or simulations carried out in respective literature. Considering thermodynamic and chemical aspects, potential phosphides could be identified. The most important outcomes affecting the process of phosphide formation are summarised as follows:

- Higher metal concentrations of iron, chromium, or manganese in the slag increase the probability of contact with phosphorus, implying a lower phosphorus gasification degree, leading to an increased phosphorus accumulation in the metal phase.
- Higher phosphorus and metal activity coefficients increase the formation of phosphides.
- The activity coefficient of phosphorus γ_P decreases with an increasing metal concentration in liquid metal baths.

These stated assumptions, excepting these including activity considerations, made above were validated by practical experiments. Hence, slags with different metal contents of Fe, Cr, and Mn were produced synthetically. Then the slag samples were reduced with carbon powder as a reducing agent at temperature of 1873 K. The final products, a metal, and a mineral phase, were analysed according to their composition to determine the affinity between P and Fe, Cr, or Mn. The objective of the conducted experiments is to get a better insight into the undesired phosphide formation behaviour during carbo-thermal treatment of different slag compositions. The line of action, and results from the experiments are introduced in the next chapter.

3 Practical experiments

Outcomes from the literature research revealed, that metals like iron, chromium, and manganese have a great affinity to phosphorus. Generally, phosphides originate during reduction processes of phosphorus-bearing slags at elevated temperatures, when molten metal is exposed to gaseous phosphorus. For a preferably pure obtained metal alloy by a simultaneous minimization of unwanted phosphide content within the metal product it is crucial to better understand the process behind phosphide formation. Hence, the last chapter of this thesis deals with the execution of two experiments, comprising of the production of synthetical slags by smelting adequate chemical amounts. Subsequently, a pyrometallurgical treatment step of each sample is carried out in an electrically heated furnace under inert gas purging providing a reducing atmosphere. Before the reduction experiment is performed, melting behaviour of the synthetic slag samples after reductant addition is examined in the respective temperature range with the aid of a heating microscope (HM). Important insights from the theoretical fundamentals serves as foundation for further considerations and are therefore applied to the experimental setup and operation conditions. This chapter starts with the experiment's objective and methodology, followed by the definition of necessary parameters required for experimental execution. Then the execution of experiments consisting of smelting, melting behaviour evaluation, and reduction are explained, while results are introduced and discussed afterwards. Finally, a short research prospect is given at the end, highlighting suggestions for improvements about future experimental setups and targets for the carbo-thermal reduction of phosphorus containing slags with certain ranges of iron-, chromium-, and manganese-contents.

3.1 Experimental objectives

The experiments conducted in the course of this thesis aims in a better understanding of the behaviour between phosphorus and metals like iron, chromium, or manganese during carbo-thermal treatment of synthetically produced slags. For this reason, the tendency of phosphide formation for each sample is evaluated by examining the distribution of phosphorus between the emerging mineral- and metal-phase after reduction. The gas phase formed during the process was not analysed and is therefore not subject of considerations. In total, the investigated materials consist of six synthetically produced slag samples with different compositions of either iron, chromium, or manganese with once lower and once higher metal concentrations.

3.2 Experimental Methodology

The approach and the applied methodology of the smelting, melting behaviour evaluation, and reduction experiment are given in this chapter. An overview of the whole experimental line of action can be taken from Figure 28.

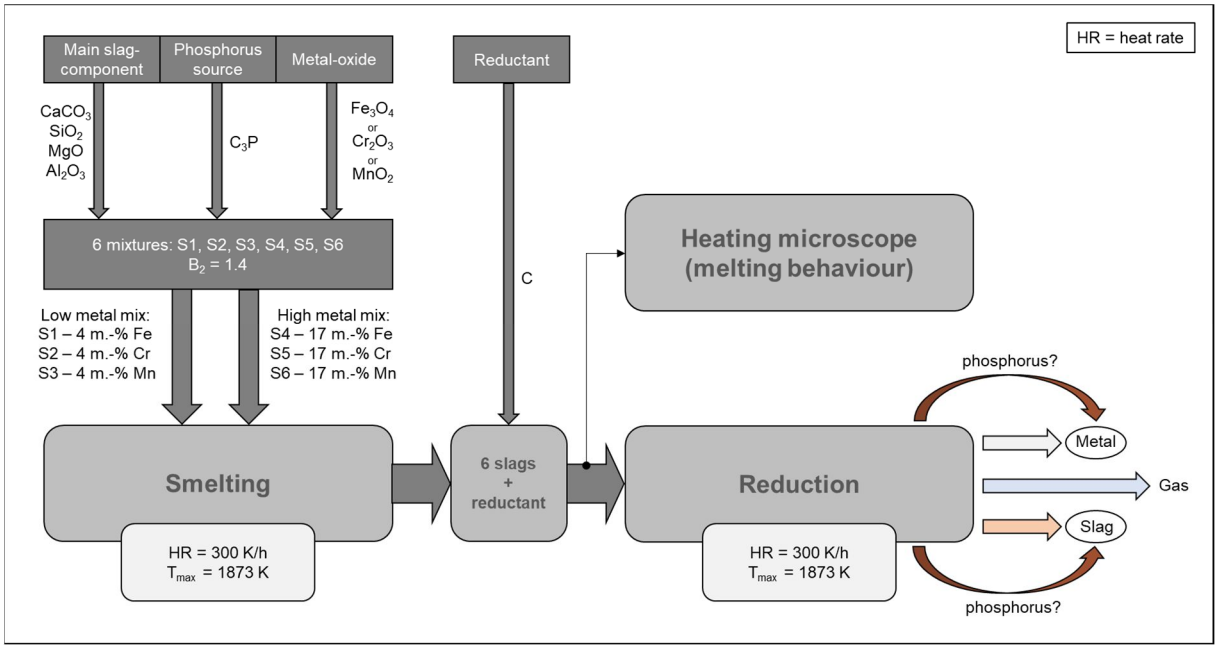

Figure 28: Overview of the experimental procedure of smelting, melting behaviour evaluation, and reduction

First, six synthetic slag samples are prepared by weighing and blending high purity chemicals of characteristic compositions, which will be discussed later in chapter 3.3.1. Afterwards all mixtures are smelted in MgO-crucibles, to obtain the slags as basic material for subsequent reduction. Cooled, and solidified slag, recovered from the crucibles is processed in a jaw crusher to obtain a uniform grain size. Then the amount of carbon for an entire reduction of all crucial species with an excess amount of 25% is calculated stoichiometrically and added to the slag samples afterwards. The melting behaviour of the slag-carbon mixture were examined in a heating microscope. Consequently, samples are reduced in the same type of crucibles as for the smelting experiment. Due to technical problems with the original furnace in which the synthetic slags were produced, reduction experiment was conducted in an electrical furnace at the Chair of Nonferrous Metallurgy. The formed product slag and metal phase after reduction were recovered, separated, and weighed. Then all phases were analysed using inductively coupled plasma optical emission spectrometry (ICP-OES). The same method was applied analysing a part of the synthetically produced slag samples.

Smelting experiment was carried out in an industrial electrically heated so-called elevator furnace (EF) of the type ELHT 16/18 from the company Thermconcept at the Chair of TPT. Ten pieces of heating rods made of molybdenum-silicide ($MoSi_2$) ensure the heat input and an exhaust ventilation enables the removal of gaseous compounds from the reaction zone at the top of the EF through a hole. The bottom platform of the furnace chamber is accessible by moving it down- and upward in the same way as an elevator, which gives the furnace the appropriate name. In addition, the furnace is basically designed for opening the furnace chamber during very high operation temperature without destroying the refractory lining due to thermal shock. The maximum operation temperature of the EF is specified with 2073 K, while lower temperatures for continuous operation need to be used. Furthermore, the furnace is equipped with an integrated advanced temperature controller and programmer (Eurotherm 3508) where an adjustment of the heating and cooling programme can be defined manually or with the software iTools 3500 from Eurotherm. Hence, it enables a configuration and monitoring of different furnace parameter during the experimental execution, including power input in % of the maximum power, actual value, and set value of the inside temperature of the furnace chamber. Additionally, a thermocouple (TC) of type S is mounted at the top of the furnace, with the measuring tip protruding into the furnace chamber through the outlet hole at the furnace top. By using a measurement card of National Instruments, the received temperature data of the TC are reprocessed and stored using the software SignalExpress. Finally, after the heating-up process was performed, samples were cooled down very slowly by the programmed temperature curve. Because all samples are treated at the same time, the

crucibles are placed on a base made of refractory concrete. The whole experimental setup of the smelting experiment can be seen in Figure 29. Ar-gas wasn't used for smelting.

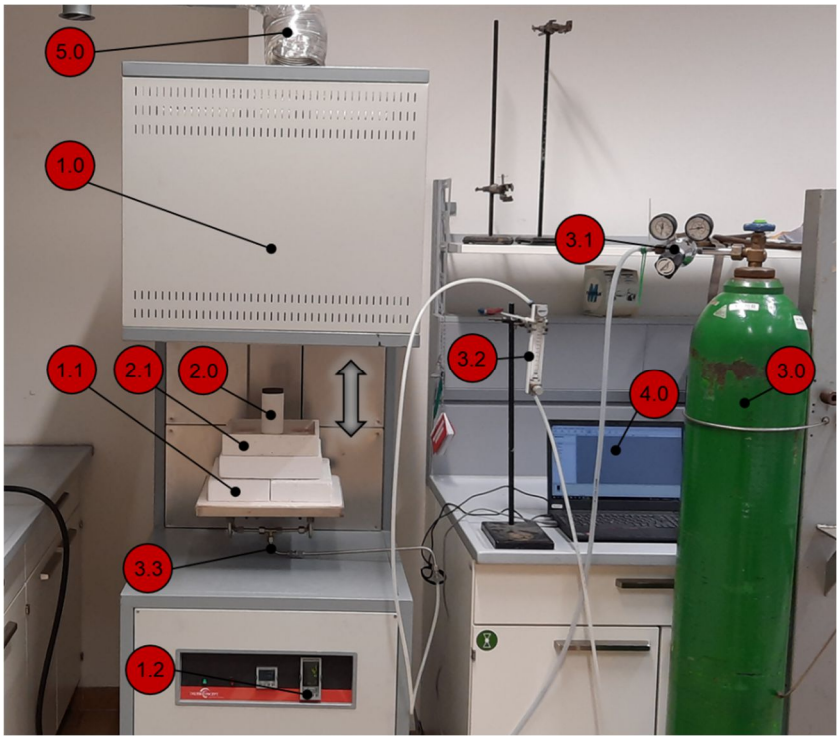

Numeration	Component	Classification
1.0	Elevator furnace ELHT 16/18 from Thermconcept (furnace chamber)	Furnace
1.1	Movable bottom panel	
1.2	Integrated advanced temperature controller and programmer (Eurotherm 3508)	
2.0	MgO-crucible	Crucible setup
2.1	Refractory-concrete-base	
3.0	Argon cylinder	Purge gas system
3.1	Argon pressure regulator	
3.2	Argon flowmeter	
3.3	Argon distribution (furnace inlet)	
4.0	Measurement laptop (iTools 3500)	Data recording
5.0	Exhaust ventilation	Product gas removal

Figure 29: Experimental setup and component description of the smelting experiment

For an estimation of the slag-carbon mixtures melting behaviour, all samples were evaluated in a heating microscope, whose setup is shown in Figure 30. The HM consists of an electrically heated furnace, an integrated TC, whereon the sample is placed during high temperature treatment, a gas purging system, a cooling system, comprising of hoses cooling the furnace with tap water, a light source, a camera, a power supply, and a computer for the evaluation of the measured data.

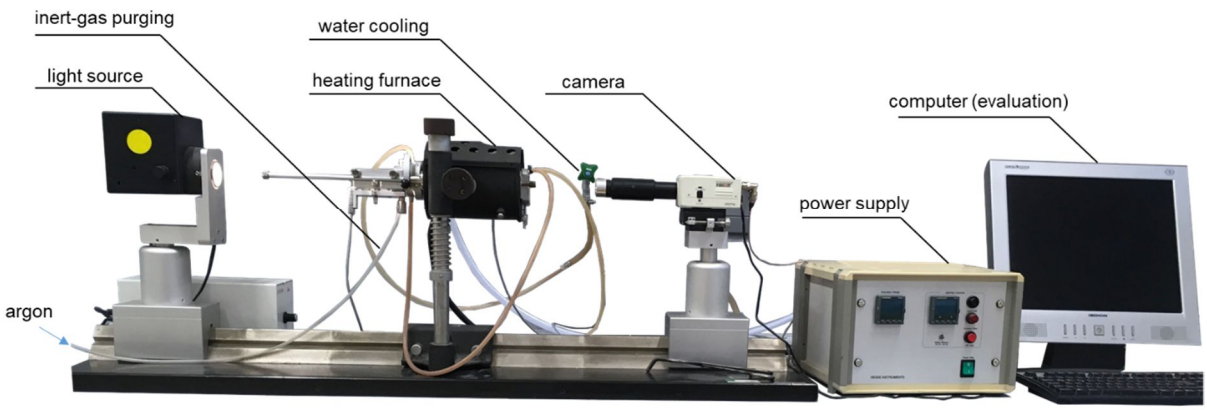

Figure 30: Component description and setup of the heating microscope

A cylindrical shaped sample, which is placed on a ceramic plate made of 99.7% Al_2O_3, formed by a press stamp is located on a thermocouple inside the furnace and illuminated frontally with a light source during operation. Images are taken of the samples silhouette over the whole heating-up process in a certain time interval by a camera. For this reason, deformations of the sample can be determined by the area change of the shadow, which is an indicator of proceeding melting or sintering processes owing to the rising influence by increasing temperature. Moreover, the softening temperature can be evaluated as well. By a specific percental decline of the initial shadow area, it can be assumed, that the mixture can be converted into a molten state under the set temperature conditions.

Due to technical problems with the EF after the smelting step, another furnace had to be used, which was kindly provided by the Chair of Nonferrous Metallurgy. This furnace from Nabertherm which is shown in Figure 31 is equipped with an exhaust hood. Therein a mechanical flap closes the furnace chamber at 1173 K and from this temperature on it does not allow exhaust gases to escape.

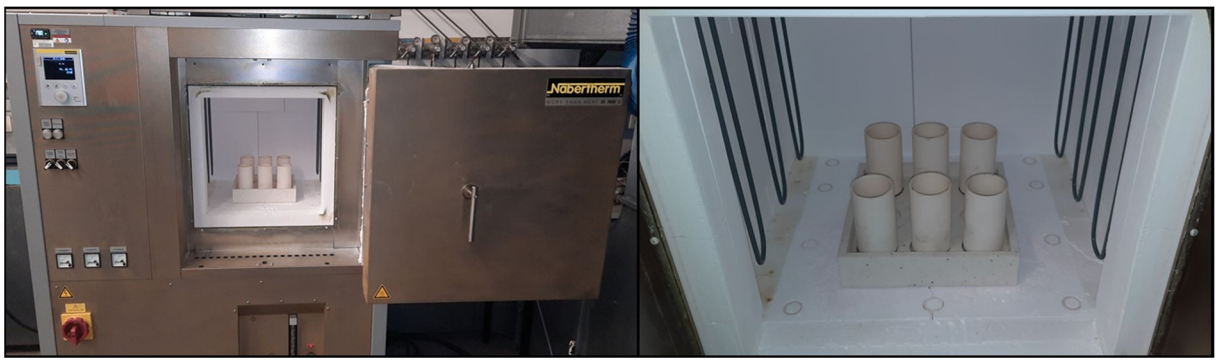

Figure 31: Experimental setup of reduction experiment

The same heating curve as for smelting was adjusted. Moreover, a continuous flow of argon (4 l/min) as purge gas provides an inert atmosphere within the furnace chamber, preventing false air suction by creating a slight overpressure.

The MgO-crucible of the same type for smelting and reduction has an outer diameter of 55 mm and a height of 95 mm with a median tare weight value of around 230 g. A bottom plate, made of graphite is located under the MgO-crucible optimizing the input of thermal radiation. An outline of the crucible setup during reduction experiment is given in Figure 32. The placement of the samples, which are simultaneously treated inside the furnace chamber, is depicted in Figure 31 on the right-hand side. For smelting, the MgO-crucible is simply placed in the recess of the refractory-concrete-base without the graphite bottom support and without carbon as reductant respectively.

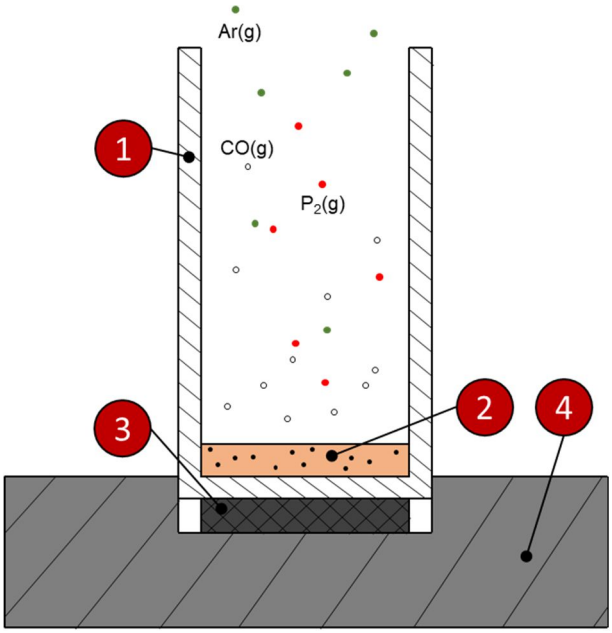

Figure 32: Setup of MgO-crucible during carbo-thermal reduction – **1**: MgO-crucible **2**: slag-carbon mixture **3**: graphite plate **4**: refractory concrete base

The principle of the introduced packed bed reactor concept presented in chapter 2.5.2 with the associated beneficial characteristics derived from it can't be applied to the setup of the common carbo-thermal reduction experiments conducted in this thesis. Graphite pieces, providing a large reaction surface are totally missing and the heat input system distinguished from electromagnetic induction. Furthermore, reaction gases are not removed continuously during operation. Generally, it can be expected, that at the investigated temperature range phosphide formation takes place spontaneously as long as P_2 and the respective metal are exposed to each other. However, the objective of this work is not reaching high PGD, but to

investigate the tendency of phosphide formation, regarding metals like iron, chromium, and manganese after pyrometallurgical high temperature reduction.

3.3 Evaluation of experimental parameters

For an adequate experimental execution various parameters need to be addressed including the composition of the slag samples, and an appropriate temperature range for smelting, transferring all chemicals into a liquid state. Furthermore, reduction temperature for all relevant species as well as the required reductant amount are evaluated subsequently. According to the relation between the amount of metal and phosphorus in the respective slag sample combined with thermodynamic considerations, the expected phosphide-compounds can be deduced from these parameters and is implemented at the end of this chapter.

3.3.1 Generation of synthetically Fe-, Cr- and Mn-rich P-containing slags

Six slag samples (S1 – S6) merely consisting either of lower or higher amounts of iron, chromium, or manganese are first synthetically produced. For each sample the mass of all representative slag forming components and quantity of metal were calculated and are illustrated in Table 6.

Table 6: Calculated composition of the synthetic slag samples (S1 – S6)

Chemicals	**S1 [g]**	**S2 [g]**	**S3 [g]**	**S4 [g]**	**S5 [g]**	**S6 [g]**
Fe_3O_4	1.82	-	-	7.22	-	-
Cr_2O_3	-	1.81	-	-	7.43	-
MnO_2	-	-	2.04	-	-	7.95
C_3P	1.01	1.02	1.00	1.00	1.04	0.98
SiO_2	10.05	10.05	10.00	8.56	8.49	8.37
$CaCO_3$	25.68	25.67	25.53	21.72	21.50	21.24
(CaO)	**(14.40)**	**(14,40)**	**(14.30)**	**(12.17)**	**(12.05)**	**(11.90)**
Al_2O_3	0.57	0.58	0.57	0.6	0.61	0.59
MgO	0.86	0.87	0.86	0.9	0.92	0.88
total	39.99	40.00	40.00	40.00	39.99	40.01

Commercially available chemicals in powder form (>97% purity) were weighed and finally blended in a MgO-crucible. As already stated in the theoretical fundamentals, oxides of Fe, Cr, and Mn in steelmaking slags appear mostly as Fe_2O_3, FeO, Cr_2O_3, CrO, and MnO. [12,14,18,22,23] Though, Fe_3O_4 and MnO_2 are deployed as oxides for slag samples in this thesis, which differ from the stated common slag constituents. However, the occurrence

of metal oxides by examining the final oxidic state after the smelting experiment will be ascertained later. Basicity is kept constant (B_2 = 1.4) by varying the amounts of $CaCO_3$ and SiO_2, while the quantity for all other slag constituents (C_3P, Al_2O_3, MgO) is consistent. As a result, before smelting, the total mass of each sample adds up to 40 g. $CaCO_3$ serves as the CaO-source for the up-coming experiments. According to the endothermic reaction character (ΔH_R = 178 kJ/mol), $CaCO_3$ begins to decompose at temperatures greater than 1153 K with the formation of CaO and CO_2 according to Equation 3-1, accelerating at rising temperatures. [77,78]

$$(CaCO_3) \leftrightarrows (CaO) + \{CO_2\} \qquad \textbf{3-1}$$

For this reason, a certain mass loss of the original slag (40 g) is expected, whereby 44% of the initial $CaCO_3$ mass is lost by its decomposition in terms of calculation. For this reason, it is provided that CaO is solely existent after smelting, bound into the slag system. The calculated aggregate mass after the smelting step based on the occurring elements can be seen in Figure 33 (left hand side). Summarized, the proportion for each metal (Fe, Cr, and Mn) totals to around 4 m.-% for slags with lower metal concentration (S1, S2, and S3) and approximately 17 m.-% for high metal concentrated slags (S4, S5, and S6) covering a wide scope of metal content, which is given by the elemental composition in Figure 33 on the right hand side. Due to a nearly identical metal composition of each sample, a direct mutual comparison between any individual metal and phosphorus can be made regarding the tendency of phosphide formation.

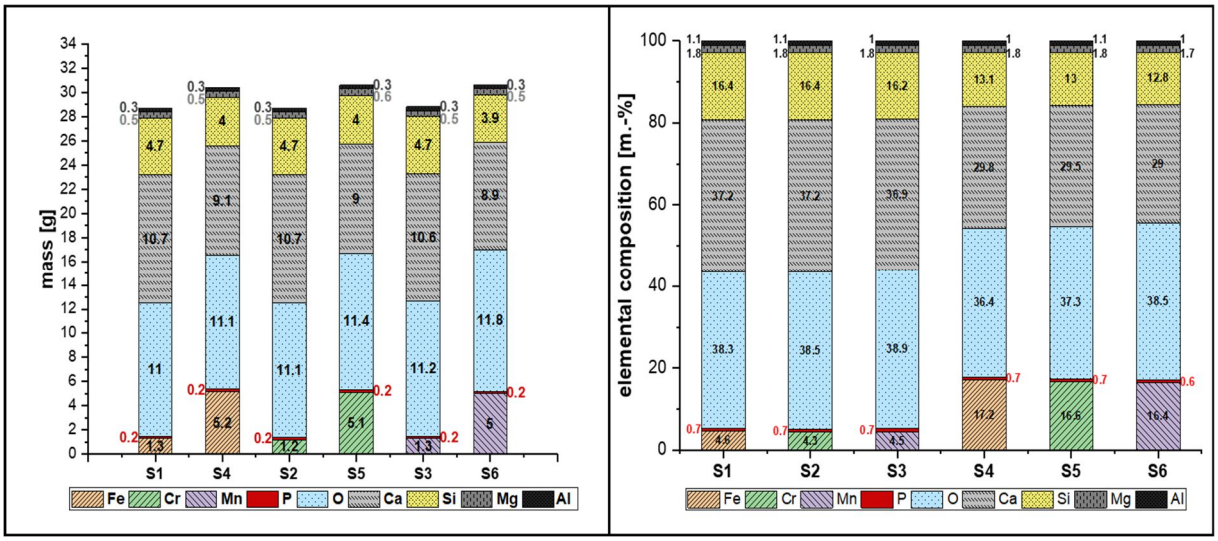

Figure 33: Calculated values: Element's mass and elemental composition of synthetic produced slag samples (S1 – S6)

3.3.2 Reductant demand, expected species after smelting and reduction behaviour

Carbon from pellets, processed to powder in a hammer mill is used as reducing agent. It offers a great reaction surface, producing CO-gas during direct reduction processes by consuming the oxygen from the involved oxide with the restriction that it takes place under inert conditions. Either gaseous carbon monoxide reacts in the form of indirect reduction processes, which will be discussed later or leaves the furnace chamber via the flue. Therefore, pure gas-gas reactions can be neglected for this work. The amount of carbon, required for a complete reduction at the maximum operation temperature was determined stoichiometrically. For this reason, it was assumed that 5% of the SiO_2 content in the slag will be reduced. The remaining components were entirely reduced with exception of CaO, MgO, and Al_2O_3. For these species, the maximum operation temperature for reduction is too low. Hence, this affects metal oxides of iron, chromium, or manganese in the respective slag sample and of course C_3P. 25% supplementary carbon powder quantity is added to the calculated minimum carbon quantity, providing enough reducing agent.

Before the reduction mechanism can be considered in more detail, it must be known which type of compound is existent after the smelting experiment e.g., oxidic state of metals and phosphorus-species. Owing to the lack of knowledge about the phases and compounds of each element integrated into the slag, all components, which are regarded for reduction in the relevant temperature window are discussed separately. Consequently, thermal stability and possible formation of specific oxides are investigated.

In the case of iron, commercially available Fe_3O_4 (iron (II, III)-oxide - purity grade >97%) was applied for the samples S1 with low Fe-content and S4 with high Fe-content. Findings in literature regarding thermodynamic considerations report, that the thermal stability of Fe_3O_4 in iron ore is given up to temperatures below 1773 K, which can be seen in Equation 3-2 and 3-3. Moreover, the decomposition behaviour is also dependable on the partial pressure of oxygen p_{O_2} concerning Equation 3-4, while p^0 is the reference pressure of the system, usually 1 atm and ΔG^0 is the standard Gibb's free energy in J/mol·K. [79] For this reason it is assumed, that FeO content is substantial, but also minor amounts of Fe_3O_4 can be found after smelting.

$$2Fe_3O_4(s) \leftrightarrows 6FeO(l) + O_2(g) \qquad \textbf{3-2}$$

$$\Delta G^0 = 858200 - 392.6 \cdot T\ [J/mol \cdot K] \qquad \textbf{3-3}$$

$$\ln\left(\frac{p_{O_2}}{p^0}\right) = -\frac{\Delta G^0}{R \cdot T} \qquad \textbf{3-4}$$

Cr-composing slags were S2 (low Cr-content) and S5 (high Cr-content). Chromium (III)-oxide (purity grade ≥98%) were used for these samples and it is also presumed according to the literature that this compound can be found after the smelting experiment in the slag matrix. [80]

In terms of manganese-containing samples, which are S3 with low Mn-content and S6 with high Mn-content, the substance MnO_2 (manganese (IV)-oxide - purity grade ≥98%) was added. It is stated, that MnO_2 under inert conditions is not stable at temperatures above 753 – 738 K, whereby Mn_2O_3 is formed as a product of decomposition. Under even warmer conditions, Mn_3O_4 is the most stable Mn-oxide at temperatures higher than 948 – 998 K owing to the degradation of Mn_2O_3. In comparison to an oxidising atmosphere, MnO_2 exists to 773 K, Mn_2O_3 until 1173 K and Mn_3O_4 can be stable to 1873 K. [81] Thus, Mn_3O_4 is expected in the slag after smelting.

For phosphorus containing compounds (C_3P) thermal stability is proven at temperatures, which are even higher than 2073 K and until these values no gaseous compounds (P_2O_5) are expected to be formed due to thermal decomposition. Therefrom, C_3P is used for further considerations. [82]

After these deliberations, metal oxides in the form of Fe_3O_4, FeO, Cr_2O_3, and Mn_3O_4 and C_3P as phosphorus species can be expected after smelting experiment and are taken into account as reactants for additional considerations regarding reduction behaviour. Furthermore, since it is also assumed that small amounts of SiO_2 will be reduced due to possible temperature peaks their reduction mechanism needs to be investigated as well.

3.3.2.1 Metal oxide reduction

Basically, the process of reduction can be divided into indirect and direct reduction. In the former, carbon monoxide as reaction partner lead to the formation of carbon dioxide according to Equation 3-5, while in the latter solid carbon serves as reductant and CO as final oxidation product originates, which is illustrated in Equation 3-6. [25]

$$\left(Me_xO_y\right) + y\{CO\} \leftrightarrows x[Me] + y\{CO_2\} \qquad \textbf{3-5}$$

$$(Me_xO_y) + y\ C \leftrightarrows x[Me] + y\{CO\} \quad \textbf{3-6}$$

For the identified metal oxides made above (Fe_3O_4, FeO, Cr_2O_3 and Mn_3O_4) as well as for SiO_2 and possible P-containing compounds thermodynamic calculations were performed regarding reduction reactions in HSC Chemistry 7.1. First, indirect reduction is discussed, while direct reduction behaviour of respective metal oxides is presented afterwards. The same is carried out for phosphorus species. For that reason, the following indirect reduction reactions of respective metal oxides can be ascertained, considering, that one mole of oxygen is involved, see Equation 3-7 – 3-14.

$$2(Fe_3O_4) + 2\{CO\} \leftrightarrows 6(FeO) + 2\{CO_2\} \quad \textbf{3-7}$$

$$2(FeO) + 2\{CO\} \leftrightarrows 2[Fe] + 2\{CO_2\} \quad \textbf{3-8}$$

$$2/3(Cr_2O_3) + 2\{CO\} \leftrightarrows 4/3[Cr] + 2\{CO_2\} \quad \textbf{3-9}$$

$$2(Mn_3O_4) + 2\{CO\} \leftrightarrows 6(MnO) + 2\{CO_2\} \quad \textbf{3-10}$$

$$2(MnO) + 2\{CO\} \leftrightarrows 2[Mn] + 2\{CO_2\} \quad \textbf{3-11}$$

By reference to possible indirect reduction reactions relevant for this thesis thermodynamic parameters as the reaction's enthalpy-, and entropy-change as well as the free Gibb's energy are summarized in Figure 34.

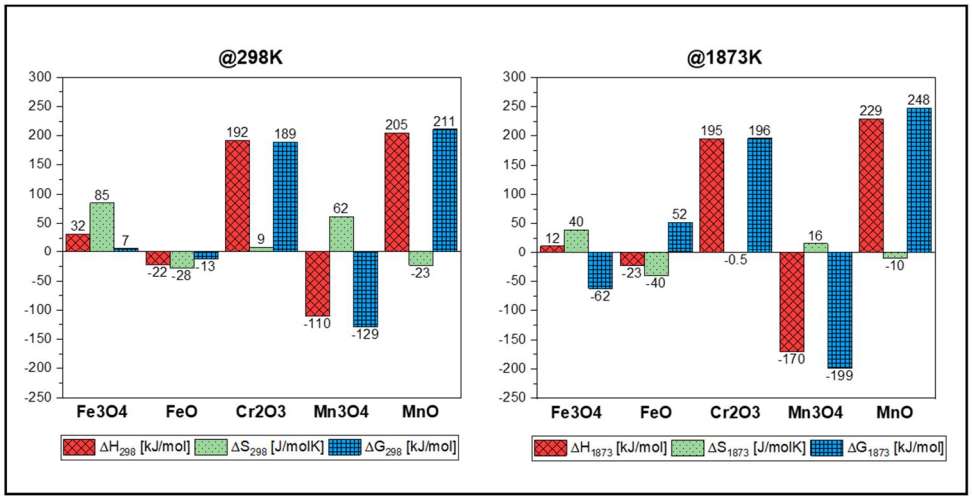

Figure 34: Indirect reduction reaction parameters of Fe-, Cr-, and Mn-oxides with one mole oxygen at 298 K and 1873 K [83]

Thermodynamic parameters at characteristic temperatures (298 K and 1873 K) are defined in order to illustrate their development during experiment execution. Exothermic or endothermic behaviour can be determined by the trend in the observed temperature interval, whereby high temperatures promote endothermic (+ΔH), and low temperatures fostering exothermic (-ΔH) reactions. Moreover, findings about the voluntary nature of indirect reduction reactions are given by the expression of the free Gibb's energy. The scheme for indirect reduction mechanism of solid metal oxides is quite similar for all observed species, resulting in an identical number of gaseous substances (in mole) on the reactant and product side. For example, the sequence of iron oxide reduction for sample S1 and S4 is comparable to processes that take place in a BF: Fe_3O_4 (RD = 11.1%) is first reduced to FeO (RD = 33.3%) and then metallic iron (RD = 100%) will be generated. While for example indirect reduction of Fe_3O_4 shows minimal endothermic characteristics, that of FeO is minor exothermic at 298 K. Despite exothermic reactions are favoured at lower temperatures and ΔG shows negative values at 298 K up to around 550 K, what applies to FeO, it must be available in sufficient quantities. Furthermore, abundant carbon monoxide must be emerged, and retention time need to be high enough. All these factors must be ensured for indirect reduction and cannot be guaranteed in case of FeO. However, at higher temperatures enough carbon monoxide formed from direct reduction reactions, makes indirect reduction feasible, particularly for Mn_3O_4, and Fe_3O_4. In addition, Mn-oxides in the slag samples reveal an analogous reaction sequence to Fe-oxides: Mn_3O_4 is first reduced to MnO, and then metallic Mn is formed. Cr_2O_3 is not concerned in indirect reduction processes according to the investigated parameters. To sum up, indirect reduction manifest as impossible at lower temperatures for all species (<1000 K). Conversely, at higher temperatures due to the increasing formation of CO from

direct reduction, indirect reduction reactions can contribute to the removal of oxygen from the respective oxide. However, gaseous compounds are removed from the furnace chamber continuously, reducing the reaction time and can therefore affect indirect reduction negatively.

In addition to direct reduction of FeO, Cr_2O_3, and MnO, which was already shown in Equation 2-29 – 2-32, further highlighted reactions of involved Fe-, and Mn-oxides species, but also reactions involving SiO_2 can be seen in Equation 3-12 – 3-15. On the other hand, SiO_2 can also be reduced with carbon to gaseous SiO, according to Equation 3-16, but this happened only at very high temperatures greater than 1900 K. [14,83]

$$2(Fe_3O_4) + 2C \leftrightarrows 6(FeO) + 2\{CO\} \quad \textbf{3-12}$$

$$2(Mn_3O_4) + 2C \leftrightarrows 6(MnO) + 2\{CO\} \quad \textbf{3-13}$$

$$(SiO_2) + 2\{CO\} \leftrightarrows [Si] + 2\{CO_2\} \quad \textbf{3-14}$$

$$(SiO_2) + 2C \leftrightarrows [Si] + 2\{CO\} \quad \textbf{3-15}$$

$$2(SiO_2) + 2C \leftrightarrows 2\{SiO\} + 2\{CO\} \quad \textbf{3-16}$$

Thermodynamic data concerning direct reduction for metal oxides are given in Figure 35.

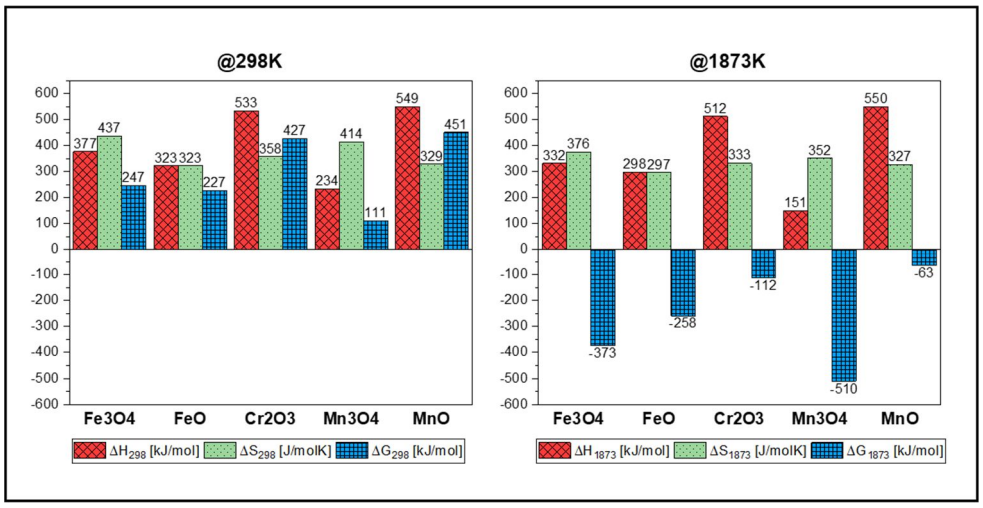

Figure 35: Direct reduction reaction parameters of Fe-, Cr-, and Mn-oxides with one mole oxygen at 298 K and 1873 K [83]

With direct reduction, more mole gases were produced resulting in a high positive entropy-change and all reactions show endothermic characteristics. While the free Gibbs energy at room temperature is positive for all species, it can be concluded that ΔG is rapidly declining with growing temperatures, which is validated by looking at the values depicted on the figure's right-hand side above. Therefore, thermodynamic considerations at operational temperature of reduction experiment implies that all metal oxides can be reduced. However, indirect reduction of SiO_2 can be excluded and extended calculations manifest that Equation 3-15 and 3-16 proceed thermodynamically between 1873 – 1973 K and therefore it is quite conceivable that uncontrolled temperature peaks can lead to a partial direct reduction of SiO_2. Additionally little mass loss of silicon can be supposed to take place due to the removal of gaseous SiO.

Aside from that, carbon monoxide production takes place for each mole consumed solid carbon during direct reduction processes. Furthermore, carbon monoxide can also be produced by the endothermic (ΔH^0 = 172.47 kJ/mol) Boudouard-reaction according to Equation 3-17. At temperatures around 1200 K an equilibrium is reached in favour of almost exclusively CO, while solid carbon is responsible for a low partial pressure of carbon dioxide. [25,84] However, only direct reduction can be the initial booster for subsequent indirect reduction mechanism by supplying carbon monoxide as reactant. Thus, CO_2 as a result of indirect reduction originates, which in turn reinforces carbon monoxide formation by consuming solid carbon fostered by the Boudouard-reaction.

$$C + \{CO_2\} \leftrightarrows \{CO\} \qquad \textbf{3-17}$$

Hosts of literature emphasizes the complexity of carbo-thermal reduction, while the process for iron-oxide-species is very well investigated, showing the already identified reaction sequence, from Fe_3O_4 reduction to metallic Fe. [85,86] The creation of iron-carbide (Fe_3C – cementite) during reduction of iron-ore pellets at different temperatures, gas compositions, exposure time, and material composition is studied. Highest cementite content in the reduced pellets is evaluated under a CO/H_2 atmosphere at 1100 K. [87] However, compared to the experimental setup in this thesis, an carbon monoxide atmosphere during reduction experiment is easily conceivable, but solid carbon powder as reductant is applied to the slag mixtures. Hence, a surplus quantity of carbon can potentially lead to a dissolution in the liquefied metallic iron bath at higher temperatures. This mechanism of dissolved carbon in liquid iron is investigated by four different approaches, which is intensified at temperatures between 1573 K – 1773 K. Moreover, silicon addition has no influence, but sulphur addition of 1 m.-% instead diminishes the carbon solubility-rate. [88] In case of Cr_2O_3 different species of chromium-carbides (Cr_3C_2, Cr_7C_3, and $Cr_{23}C_6$) as intermediates are first formed, involved in

direct and indirect reduction mechanism. Afterwards, a variety of different reaction pathways proceeds, stating that chromium-carbide species reacting either with CO_2, or Cr_2O_3 itself forming different chromium-carbides again or metallic chromium originates respectively. [82] The same is valid for MnO reduction, whereby also manganese-carbides like Mn_7C_3, and $Mn_{23}C_6$ are formed. Generally, the course of reduction is dependent on the participating gas atmosphere such as Ar, He, H_2, and mixtures of H_2-He, H_2-Ar, He-CO are used, whereas reduction proceeds slowest for Ar and fastest for H_2. H_2 is directly involved in reduction, either with the attendance of solid carbon, keeping the partial pressure of H_2O low, or it forms methane, accelerating this process owing to gas-solid reactions. Furthermore, higher temperatures promotes reduction processes, independently from different atmospheric compositions, while reduction with H_2 proceeds even at 1548 K totally after 60 min residence time. [89] Difficulties, according to sintering of molten slag around metal oxide particles (Mn_3O_4), which retarded reduction processes decelerating gas diffusion especially at lower temperatures. [81] Particle size of reductant as well as pre-processed material to be reduced has a significant effect on the reduction behaviour. [90]

3.3.2.2 Phosphorus-species reduction

Reduction reactions for P-containing compounds are shown in Equation 3-18 – 3-21. [84] For the gasification of phosphorus as a result of C_3P reduction with carbon considerably high amounts of SiO_2 are required, which results in the formation of $CaSiO_3$ (CS). Indeed, it is reported that reduction of C_3P with carbon monoxide is generally imaginable, but distinctly slower compared to direct reduction. [84] Furthermore, Equation 3-19 is important for supplementary temperature considerations with reference to the Richardson Ellingham diagram made in the next chapter. In addition, reduction mechanism for P_2O_5 representing both aggregate phases were given, while it is reported that C_3P is thermally stable also at very high temperatures, so that the formation of gaseous P_2O_5 can be excluded.

$$2/5(Ca_3(PO_4)_2) + 6/5(SiO_2) + 2C \leftrightarrows 6/5(CaSiO_3) + 2/5\{P_2\} + 2\{CO\} \quad \textbf{3-18}$$

$$2/5(Ca_3(PO_4)_2) + 2C \leftrightarrows 6/5(CaO) + 2/5\{P_2\} + 2\{CO\} \quad \textbf{3-19}$$

$$\frac{2}{5}(P_2O_5) + 2C \leftrightarrows \frac{2}{5}\{P_2\} + 2\{CO\} \quad \textbf{3-20}$$

$$\frac{2}{5}\{P_2O_5\} + 2C \leftrightarrows \frac{2}{5}\{P_2\} + 2\{CO\} \qquad \textbf{3-21}$$

$$2/5(Ca_3(PO_4)_2) + 2\{CO\} \leftrightarrows 6/5(CaO) + 2/5\{P_2\} + 2\{CO_2\} \qquad \textbf{3-22}$$

Thermodynamic parameters relating to phosphorus-containing species in HSC Chemistry 7.1 can be seen in Figure 36. The graphs designation of C_3P (SiO_2), C_3P, P_2O_5, and $\{P_2O_5\}$ relates to Equations 3-18 – 3-21 in the same order.

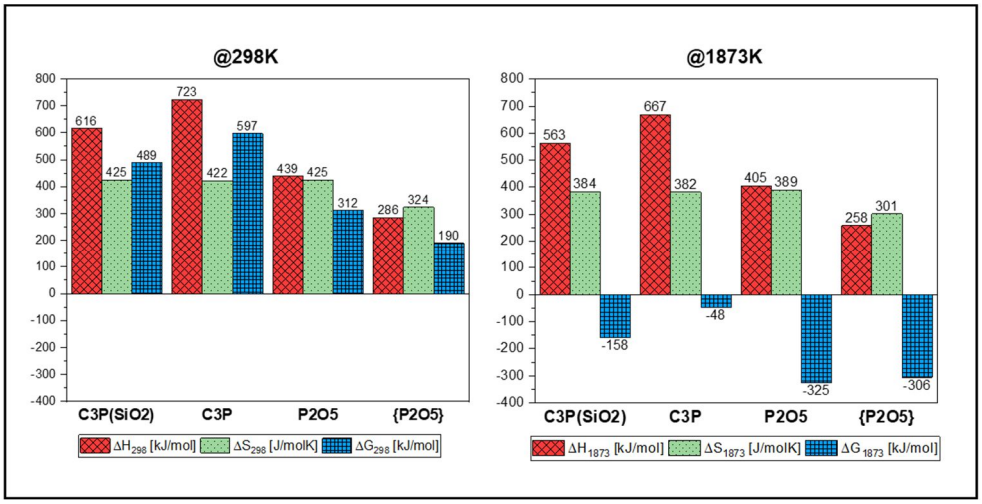

Figure 36: Direct reduction reaction parameters of possible P-containing species with one mole oxygen at 298 K and 1873 K [83]

Direct reduction reactions characteristics for P-containing compounds are endothermic and indicate a rapid decrease in free Gibb's energy with rising temperatures. At the maximum operation temperature (1873 K) all reactions occur spontaneously under these conditions. Indirect reduction for the same species is given in Figure 37, concluding that indirect reduction of gaseous and solid P_2O_5 seems to be possible at higher temperatures.

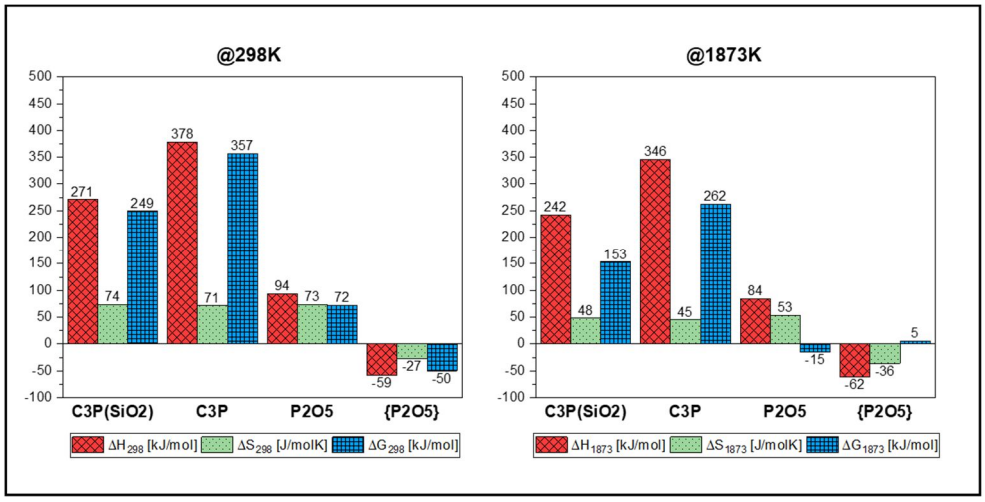

Figure 37: Indirect reduction reaction parameters of possible P-containing species with one mole oxygen at 298 K and 1873 K [83]

3.3.2.3 Summary of reduction behaviour

In summary, direct reduction can be stated as dominant oxygen removal process for respective oxides during reduction experiment. Indirect reduction instead might become more influential for merely a small number of species, but only at higher temperatures when carbon monoxide production becomes sufficient. However, only each individual component is considered separately disregarding the interfering influences within the multi-component slag system and reaction kinetics are not part of considerations as well. Furthermore, only direct, and indirect reduction of metal oxide species is investigated, whereby it is stated by outcomes from literature, that the participation of chromium-, and manganese-carbides, formed during the carbo-thermal reduction affects this process significantly. The beginning of phosphorus gasification undoubtedly is the critical initial ignition for phosphide formation. It can be concluded that metals are reduced either before or after phosphorus species were reduced, depending on which phosphorus compound (C_3P, P_2O_5) occurs in the slag sample and which species are additionally involved, e.g., SiO_2. In concrete terms, this means that phosphide formation is only preferred when gaseous phosphorus and a metal bath are existent simultaneously. Additionally enough contact time for ongoing reactions must be given, which is only possible if the metal oxide is reduced beforehand phosphorus compounds, and the emerged metal is present as a liquid molten bath. However, phosphide formation mechanism will be discussed in chapter 3.3.4.

3.3.3 Required temperature ranges and heating-up process

Necessary temperatures during the conducted experiments are both - smelting and reduction temperature. While the former must be high enough, liquefying the chemical powder mixture, transferring it into a slag-like material, the latter need to reach those temperature value to reduce relevant compounds completely. For this reason, the selected temperatures as well as the heating curves are described below.

For the smelting step, a temperature of 1873 K was chosen. Various sources mention melting temperatures between 1523 K – 1673 K, whereas slags in these literatures differ from typical BOFS compositions. [91,92] According to steelmaking slag from the converter, melting temperature for several batches with a mean value of 1718 K with a basicity B_2 = 3.5 – 4 were reported. [93] However, although samples of this work showing a lower basicity and differ in their composition, these values can be taken as a good approximation. Besides, the maximum achievable EF temperature in short-term operation is limited to 2073 K.

For a rough estimate of the temperature-window minimally required for direct reduction, the Richardson Ellingham diagram (see chapter 2.4.1) was used, where all depicted species are referred to the oxidation with one mole O_2. C_3P by contrast, is not depicted and therefore it needs to be drawn first. For this purpose, the mechanism proceeds by the attendance of CaO as reactant according to Equation 3-23. Relating to C_3P a reduction temperature of 1823 K is stated according to simulations in HSC Chemistry 7. [14]

$$\frac{6}{5}CaO + \frac{2}{5}P_2(g) + O_2(g) \leftrightarrows \frac{2}{5}Ca_3(PO_4)_2 \qquad \textbf{3-23}$$

The same was carried out for the reduction of Fe_3O_4 to FeO, Mn_3O_4 to MnO and solid P_2O_5 to gaseous P_2. The minimum temperature for the removal of 1 mole oxygen from the respective oxides relevant for this thesis are summarized by ascertain the intersection of each relevant metal oxidation straight line with the oxidation of solid carbon forming CO gas, according to Equation 2-28 and is summarized in Figure 38.

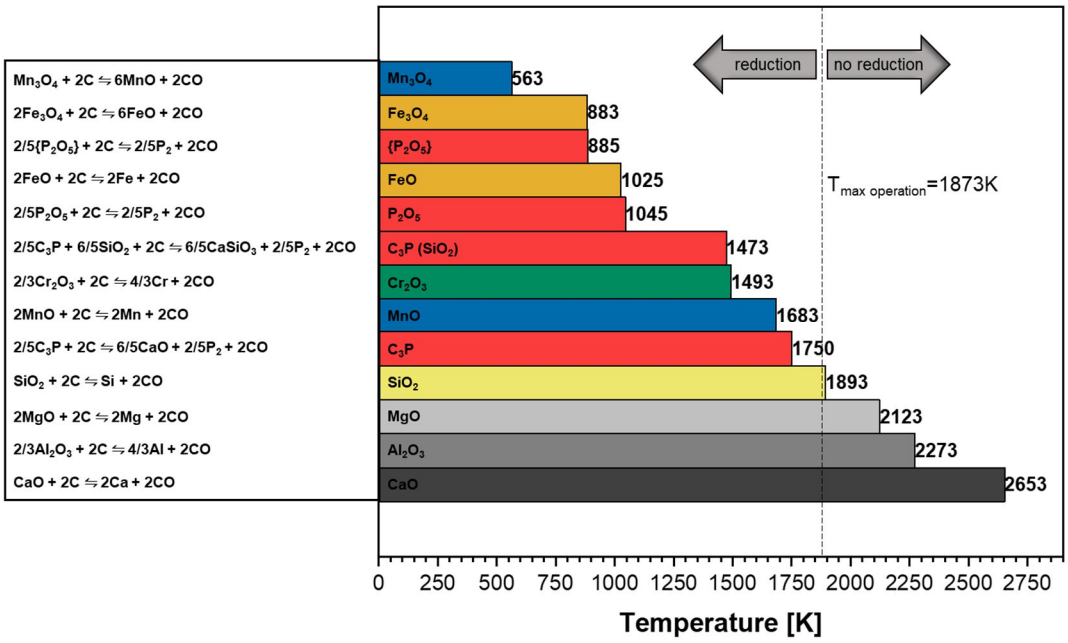

Figure 38: Minimum temperature required for direct reduction of all slag constituents related to one mole oxygen

Therefrom it can be deduced that Al_2O_3, MgO, and CaO according to Equation 3-24 – 3-26 cannot be reduced within the experiments in the EF.

$$\frac{2}{3}(Al_2O_3) + 2C \leftrightarrows \frac{4}{3}[Al] + 2\{CO\} \quad \textbf{3-24}$$

$$2(MgO) + 2C \leftrightarrows 2[Mg] + 2\{CO\} \quad \textbf{3-25}$$

$$2(CaO) + 2C \leftrightarrows 2[Ca] + 2\{CO\} \quad \textbf{3-26}$$

The occurrence of temperature peaks can certainly lead to a partly reduction of SiO_2. All other species including the oxides of Fe, Cr, and Mn are totally reduced under thermodynamical considerations. Figure 39 shows the adapted Richardson Ellingham diagram in a temperature range between 500 – 2100 K highlighting potential indirect and direct reduction scopes applied to the specific metal oxides, identified in chapter 3.3.2 as well as for SiO_2. The black lines with positive and negative slope respectively, express the oxidation of carbon monoxide and solid carbon with one mole oxygen. Hence, it can be accentuated that indirect reduction is negligible for the reduction experiment excepting for Mn_3O_4 and Fe_3O_4. However, direct reduction is the prevailing process for metal formation. The red dashed line marks the maximum experimental operation temperature.

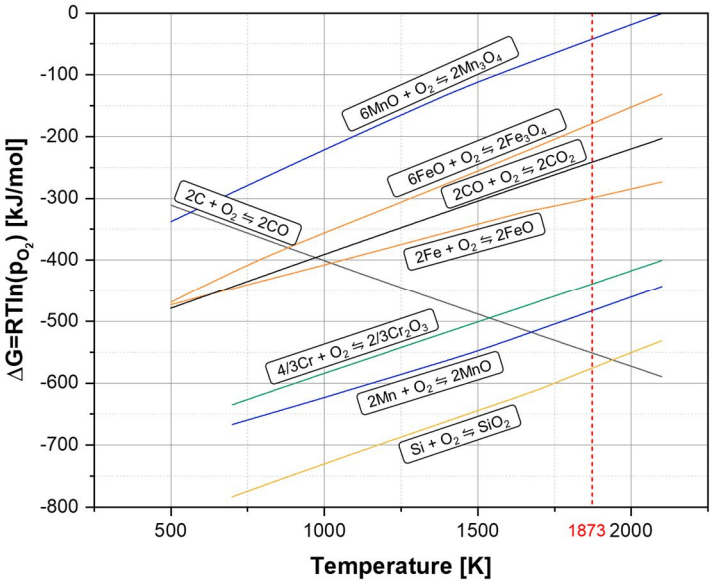

Figure 39: Richardson Ellingham diagram: Oxidation of relevant metals, metal oxides and Si between 500 – 2100 K, data from HSC Chemistry 7.1 [83]

The same is done for P-containing components, which can be seen in Figure 40. Among these are gaseous and solid P_2O_5 and C_3P. Indirect reduction until 1500 K seems to be only possible for gaseous P_2O_5, but can be neglected because this compound is thermodynamically stable at temperatures even greater than 1650 K ($P_2O_5 \leftrightharpoons \{P_2O_5\}$). [83] Furthermore, it is stated, that C_3P is also stable enough even at higher temperatures, and therefore it is assumed that the decomposition to $\{P_2O_5\}$ does not occur in the observed temperature range.

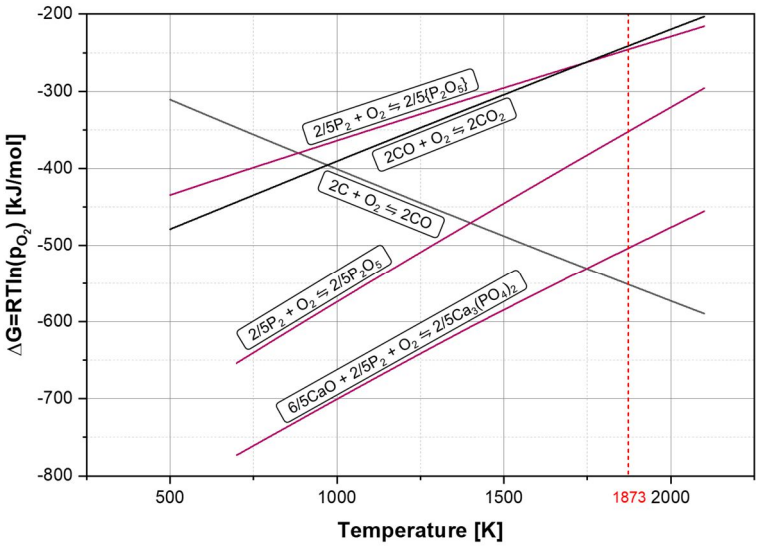

Figure 40: Richardson Ellingham diagram: Oxidation of relevant phosphorus species between 500 – 2100 K, data from HSC Chemistry 7.1 [83]

The heating-up process is relevant to protect the crucibles for destruction on one hand and on the other hand to ensure enough time by exposing the samples to a suitable temperature range. If it is too fast, crucible-material can be damaged due to thermal stress and to low heat rates would only unnecessarily delay the already long-lasting process. For this reason, a heating rate (HR) of 300 K/h was selected for both experiments until 1873 K were reached. The holding time at the maximum temperature was chosen to be 30 min for the smelting step and 45 min for reduction. Since the entire process is executed, the samples were cooled down within the furnace chamber with a HR of 300 K/h. As the last part of this chapter, phosphide formation needs to be examined in a greater detail. The scope includes phosphides of iron, chromium, and manganese regarding chemical and thermodynamic aspects.

3.3.4 Expected metal phosphides based on the gained knowledge

In the last sub-chapter phosphide formation based on the six samples to be treated in the reduction experiment are discussed in more detail. Thermodynamic considerations along with deliberations according to the composition, particularly the relation between metal and phosphorus content convey an overview of the possible appearance of potential phosphides under the applied process conditions.

First of all the relationship between substance amount of Fe, Cr, or Mn and P_2 denoted as stochiometric ratio is calculated, using the values of Table 6 and are presented in Table 7.

Table 7: Stochiometric ratio (mole Me/mole P_2) of the synthetic slag samples (calculated composition)

Fe-slags		**Cr-slags**		**Mn-slags**	
S1-Fe_{low}	**S4-Fe_{high}**	**S2-Cr_{low}**	**S5-Cr_{high}**	**S3-Mn_{low}**	**S6-Mn_{high}**
7.2	29.0	7.2	29.2	7.3	28.9

The Me/P_2 ratio of higher concentrated metal slags (S4, S5, and S6) is around quadruple compared to slags with lower metal content. The greater the value the stronger the probability that gasified phosphorus get in contact with the molten metal bath, which in turn promotes the phosphide formation mechanism. In terms of SR related to phosphide species named in chapter 2.7.1, metal amount is abundant even for lower metal containing slag samples (S1, S2, and S3), which means that the formation of all illustrated phosphides is inherently feasible. Thermodynamic aspects including ΔG of phosphide compounds are already considered in chapter 2.7.1 at the maximum operation temperature of the InduMelt plant (1900 K), which is a comparable temperature level to the conducted experiments in this thesis (1873 K). However, it must be accentuated, that all slag samples run through a wide temperature range

during reduction experiment, and it was already identified, that P_2 can potentially exist at lower temperatures (1473 K). However, gaseous phosphorus by C_3P reduction takes place at even higher temperatures of 1750 K according to the Richardson Ellingham diagram. While at 1900 K only FeP_2 formation can be excluded for examined metal phosphides by regarding the Gibb's energy, temperature dependency at lower temperature ranges is investigated later. An overview of reaction pathways between phosphorus and iron, chromium, and manganese is summarized in Figure 41.

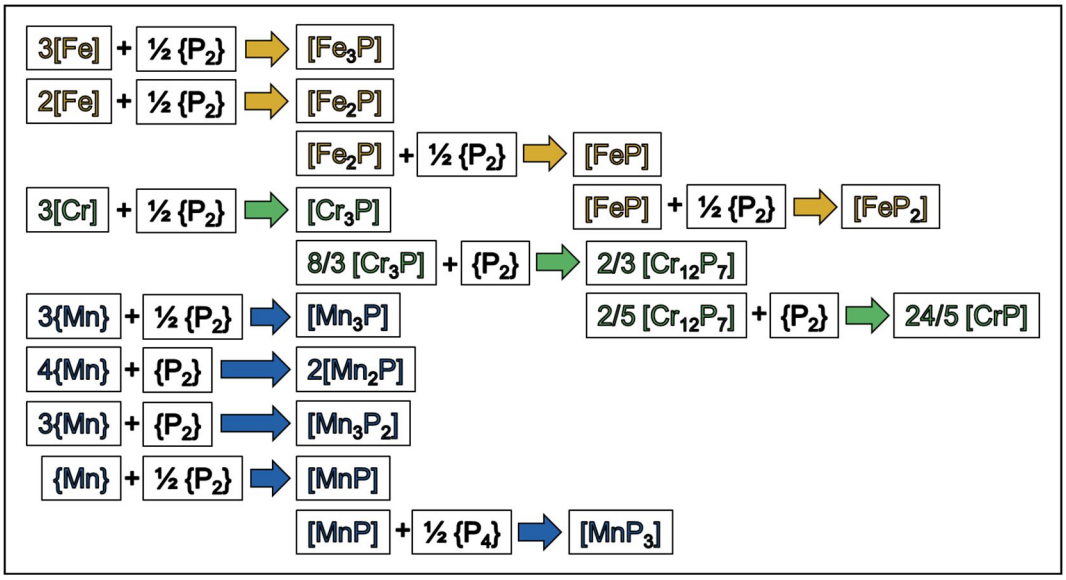

Figure 41: Summary of Fe-, Cr-, and Mn-phosphide reaction sequence, own representation from [59]

Schlesinger et al. (2002) shows a variety of thermodynamic data, including the development of the Gibb's energy for a wide range of metal phosphides depending on the temperature. This embraces phosphide species, relevant for this thesis and is presented in Figure 42. Therefrom, it can be deduced that higher temperatures increase the driving force (ΔG becomes more positive) of phosphide origination and this tendency is followed by all depicted phosphides. All values of the Gibb's energy correlates to chemical reactions in Figure 41, while silicon and calcium phosphide formation reactions are expressed in Equation 3-27 and 3-28. During reduction experiment execution, samples pass through the entire temperature range, beginning at room temperature and expire at the maximum of 1873 K. By surpassing 1473 K P_2 is stable under thermodynamic considerations. The scope where gaseous phosphorus potentially proceeds is outlined in the area between both red dotted dashed lines according to Figure 42. Thus, with exception of SiP all phosphides tend to be formed in this temperature range. [59,61]

$$[Si] + \frac{1}{4}P_4(g) \leftrightarrows [SiP] \qquad \textbf{3-27}$$

$$(Ca_3(PO_4)_2) + 8C \leftrightarrows [Ca_3P_2] + 8\{CO\} \qquad \textbf{3-28}$$

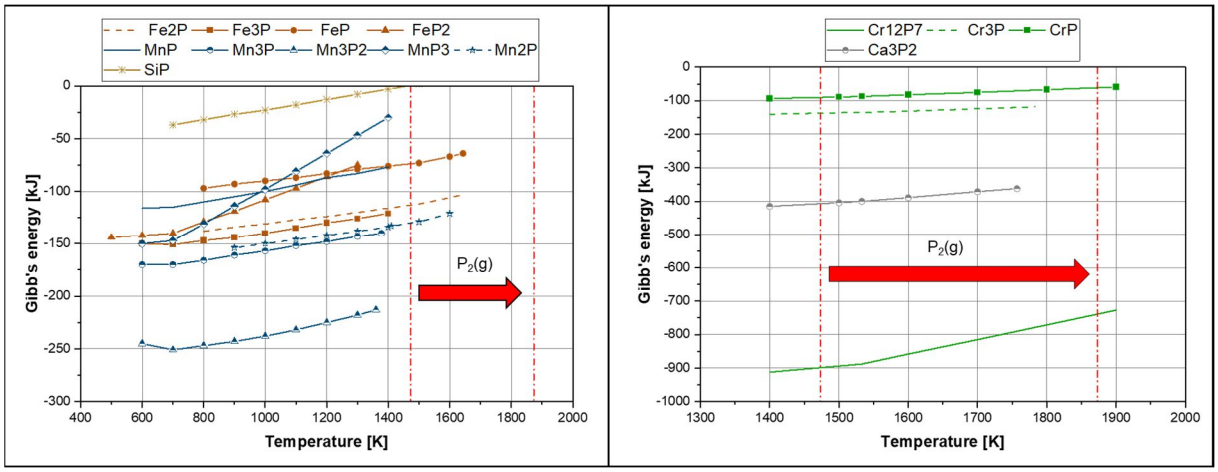

Figure 42: Gibb's energy vs. temperature of relevant Fe-, Cr-, Mn-, Si-, and Ca-phosphides, cf. [61]

Due to sufficient metal quantities in both, low- and high-metal-concentrated slag samples excepting SiP, all phosphides can potentially be formed. Phosphide reactions with lower SR-value compared to SR of slag sample composition ($SR_{reaction} < SR_{sample}$) lead to an increase of the Me/P_2-ratio of the mixture (concentration of the metal content) and vice versa. In the case of chromium, it cannot be assessed if after the formation of C_3P enough gaseous phosphorus remains for the origination of $Cr_{12}P_7$. For manganese phosphide formation, the metal needs to be in a gaseous state, which seems very unlikely. By additionally examining the driving force of each reaction it is expected that Fe_2P, $Cr_{12}P_7$, and Mn_3P_2 are the favoured phosphorus-species in the formed metal alloy. However, as already stated reaction kinetics and influence of interdependencies between different slag constituents are ignored in these considerations.

3.4 Experimental execution

The sequence of the experimental execution comprises of a first preparation of six slag samples in a previous smelting step, investigating their melting behaviour after reductant addition in a heating microscope, and the subsequent carbo-thermal reduction. Smelting was carried out in an EF; reduction take place thankfully in an electrically heated furnace at the

Chair of Nonferrous Metallurgy at the same equal temperature curve according to chapter 3.3.3.

3.4.1 Smelting experiment

MgO-crucibles filled with samples were placed on the respective position on the refractory-concrete-base, which is positioned on the bottom panel of the EF. The heating curve was adjusted in iTools (HR = 300 K/h until 1873 K with a hold-up time of 30 min and a cooling-down rate of again 300 K/h) and transferred to the advanced temperature controller and programmer. Finally, after starting the heating process the measurement in SignalExpress starts to run, recording temperature values from the type S TC. Ar-gas was not necessary for sample smelting and therefore it was waived for this step, but the exhaust ventilation was on. After experiment execution, solidified slag is gained using chisel and hammer. Then coarse lumpy slag was crushed in a jaw crusher with a target grain size of 0.5 mm. Ultimately, 15 g for each sample were used for reduction. Moreover, roughly 4 g were handed to the ICP-OES analyses, which is also the basis for the results in 4.1.1. Before reduction is carried out, the melting behaviour of the slag-carbon mixture is investigated in a heating microscope.

3.4.2 Slag-reductant melting behaviour

To ensure that the slag-carbon mixtures also become molten, preliminary tests were carried out in a HM. Crushed powder of the slag-reductant samples was shaped by means of a press stamp. Hence, fine grained and powdery material was elutriated using acetone to facilitate the pressing procedure. With its high vapor pressure and low boiling temperature of 329 K acetone has no impact on the treated mixture. [94] The formed press cylinder was applied to a plate of Al_2O_3, which was then placed on a TC and pushed thoroughly into the furnace chamber. A volume flow rate of 2 l/min argon gas was adjusted, and the furnace chamber was cooled with tap water. Then the light source was switched on and the heating process was started on the measuring computer. The sample within the reactor chamber is heated until 1873 K were reached and cooled down afterwards. One heating-up and cooling-down cycle takes around two hours – faster heating rates are chosen for this experimental setup in comparison to the smelting and reduction step.

3.4.3 Reduction experiment

Due to unreliable heating rates of the EF, fortunately a different electrically heated furnace was provided by the Chair of Nonferrous Metallurgy. Slag with solid carbon amount were transferred into the MgO-crucibles. Graphite plates for crucible underlayment with 10 mm thickness ensures radiation input in the section of sample material, which is at the crucibles bottom. For experiments in the EF, it was first designated to put a cap made of graphite with a central hole of 8 mm for gas removal on the top of the crucible. This measure should ensure a CO atmosphere within the crucible, but the cap was omitted owing to the circumstance that the furnace used for reduction is equipped with a flap, which closes the furnace chamber after 1173 K. However, Ar gas purged the furnace over the entire duration of the experiment. The refractory-concrete-base with the MgO-crucibles according to the setup shown in Figure 32 is placed centrally into the furnace chamber. The same HR and cooling down process as for smelting was chosen for reduction experiment with a hold-up time of 45 min. Temperature monitoring via a type S TC was omitted. Instead, an Ar volume flow rate of 4 l/min was set at the flow meter. After reduction execution the head of cooled MgO-crucibles were cut with a diamond saw blade and the crucibles bottom plate was halved. Since little material was available, crucibles were broken with a jaw vice, hammer, and chisel. As far as possible the gained material was separated into a metal-, and mineral-phase. Finally, the prepared material was analysed for their elemental composition with ICP-OES. Moreover, to identify oxidic- and metallic-phases a SEM-analysis was carried out subsequently.

4 Results and discussion

Results of the total experimental sequence are presented in the up-coming chapter. First, results of the smelting step from ICP-OES are introduced and discussed, whereby calculated values are confronted with practical outcomes, arguing about identified deviations. Then, outcomes of the heating microscope which are debated shortly are presented afterwards, followed by those of carbo-thermal reduction. ICP-OES analysis of treated material from the reduction step is supported by scanning electron microscopy (SEM). Findings from the smelting step imply only synthetical slag analysis, while the reduction experiment includes investigations of both potential emerging phases: a slag-phase, which, due to the risk of confusion, will be referred as follows as mineral phase (MI) and a metal-phase (ME). As already stated, the gas phase is not subject of investigations in this thesis and is therefore not regarded. The subsequent reduction experiment is discussed at the end, whereas achieving results are compared to assumptions made at the beginning of this thesis. Therefrom, statements made from the literature research can be corroborated or refuted.

4.1.1 Smelting experiment

All six mixtures were treated simultaneously in a smelting experiment up to 1873 K. Heating process occurs according to the adjusted programme, which can be assured by the redundant additional temperature measurement with the type S TC. ICP-OES results from the slag samples (S1 – S6) are shown in Figure 43. Excepting S2, which Cr-quantity of 1.6 m.-% is too low, metal content for all remaining samples is in a very good agreement with pre-calculated values from Table 6. 0.4 – 0.5 m.-% phosphorus in each sample as well as the amount of Mg is also in a good accordance with the beforehand conducted calculation. Al content instead is

widely fluctuating in a range between 3.2 – 12.2 m.-%, which cannot be explained to this extent. The occurring deviations could be attributed to a wrong slag sample generation, i.e., error in weighing, or sample extraction, or aluminium input from other sources e.g., abrasion from tools, jaw crusher etc. However, as described later the crucible shows nearly no attack by the smelted slag samples. In addition, the crucible material composed of 97.5% MgO, whereby all slags are not concentrated with Mg. Therefore, a concentration of Al owing to the crucible can be excluded.

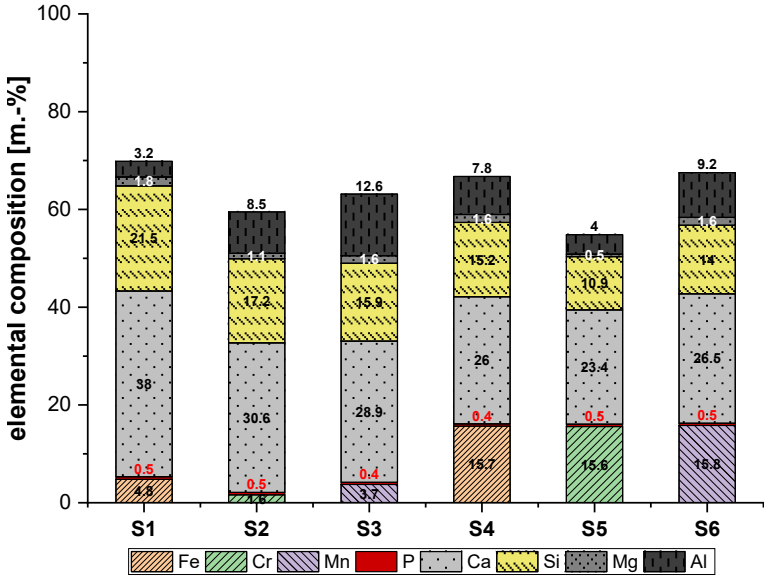

Figure 43: ICP-OES results from synthetic produced slag samples after smelting, illustrated as elemental composition

In Figure 44 the oxidic composition of samples S1 – S6 are depicted. Because oxygen content cannot be determined with ICP-OES, it was assumed, that all measured elements from Figure 43 are incorporated into a slag phase as the respective oxides. For this reason, the total mass percentage doesn't match with 100%, but is in a reasonable range.

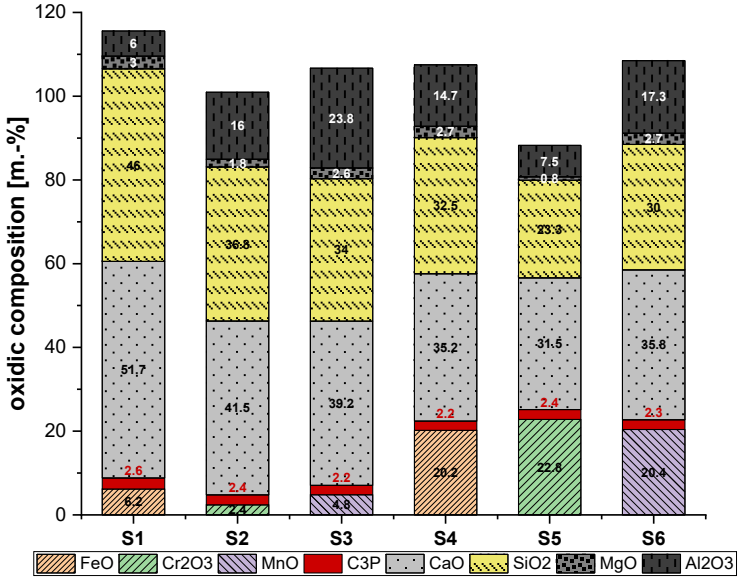

Figure 44: Calculated oxidic composition based on the elemental ICP-OES results of Figure 43

The course of action for sample extraction after smelting and reduction experiment and subsequent sample processing is depicted in Figure 45.

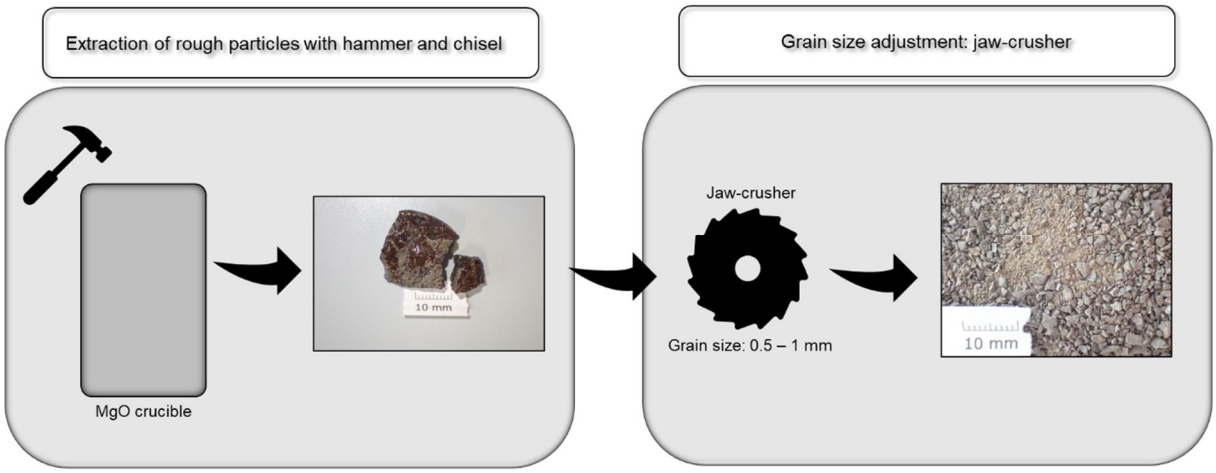

Figure 45: Simplified flowchart of sample extraction after smelting and reduction experiment

Slag samples after destruction of MgO-crucibles with the aid of hammer and chisel can be seen in Figure 46. Despite S1 – S4 and S6 showing a uniform formation of solidified slag, S5 (high chromium slag) exhibits a characteristic hump. Thus, for this sample melting process could not take place completely, which can be attributed to an inadequate melting time, or the chosen temperature range was too low. However, for samples S1 – S3 sintering processes can't be excluded. A first optical view of the broken MgO-crucibles reveals that there is a

precise and consistent boundary between slag and crucible material. Little to hardly diffusion of slag material into the crucible and vice versa is perceptible and results of Figure 43 confirm that slags are not concentrated with Mg content.

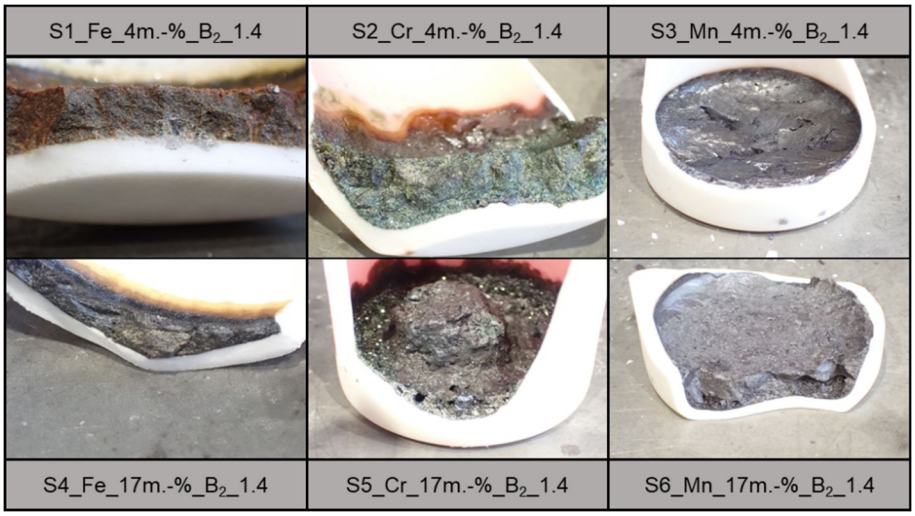

Figure 46: Broken MgO-crucible with solidified slag content (S1 – S6) after smelting experiment

Extracted coarse slag pieces from the crucible with around 10 mm size for each slag sample (S1 – S6) is illustrated in Figure 47. A smooth and plain surface of broken slag particles with a distinctive colour for each sample is recognizable, which is light and dark brown for iron samples, green for chromium slags, and black for manganese containing material.

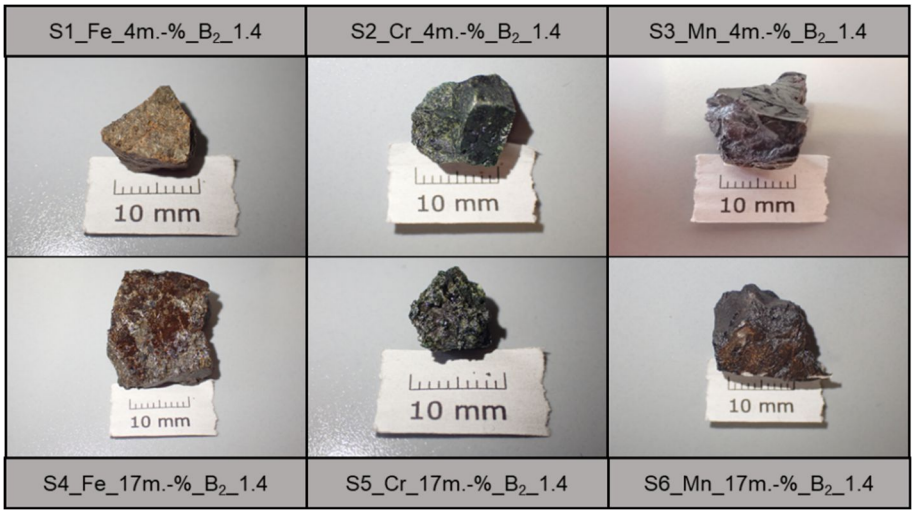

Figure 47: Pieces of synthetically produced slag samples (S1 – S6) obtained from the MgO-crucible after smelting experiment

Crushed slag samples (S1 – S6) with a grain size around 0.5 mm after treating slag chunks in a jaw crusher is shown in Figure 48.

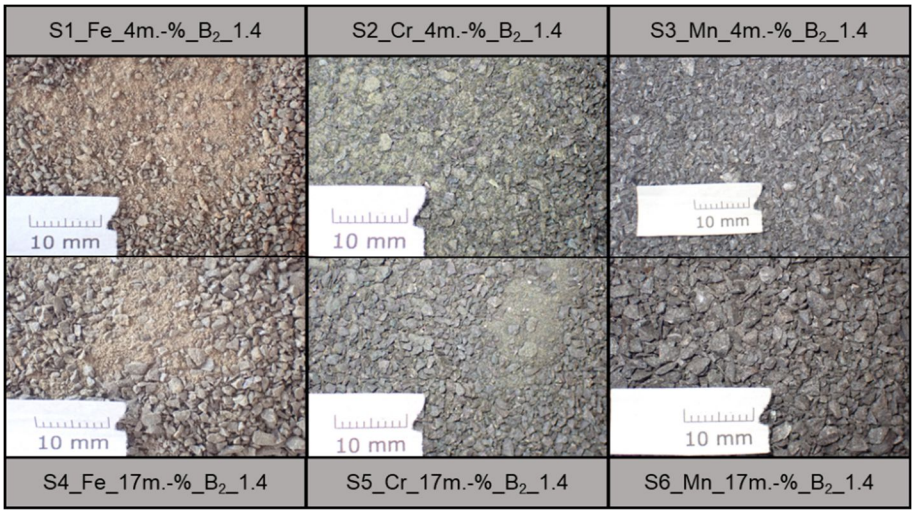

Figure 48: With a jaw crusher treated (grain size: ~0.5 mm) synthetically produced slag samples (S1 – S6) after smelting experiment

The basicity of the slag samples is calculated based on the oxidic composition results from Figure 44 and is summarized in Table 8. Assumptions made are that Ca-, and Si-content is present as CaO and SiO_2 species, and Ca amount bound in C_3P is subtracted from the total Ca amount. The basicity of the samples is 1.1 for S1 and S4, 1.2 for S2, S3, and S6 and 1.4 for S5.

Table 8: Calculated basicity of slags after smelting experiment based on the results from Figure 44

S1	S2	S3	S4	S5	S6
1.1	1.2	1.2	1.1	1.4	1.2

While it was first assumed, that the oxygen content in the samples adds up to 100%, this presumption corresponds well with calculated values within the accuracy limits of the ICP-OES analysis, which is depicted in Table 9. Species presumed for calculations were FeO, Cr_2O_3, MnO, C_3P, CaO, SiO_2, MgO, and Al_2O_3.

Table 9: Calculated total mass percentage m.-% [%] of samples S1 – S6 after smelting experiment based on the ICP-OES results according to Figure 44

S1	S2	S3	S4	S5	S6
115	101	106	107	88	108

Excepting S5 (Δm.-% = -12 m.-%) all calculated values for the remaining samples shows higher total mass percentages (Δm.-% = +1 m.-% – +15 m.-%). It is quite conceivable that phase formations under oxygen release/inclusion occurred during the melting process and for the resulting slag samples different compounds are formed and bounded into different slag phases than the assumed occurrence of simple oxide species considered above.

4.1.2 Slag-reductant melting behaviour

This experiment serves as an intermediate step for the upcoming reduction experiment in order to evaluate the melting behaviour for each mixture. All slag-carbon samples were reduced separately at 1873 K with the same heating-up process in the electrically heated reactor of the HM. Around 0.1 g from the same material which will be reduced later in the crucibles was used for these investigations.

Treated samples are presented in Figure 49. The used material stem from samples S1 – S6 after smelting experiment after carbon addition. Basically, every sample could be converted to a molten state before the maximum reduction temperature of 1873 K were reached. Figure 49 shows that low iron containing slag S1 has covered the whole area of the Al_2O_3 plate implying a good flowability. Pores are recognizable as well which could come from the formed gaseous compounds as a reaction product of reduction. However, the mixture has brown not identifiable spots, and no metallic inclusions or spheres can be identified. Regarding S4 even metallic spheres are originated, embedding in the surrounding slag. A segregation of the reduced iron and slag is highly developed. Low chromium sample S2, reduced in the HM reveals small partly reduced metal nuggets in the centre, which are surrounded by slag. Green colour is always an indication for chromium-oxide and in turn a result of an incomplete reduction. The dark green colour of the reduced sample S5 with high Cr-amount seems to be compact, highly viscous, and homogenous. No metal can be perceived and no clear distinction between slag and metal can be made as it is for S2. For both Mn-bearing samples it seems that they consist primarily of slag. Solely small traces of metal are perceptible by S6. Manganese evaporation is also stated in literature taking place at temperatures higher than 1873 K. [95]

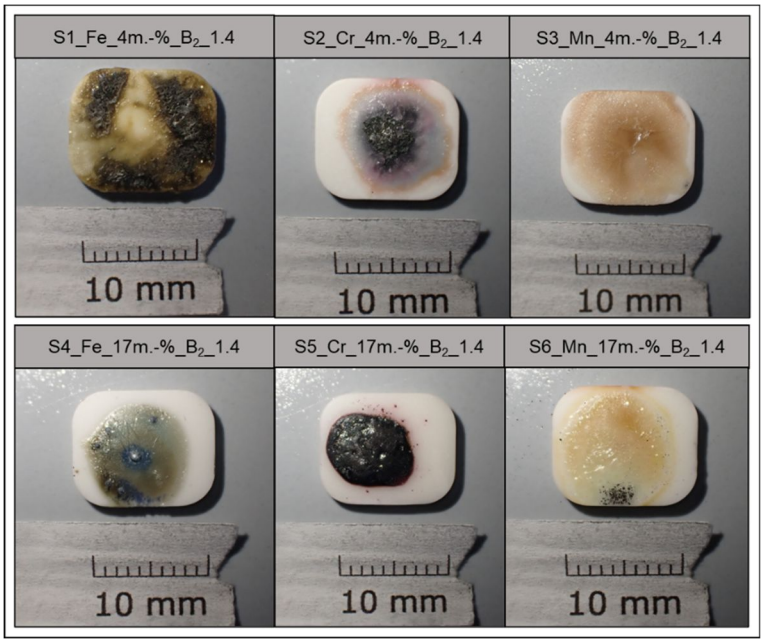

Figure 49: Slag samples (S1 – S6) after reductant addition on the Al_2O_3-plate after treatment in a heating microscope at 1873 K

Image recording during the HM experiment execution at characteristic temperatures of low metal concentrated slag-carbon mixtures can be seen in Figure 50.

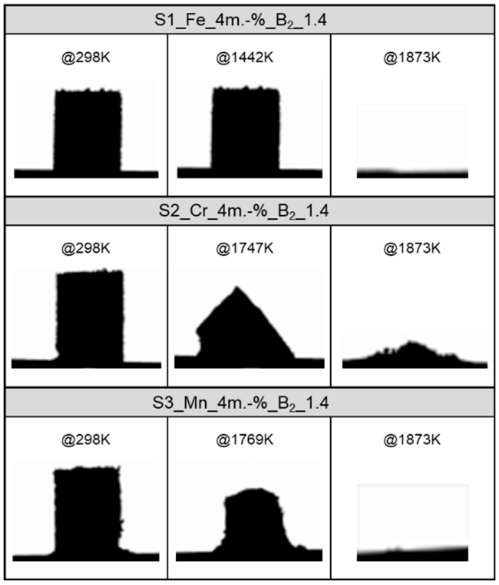

Figure 50: Silhouette of slag-carbon mixtures with low metal concentration (S1 – S3) during HM-experiment execution at start-, softening-, and final-temperature

Images from the HM-experiment treating the high metal concentrated slag-carbon mixtures is illustrated in Figure 51.

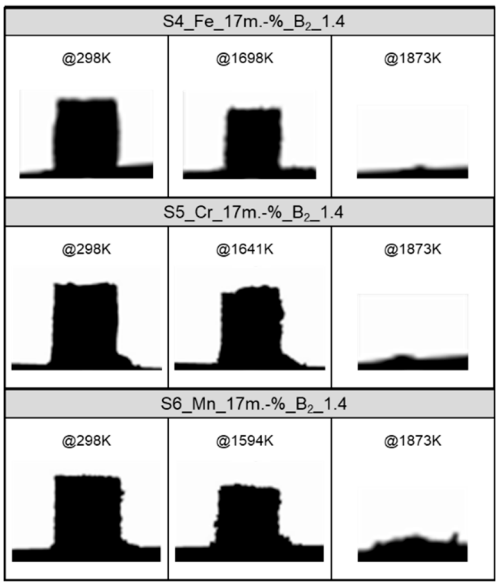

Figure 51: Silhouette of slag-carbon mixtures with high metal concentration (S4 – S6) during HM-experiment execution at start-, softening-, and final-temperature

The relative area [%] is the ratio between the current silhouette area of the respective temperature ($A_{T_{current}}$) and the initial surface of the cylinder at experiment start ($A_{initial}$) which is presented in Equation 4-1.

$$rel.area = \frac{A_{T_{current}}}{A_{initial}} \cdot 100\% \qquad \textbf{4-1}$$

The relative area of low metal concentrated slag-reductant mixtures is determined for temperature values up to 1873 K in Figure 52.

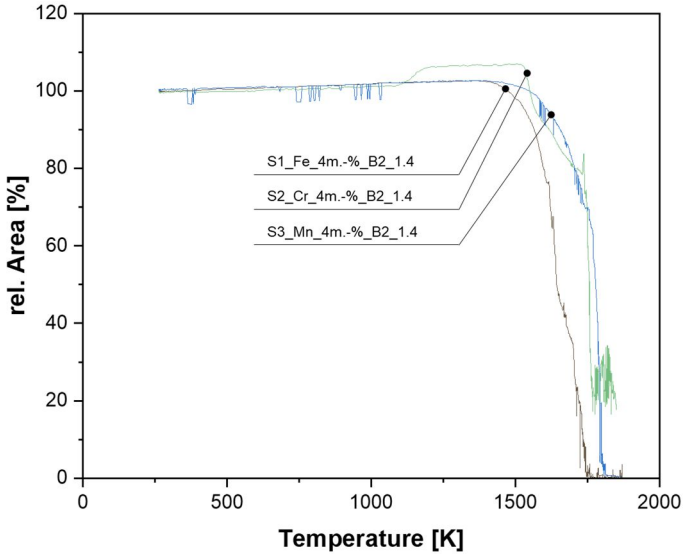

Figure 52: Relative area change after treating the low metal concentrated slag-carbon mixture (S1 – S3) in the HM

The change of the rel. area over temperatures to 1873 K for high metal concentrated slag-reductant samples is shown in Figure 53.

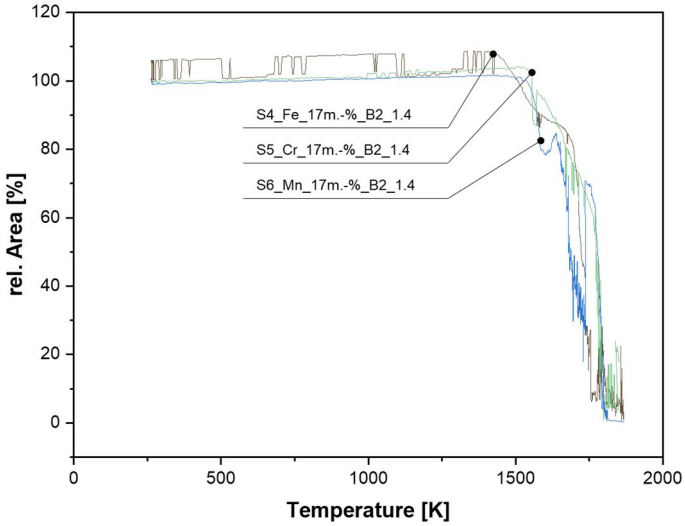

Figure 53: Relative area change after treating the high metal concentrated slag-carbon mixture (S4 – S6) in the HM

To summarize Figure 50 – Figure 53, it can be concluded that all slag-carbon mixtures become molten before the maximum process temperature of 1873 K for the upcoming reduction experiment will be reached. As a result, all mixtures can be used unproblematically for the final step of carbo-thermal slag treatment.

4.1.3 Reduction experiment

This chapter illustrates results and their discussion from the reduction experiment. The heating-up and cooling-down process has complied with the set specifications. The maximum temperature of 1873 K was kept constant for 45 min, heated up and cooled down with a rate of 300 K/h. A clap has closed the furnace chamber at 1173 K, without interrupting argon gas purging with a constant volume flow rate of 4 l/min. First sampling and preparation of the treated material for subsequent analysis is described, followed by the applied analysis methods of ICP-OES for elemental composition and SEM for the identification of oxidic- and metallic-phases within the obtained material. In the following, as already described, the terms mineral-phase and metal-phase are used for the resulting products of carbo-thermal reduction. The comparison of appearing anomalies or deviations between the assumptions made at the beginning of this thesis and results are discussed in the conclusion of chapter 5. Furthermore, improvement suggestions for further experiments in the field of carbo-thermal reduction of iron-, chromium-, and manganese rich slags with focus on phosphide formation is also given but will be explained in more detail in chapter 6.

4.1.3.1 Sample extraction and preparation

After experiment execution, the head of the cooled crucibles was cut off with a diamond saw, and the bottom of the crucible was cut in half. The small amount of sample prevented that the crucible bottom could be cut as well, which would made sample extraction quite easier. Solidified material after carbo-thermal reduction at 1873 K inside the sawed crucible are shown in Figure 54. A clear separation of all low metal slags (S1 – S3) and crucible is identifiable. As distinguished from samples S4 – S6, where the crucible material is obviously interacting with the samples during carbo-thermal treatment. From sample S4, material has selectively eaten its way through the crucible bottom, resulting that nearly the entire sample amount was lost. Only little literature could be found, arguing the wear of MgO-crucibles by molten slags or iron at elevated temperatures. It was stated, that the oxygen amount in molten iron has a great influence on the interaction-behaviour to the MgO-crucible wall, intensifying the attack at higher oxygen concentrations. [96] S5, instead, shows massive cavities, in which metallic spheres of chromium could be isolated manually. The red discolouration of the crucible material, which could also be observed at the predecessor smelting step, is an indication of ongoing chemical reactions between chromium and MgO. However, in comparison to S4 and S6 the crucible wear of the chromium containing sample is significantly lower. The crucible of S6 is showing the largest deformations. Its bottom is strongly curved, and the interference of material and

crucible shows, that treated slag constituents are diffused into the crucible. However, crucible material was not analysed, but it can be concluded, that primarily for higher concentrated iron, chromium, and manganese samples the choice of crucible material is essential and should be discussed in coming experiments. Particularly for S6, diffusion of slag constituents into the crucible is highly developed.

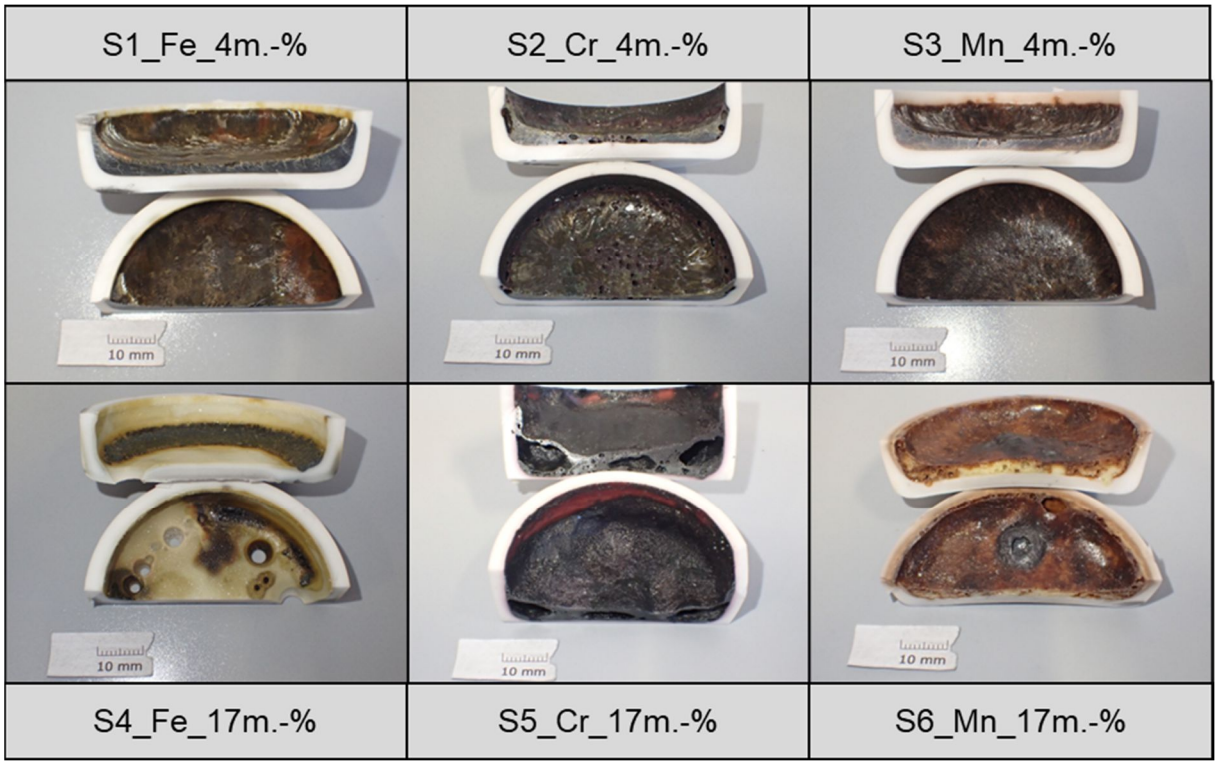

Figure 54: Slag samples (S1 – S6) inside the cut MgO-crucibles after carbo-thermal treatment at 1873 K

As it can be seen, only a thin layer of material is left in the crucible after the reduction experiment. According to Figure 33, representing the calculated amount of slag obtained after smelting and before reductant addition the total sample mass theoretically should be around 29 g of low metal slags and approximately 31 g for high metal slags. However, after carbo-thermal treatment only between 9.5 – 12 g of material could be recovered. The remaining amount can be mainly attributed to mass losses from extraction and oxygen removal due to reduction processes. This loss of mass along the entire experimental chain needs to be considered for further experiments.

Pieces of treated material, obtained by a jaw vice, hammer and chisel of low concentrated metal samples (S1 – S3) can be seen in Figure 55. Especially for S1 and S3 layers with different colours are recognizable, whereas S2 seems to be uniform along the entire height.

Here, this need to be considered particularly guaranteeing sampling quality in order to make reliable statements about the material composition. However, no metal droplets could be separated. For this reason, an elemental analysis as well as a SEM were performed to determine, whether reduction processes have taken place at all. At this point of the thesis, sample designation for material whose more precise composition of the phases is not known, are denoted as MI+ME.

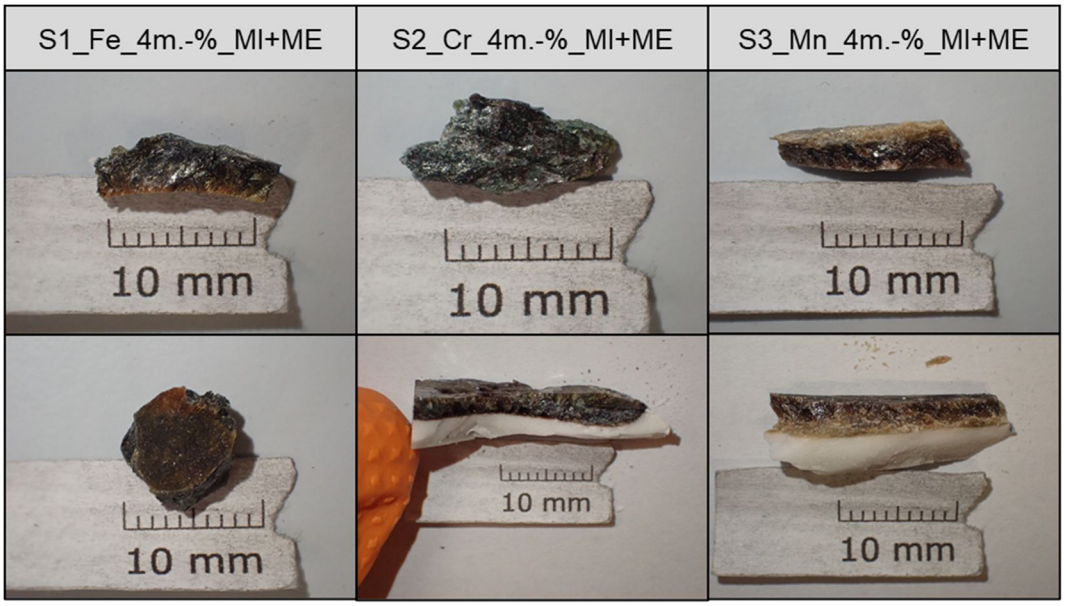

Figure 55: Pieces of extracted material, after carbo-thermal treatment of samples S1 – S3 (MI – mineral phase, ME – metal phase)

Pieces of treated material, obtained by a jaw vice, hammer and chisel of high concentrated metal samples (S4 – S6) are illustrated in Figure 56. Almost the entire material amount from sample S4 with 17 m.-% iron gone through the bottom of the crucible, whereby magnetic material has been deposited on the graphite underlayment. Therefore, this is the only material for further analysis of sample S4. Metal spheres could only be separated manually from sample S5, which could be easily done by crushing. Metal droplets with a total mass of 0.19 g were mainly found within the big cavities, which can be seen in Figure 54. The colour of the remaining mineral phase of sample S5 is dark green, indicating high contents of oxidic unreduced chromium species. However, with the help of SEM-analysis the proportion between metallic- and oxidic-chromium within the mineral phase will be figured out in chapter 4.1.3.2. By contrast, the sample of 17 m.-% manganese is highly porous. Areas of different colours, ranging from yellow, to orange and brown to black imply a segregation of this treated material. Possibly, various phases of slags with different composition were formed. Furthermore, crucible material was severely attacked by sample S6.

Totally, between 9.5 – 12 g sample amount from S1 – S3, and S5 – S6 could be recovered from the crucibles. Concerning the magnetic material of S4, around 2.2 g were obtained from the graphite underlayment and only 0.19 g of chromium metal droplets could be gained.

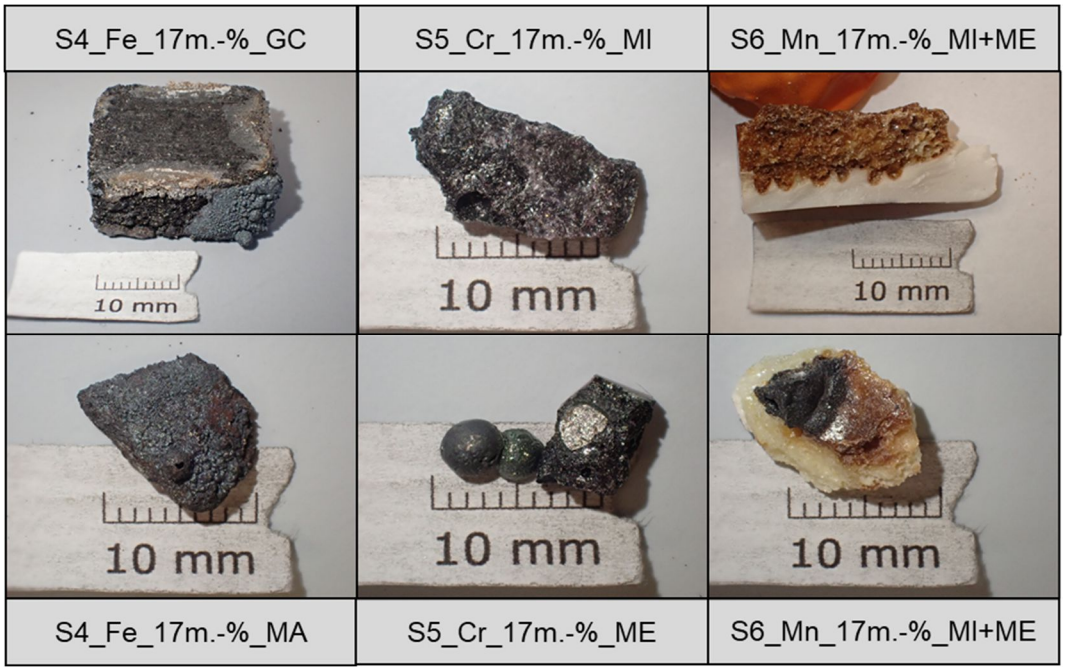

Figure 56: Pieces of extracted material, after carbo-thermal reduction of samples S4 – S6 (MI – mineral phase, ME – metal phase, GC – graphite cube, MA – magnetic phase)

In summary, due to missing visible metal droplets, no metal could be separated manually from samples S1 – S3 and S6. Only S5 enabled the separation into a metal- and a mineral-phase. For the sample S4, only magnetic material was gained from the crucible's graphite underlayment. Subsequently, the reason for no metal isolation needs to be identified, which will be supported by analysis methods of ICP-OES and SEM. Then, a distinction between metallic- and oxidic-phases can be made.

4.1.3.2 SEM-analysis

First, SEM-analysis consists of sample-preparation. For this purpose, all sample pieces to be analysed were embedded into a mould made of epoxy resin. In order to obtain a smooth surface, receiving clearer images, the sample is polished on the side to be examined. The samples to be analysed are the mineral phase from S1 – S3, and S6, the metal- and mineral-phase from S5 and the magnetic material obtained from the graphite underlayment of S4.

Representative for all three samples with lower metal amounts (S1 – S3) an image of the SEM-analysis of S2 is given, which can be seen in Figure 57. Characteristic spectra of Figure

57 were chosen and their elemental compositions are summarized in Table 10. Four slag phases of different compositions could be localised at this spot. Slag phase 2-1, 2-2, and 2-4 are rich of chromium but poor in calcium, silicon, and phosphorus. A conversely composition is shown for slag phase 2-3. Furthermore, while Mg is enriched in slag phase 2-4, Al is distributed in all slag phases with approximately 10 m.-%, but with slightly higher amounts in the calcium- and silicon-rich slag phase 2-3. Carbon amount must be interpreted cautiously, because of interferences due to the epoxy resin. However, no metallic droplets of chromium can be found, and this circumstance is also true for S1 (no metallic iron) and S3 (no metallic manganese). This is the reason why only sample S2 is considered in detail in place of low metal samples (S1 – S3). Possibly, the metal content for these samples was too low, that the probability of contact between carbon and metal-oxide was reduced. To low amount of metal could also inhibit the formation of metal droplets. Besides, the grain size of initial particles between 0.5 mm – 1 mm was potentially too small and that therefore the gas distribution was limited. But this fact was also valid for the high concentrated metal samples and chromium in turn could be reduced, which will be discussed below.

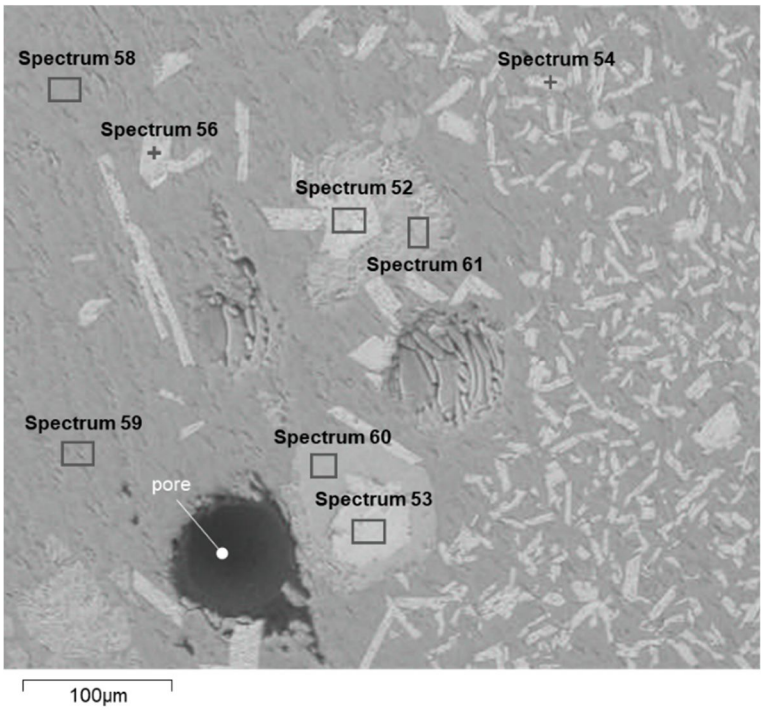

Figure 57: Image from the SEM-analysis of sample S2 after carbo-thermal reduction at 1873 K

Table 10: Elemental composition [m.-%] of characteristic spectra from the SEM-analysis of S2 according to Figure 57 after carbo-thermal reduction at 1873 K

	Spectrum – sample S2							
	52	**53**	**54**	**56**	**58**	**59**	**60**	**61**
Element	**Slag phase 2-1**		**Slag phase 2-2**		**Slag phase 2-3**		**Slag phase 2-4**	
C	4.5	5.2	4.9	4.6	5.6	5.9	5.7	5.4
O	37.3	36.9	37.3	38.5	40.0	39.8	39.7	40.4
Mg	1.0	0.9	0.5	0.4	0.6	0.7	8.0	8.3
Al	9.7	9.1	9.7	11.8	16.1	15.6	10.4	10.9
Si	2.8	2.3	3.1	3.4	10.7	10.7	2.7	2.6
P	0.1	-	0.1	0.1	0.5	0.5	0.1	-
Ca	5.6	4.6	6.8	6.8	24.4	24.9	5.4	5.2
Cr	39.1	41.0	37.7	34.4	2.0	2.1	27.9	27.3
total	100.0	100.0	100.0	100.0	100.0	100.0	100.0	100.0

Images from the SEM-analysis of the mineral phase of sample S5 is presented in Figure 58. Bright spots, indicating metallic chromium-droplets, can be detected sporadically with diameters of roughly <20 μm. This was also supported by analysis with a stereomicroscope. Therefore, around 4 g of sample were grinded and sieved (>200 μm, 200 – 100 μm, 100 – 40 μm and <40 μm). The sieve analysis of the smallest grain fraction reveals small chromium metal droplets of diameters as already mentioned of <20 μm. For this reason, a gravimetric separation due to density differences would be too costly for such a small amount of metallic chromium. Slag phases of different compositions are recognizable as well. The elemental composition of all spectra from the right-hand side of Figure 58 are summarised in Table 11. Low silicon, calcium and oxygen contents and high chromium amounts for spectrum 42/43 are a sign for metallic droplets. In addition, high phosphorus contents are a proof of formed phosphides and would be in a good agreement with the already stated affinity between metallic chromium and phosphorus. Overall, four slag phases are perceived, and their composition can be seen in Table 11. Very high amounts of aluminium are noticeable for all slag phases. Analogous results in comparison to SEM-analysis of sample S2 can also be validated for the mineral phase of S5: Higher chromium amounts in the slag phase 5-1 and 5-4 resulting in lower calcium and silicon amounts and vice versa for slag phase 5-2 and 5-3. Magnesium and phosphorus contents for all slag phases are low.

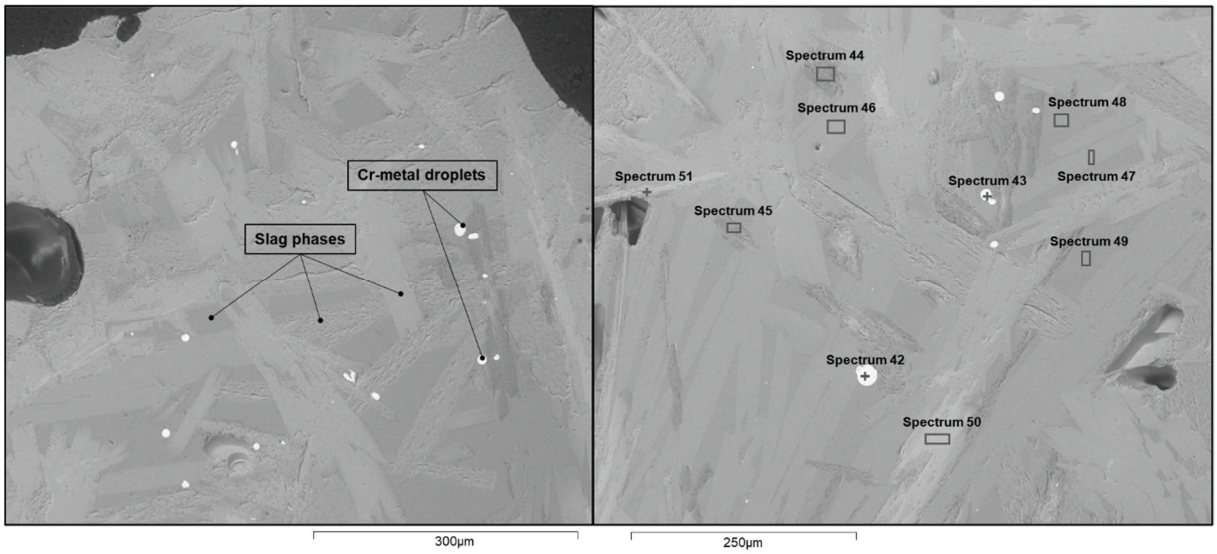

Figure 58: Image from the SEM-analysis of the samples S5 mineral phase after carbo-thermal reduction at 1873 K

Table 11: Elemental composition [m.-%] of characteristic spectra from the SEM-analysis of the mineral phase of S5 according to Figure 58 after carbo-thermal reduction at 1873 K

	Spectrum – mineral phase S5									
	42	**43**	**44**	**45**	**46**	**47**	**48**	**49**	**50**	**51**
Element	**Metal phase 5-1**		**Slag phase 5-1**		**Slag phase 5-2**		**Slag phase 5-3**		**Slag phase 5-4**	
C	6.7	6.5	5.0	4.4	4.2	5.3	5.3	6.2	4.6	3.4
O	10.8	11.9	43.2	42.9	39.7	39.4	41.5	41.3	39.6	40.0
Mg	0.6	0.2	-	0.3	0.3	0.3	0.6	0.6	0.3	0.3
Al	7.4	8.6	33.5	30.9	19.2	18.7	17.6	17.8	19.3	20.4
Si	2.5	2.8	3.3	4.0	8.9	9.1	13.3	12.8	2.1	2.6
P	16.5	16.2	-	0.1	-	-	0.5	0.5	-	-
Ca	5.4	5.6	6.0	6.7	24.8	24.4	17.9	17.7	4.0	5.4
Cr	48.1	46.9	9.0	10.7	2.9	2.8	3.3	3.1	30.1	27.9
total	98.0	98.7	100.0	100.0	100.0	100.0	100.0	100.0	100.0	100.0

For sample S6, after carbo-thermal treatment, the distribution of relevant occurring elements is depicted in Figure 59. A different colour for each element is defined, whereas brighter areas are characteristic for higher concentrations. Less Mg amounts were measured for this piece of sample and therefore Mg is omitted in this figure. The error-prone measurement of carbon, owing to influences from the surrounding epoxy resin is the reason why it is also not depicted in Figure 59. Brighter areas on the upper side on the bigger picture in grey on the left matches

with phases of higher manganese and phosphorus amounts and in turn lower calcium and silicon contents. Oxygen and aluminium are evenly distributed. Black circles are pores.

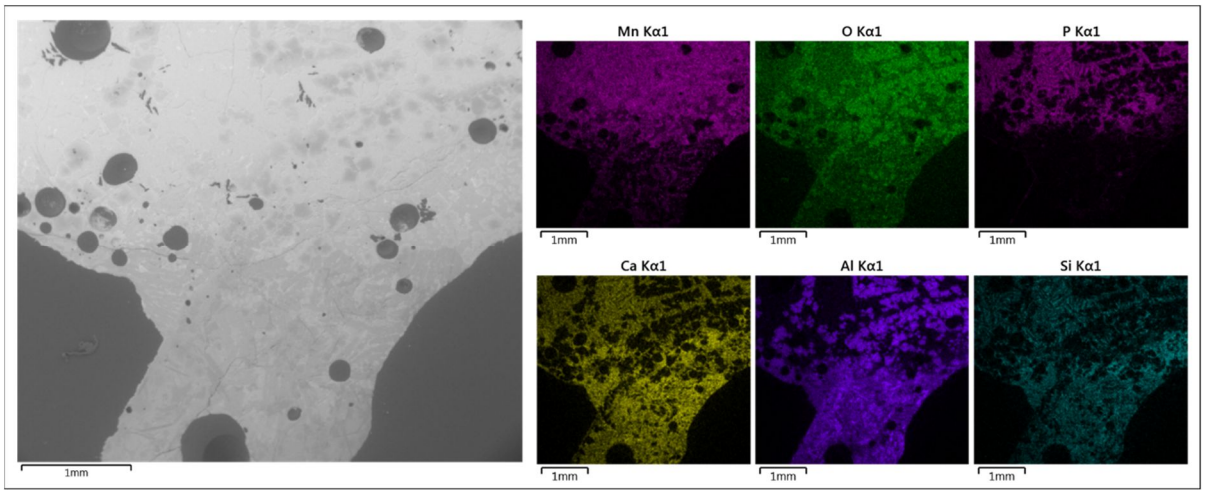

Figure 59: SEM-analysis of S6 – Elemental distribution of crucial elements such as Mn, O, P, Ca, Al, and Si

Moreover, to support the results of Figure 59 images from SEM-analysis from the sample S6 is shown in Figure 60. Two different slag phases could be identified on this image. No metallic droplets as for S1 – S3 were found during analysis. The elemental composition of the spectra, chosen on the right-hand side of Figure 60 are expressed in Table 12. A spot for spectra analysation was chosen on the upper part of the analysed grain, which is the reason for higher manganese amounts in both slag phases. The lower the manganese content, the higher the calcium and silicon amount. Furthermore, higher phosphorus contents are bound into the lower manganese slag phase. However, accordingly to Figure 56, dark spots representing the lighter manganese rich slag phase and a second heavier yellow to orange coloured nearly manganese free, calcium- and silicon-rich slag phase.

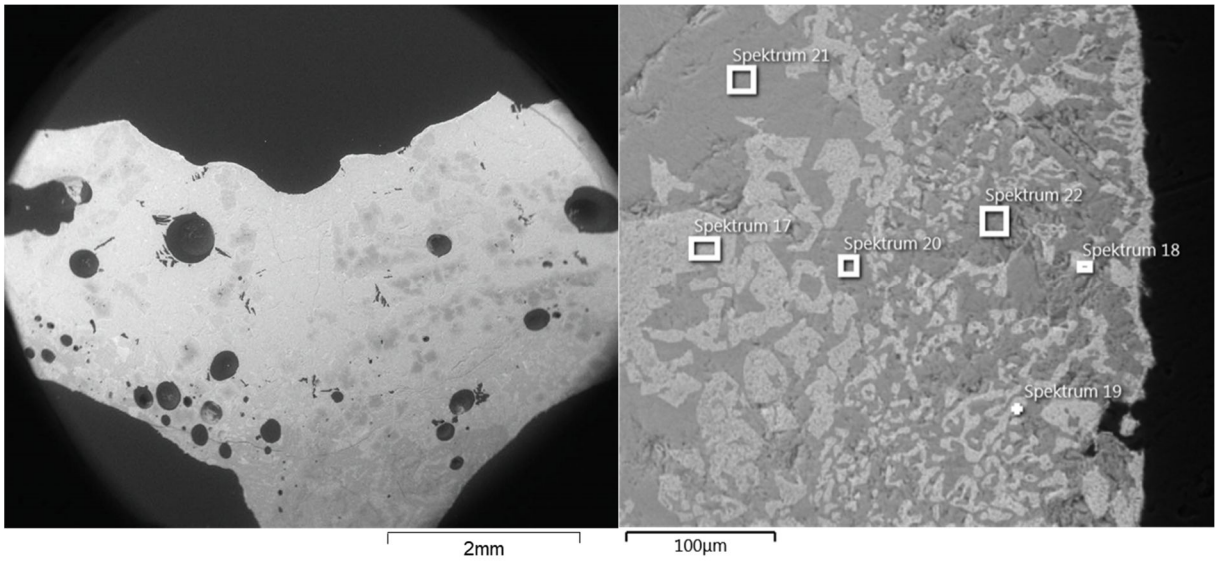

Figure 60: Image from the SEM-analysis of the sample S6 after carbo-thermal treatment at 1873 K

Table 12: Elemental composition [m.-%] of characteristic spectra from SEM-analysis of sample S6 according to Figure 60 after carbo-thermal reduction at 1873 K

	Spectrum					
	17	**18**	**19**	**20**	**21**	**22**
Element	**Slag phase 6-1**			**Slag phase 6-2**		
C	12.6	18.7	15.7	16.0	16.8	20.0
O	31.3	30.7	30.0	33.0	33.7	32.6
Al	7.3	1.6	2.5	0.8	1.3	0.8
Si	0.9	0.6	0.9	0.9	3.8	1.9
P	2.2	2.3	2.2	12.5	9.6	11.1
Ca	1.9	2.7	2.5	12.9	8.8	12.6
Mn	43.7	43.5	46.2	23.9	25.9	21.1
total	100.0	100.0	100.0	100.0	100.0	100.0

Figure 61 shows an image from SEM-analysis of magnetic material recovered from the graphite piece. Two different phases are perceptible, which can be supported by the elemental composition of spectrum 73 – 76 in Table 13: A magnetic- and carbon-phase. The former, is rich of iron, carbon, and oxygen, indicating an incomplete reduction. Therefore, beside metallic iron, the presence of magnetic unreduced Fe_3O_4 is quite conceivable and more probable than the occurrence of unmagnetic FeO. The existence of magnetic Fe_2O_3 owing to a missing oxidizing atmosphere could be excluded. Spectrum 75 and 76 consists almost exclusively of carbon and minor amounts of iron. However, it needs to be considered, that these sample was not polished and embedded into an epoxy resin. For this reason, only the surface was examined, where high amounts of carbon as well as oxygen can be expected.

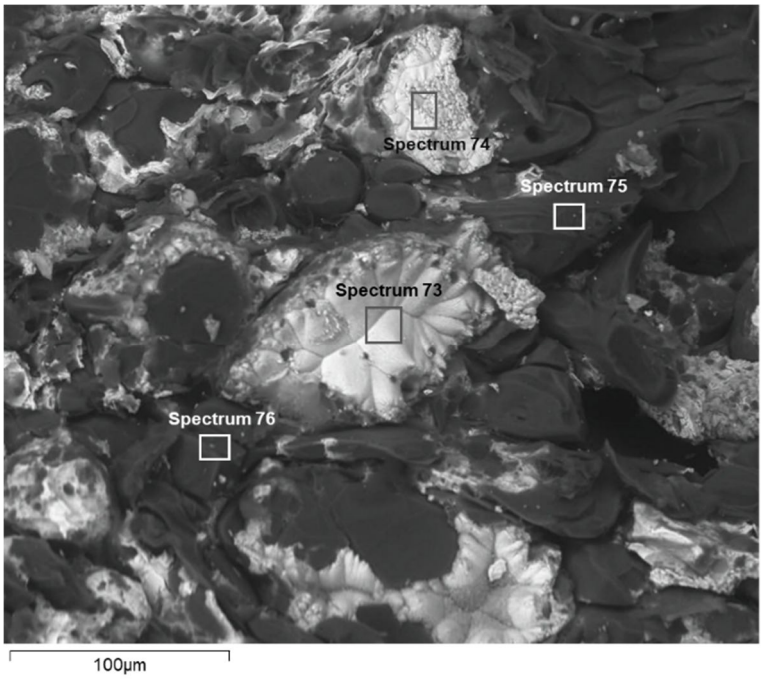

Figure 61: SEM-analysis image from the magnetic material of sample S4 after carbo-thermal treatment at 1873 K

Table 13: Elemental composition [m.-%] of characteristic spectra from SEM-analysis of sample S4 according to Figure 61 after carbo-thermal treatment at 1873 K

	Spectrum			
	73	**74**	**75**	**76**
Element	**Magnetic phase**		**Carbon-phase**	
C	40.1	38.1	93.5	92.5
O	18.0	23.9	-	-
Si	3.8	2.4	0.7	0.9
P	3.9	1.8	0.2	0.2
Fe	34.2	30.6	5.6	6.4
total	100.0	96.8	100.0	100.0

It can be concluded from the results of the SEM-analysis that only sample S5 could be reduced, resulting in the formation of metallic droplets. Furthermore, only a mineral phase, consisting of different slag phases, and no metallic-species could be found in the samples S1 – S3 as well as for S6. The results of the magnetic piece, deposed on the graphite underlayment shouldn't be paid too much attention, but it can be seen, that reduced iron-oxide could be identified, which will be supported by the up-coming analysis. However, ICP-OES for the same samples and additionally for the metallic chromium droplets are presented in the next sub-chapter.

4.1.3.3 ICP-OES analysis

In order to get an overview about the elemental composition of each recovered material after carbo-thermal treatment at 1873 K an ICP-OES analysis was performed. For the metal droplets of S5 only 0.19 g could be gained, and for this reason the whole amount was submitted to the ICP-OES. Thus, for this sample no further investigations with SEM could be carried out, which was already described in chapter 4.1.3.2. Excepted of the magnetic material from S4, which was 0.8 g, the analysis amount of all other samples was between 2 – 4 g. Based on the ICP-OES, the elements Ca, Si, Mg, Al, P, and Fe, Cr or Mn were determined and its composition is shown in Figure 62. Despite oxygen is already implemented into Figure 62, which was calculated, by assuming that the analysed elements are present as CaO, SiO_2, MgO, Al_2O_3, C_3P, FeO, Cr_2O_3, and MnO, the composition for all investigated samples deviates far from 100 m-%. Moreover, samples are highly concentrated with aluminium, which cannot be explained to this extent. Neither such high aluminium contents can stem from the crucible, which is made of 97.5% of MgO, nor from the jaw material of the jaw-crusher or other tools used for sampling. Additionally, very low amounts of calcium, and silicon were measured. By assuming that no metal-oxide such as that of iron, chromium or manganese could be reduced for S1 – S3 and for S6, these amounts are too low, particularly for S6. However, as already described beforehand, manganese could also be evaporated during high temperature treatment. The lack of knowledge about this mechanism and the omitted gas-phase investigation does not allow any further statements to be made at this point. There are also lower chromium amounts expected for the mineral phase of S5. Although 0.19 g of metallic chromium could be recovered, compared to the total expected amount of 2.55 g chromium, even higher chromium contents should be found in the mineral phase. For further experiments, the application of proper analysation method should be discussed.

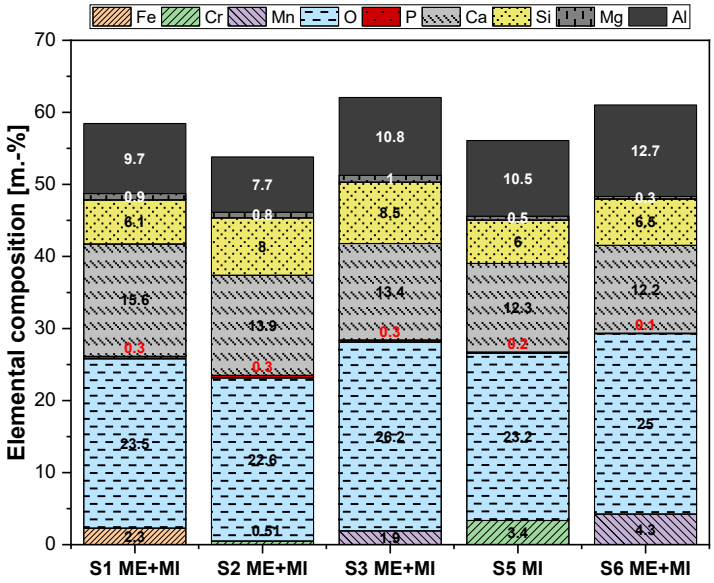

Figure 62: Elemental composition by ICP-OES of mineral samples after carbo-thermal treatment at 1873 K

The oxidic composition of each extracted mineral-phase is presented in Figure 63. For each expectable oxide species, the amount of oxygen was calculated. Again, the high Al_2O_3 is clearly visible. Instead, the ratio of iron-, chromium-, and manganese-oxides is too low. Taking into account that no phosphate reduction took place for S1 – S3, the C_3P amount is within a reasonable range. The low amounts of sample S5 could be the reason for reduction processes, while the lowest C_3P amount could be identified for S6.

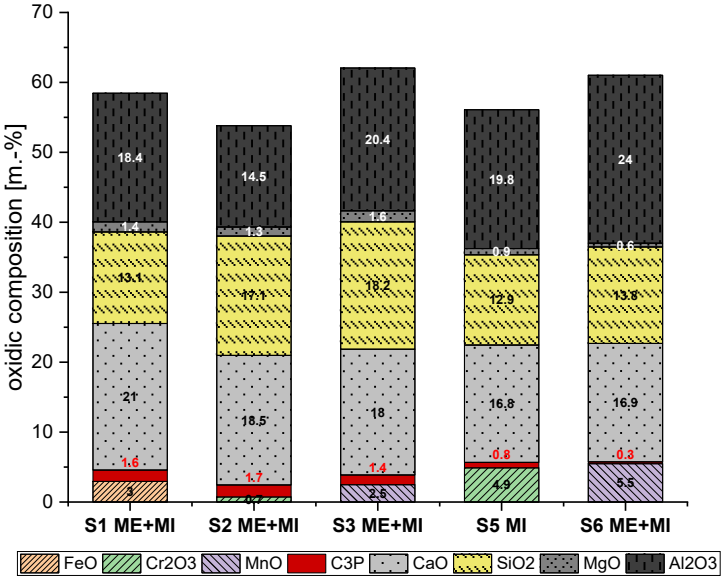

Figure 63: Composition of oxidic species of mineral samples after carbo-thermal treatment based on the ICP-OES results from Figure 62

The elemental composition by ICP-OES of the magnetic material from S4 and the metallic phase, manually separated from S5 is demonstrated in Figure 64. For both samples mainly iron, and chromium can be determined. Besides, little amounts of calcium and silicon are evidence for a metallic phase. The SEM-analysis of S4 has already revealed, that oxygen as well as high amounts of carbon can be measured at the particles surface, which could make up a part of the missing 34.6 m.-%. Too little amount of metallic chromium was left for further phase-analysis with the help of a SEM. Therefore, with the available results, it can't be argued, why the total amount of analysed elements sums up to only 40.8 m.-%. However, high amounts of phosphorus can be identified in S5, indicating the formation of phosphides. In comparison to S5, the phosphorus to metal ratio in S4 is distinctively lower. Finally, it needs to be considered, that S4 is not a representative sample.

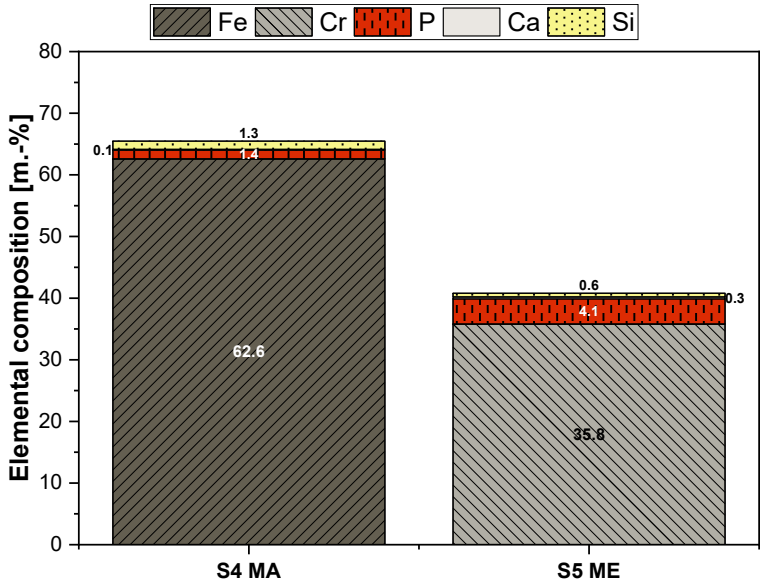

Figure 64: Elemental composition of the magnetic- and metallic-phase of S4 and S5 after carbo-thermal treatment by ICP-OES

The basicity B_2 was calculated after reduction experiment, which is summarised in Table 14.

Table 14: Calculated basicity B_2 of slags after reduction experiment based on results from Figure 63

S1 ME+MI	S2 ME+MI	S3 ME+MI	S4	S5 MI	S6 ME+MI
1.6	1.1	1.0	-	1.3	1.2

Both applied methods of analysation, ICP-OES and SEM are crucial for the identification of the composition of formed mineral-, or metal-phases. The former delivers information about the elemental composition, while the latter is performed to identify oxidic and metallic phases

within the sample. The degree of reduced metal (DRM), according to Equation 4-2 can unfortunately only be calculated reliably for sample S5.

$$DRM = \frac{metallic\ X\ [m.-\%]}{metallic\ X\ [m.-\%] + oxidic\ form\ of\ metal\ X\ [m.-\%]} \cdot 100\% \qquad \textbf{4-2}$$

By assuming that the initial sample mass before reduction was 15 g and 17 m.-% were chromium, which is 2.55 g and only 0.2 g could be extracted, a DRM of 5.2% can be determined. Minor amounts of metallic chromium droplets within the remaining mineral phase were neglected in this calculation.

5 Conclusion

This thesis aimed in fundamental research about the phosphide formation behaviour during slag processing. Specifically, proceeding reactions between highly reactive gaseous phosphorus and molten metals such as iron, chromium, or manganese, both products of carbo-thermal reduction, was examined. In sum one experimental series could be carried out. It consists of smelting synthetically produced slag samples, the investigation of their melting behaviour after reductant addition, and finally their carbo-thermal reduction at 1873 K. Slags with either lower (4 m.-%) or higher (17 m.-%) contents of iron, chromium, or manganese were prepared, covering a wide range of compositions. Overall, six samples were treated, whereby the separate formation of a metal- and a mineral-phase was expected. After that, the phosphorus distribution between those phases should be ascertained and from this a comparison should be made between each slag samples. Findings should identify which metals preferentially form phosphides under the given conditions. The future objective results in the definition of favoured mixtures, which should be treated with the aid of the InduRed reactor principle in the InduMelt. Then slag mixtures could be identified that maximize the yield of removed gaseous phosphorus during high temperature reduction, by simultaneously minimizing the accumulation of phosphides in the reduced metal product.

Due to technical obstacles with the elevator furnace this thesis deals with outcomes of only one experiment. However, more practical attempts at this field of research need to be conducted in the future. The results reveal the complexity, including the multi-component system slag to be treated and carbo-thermal reduction at elevated temperatures. Synthetic slags S1 – S3 representing low metal containing samples of iron, chromium, or manganese couldn’t be reduced at all. For each sample, a total amount of 15 g was treated. Compared to the relatively high proportion of slag-components, approximately 0.6 g of metal was possibly

too low. Therefore, a phosphorus partition for these samples couldn't be determined at all. The iron-rich sample S4 seems unsuitable for the crucible material: Sporadically but selective holes in the crucible bottom leads to the unwanted outflux of nearly the whole sample. Therefore, S4 was not available for further analysis. Only a small part of already leaked slag, showing magnetic properties could be isolated. Nevertheless, results from this sample should be interpreted cautiously. The only recovered metallic phase stem from S5, containing originally of 17 m.-% chromium. 0.2 g metallic chromium with noticeably higher amounts of phosphorus could be identified. The remaining mineral phase of S5 was poor in chromium and phosphorus, which indicates the accumulation of phosphides within the metal. Small traces of reduced metallic chromium within the mineral phase of diameters lower than 20 μm could be determined with a stereomicroscope. This particle size was too small for its recovery. For manganese, it seems that two different phases of slag formed during reduction: A dark manganese-rich lighter slag and a bright, heavier, highly porous calcium-silicate slag. Also, intense reactions between crucible and sample S6 could be recognized. However, also the phenomenon of manganese evaporation needs to be investigated in further experiments. At this point it can't be concluded if manganese could be reduced or not. Considering, that reduction took place, manganese could also be evaporated, leaving the sample into the gas phase. According to literature, the formation of manganese-phosphides occurs in the gaseous state. Low amounts of manganese and phosphorus were measured, which is why it could be an indication, that this mechanism occurred. In general, the analytical results obtained by ICP-OES occasionally show results that are difficult to interpret and elucidate. Hence, the approach for analytical methods should be discussed as well for further experiments.

For this reason, the results of the experiments, conducted in the course of this thesis, do not allow any conclusions to be drawn about the assumptions made at the beginning:

- **Higher amounts of iron, chromium, or manganese in the synthesised initial slag are expressed in a lower De-Phosphorisation coefficient L_P after carbo-thermal treatment at 1873 K: $L_P(Fe, Cr, Mn)_{high} < L_P(Fe, Cr, Mn)_{low}$:** No oxide of iron, chromium, or manganese could be reduced for samples S1 – S3 for several reasons. Therefore, at this point, no comparison with higher concentrated slags of iron, chromium, or manganese can be drawn.
- **Iron, and chromium show a stronger affinity to phosphorus, compared to that of manganese, which results in the following De-Phosphorisation coefficient sequence after carbo-thermal treatment at 1873 K: $L_P(Fe)$ and $L_P(Cr) < L_P(Mn)$**: More experiments with suitably selected parameters need to be carried out.

Furthermore, the emerging gas phase needs to be studied. According to the current state of knowledge, this assumption can neither be corroborated nor refuted.

- **The evaluation of the present slag samples concerning the relevant temperature range, chemical aspects, and thermodynamic considerations, implies that the following phosphides are most likely to be formed: Fe_2P, $Cr_{12}P_7$, and Mn_3P_2:** For the identification of phosphide species, the application of proper analytical methods should be paid more attention for further experiments. As well as for both other assumptions more outcomes of practical experiments need to be conducted, obtaining reliable results.

In summary, the experimental setup must be improved and adapted for future experiments, achieving reproducible and more meaningful results. These adjustments are represented in the research prospects of the last chapter 6.

6 Research prospect

The recycling of basic oxygen furnace slag could be provided by a pyrometallurgical treatment step with the aid of the introduced InduRed reactor concept. The formed phases are a preferably phosphorus-free metal-, and slag-product. Moreover, a heat value rich gas phase with high rates of gasified phosphorus compared to conventional slag treatment can be ensured. However, the mineral phase or slag as well as the formed gas phase were not examined in the course of this thesis. One of the main challenges for an internal re-use of the recycled metal-alloy within the steelworks is the affinity between valuable metals such as iron, chromium, and manganese as well as phosphorus. Thus, numerous efforts must be made in this field of research identifying influential parameters on the phosphide formation behaviour. In general, slags are highly complex multi-component systems, whereby a lot of different parameters need to be considered during carbo-thermal treatment which in turn is a process of highest complexity. For the experiment sequence in the course of this thesis a lot of characteristic values have to be determined including:

- Sample size and composition of the initial slag, which is crucial for the emerging mineral-, and metal-phase composition as well for their melting behaviour and viscosity
- Reductant type and amount
- Type of reduction mechanism
- Surrounding gas composition
- Process design
- Crucible setup and crucible material choice
- Heating up- and cooling down-rate
- Temperature conditions, i.e., maximum reduction temperature

- Uniform sampling and analysation methods of emerged phases

A lot of improvements should be implemented for further research efforts, guaranteeing the reproducibility of carbo-thermal reduction of such slags, gaining additional insights. Therefore, a standardized experimental scheme for the execution of follow-up experiments should be elaborated. This contains the production of synthetic iron-, chromium-, and manganese bearing slag-mixtures in a suitable concentration range. These mixtures should be reduced with fine carbon-powder in the elevator furnace to identify suitable ranges of slag composition, which in turn should be finally treated in the InduMelt. The goal is the maximisation of the PGD by simultaneously minimizing phosphorus accumulation in the resulting metal product and in the emerging slag phase. Deduced from the experiment, carried out in this thesis, upcoming experiments should include the following steps:

I. Simulation of potential slag mixtures including iron, chromium, or manganese amounts based on results of FactSage™. This could support the identification of potential slag mixtures. Furthermore, possible inconvenient slag compositions can be determined, which can be omitted for practical tests, representing a crucial time-saving step.
II. Production of an initial slag mixture with a certain basicity and slag composition based on the FactSage™ simulations by blending pure chemical powders of $CaCO_3$, SiO_2, C_3P, MgO, and Al_2O_3.
III. Smelting 1000 g of the initial slag in the InduMelt (B_2 = 1.0 – 1.2) at 1873 K in a MgO-crucible as basis material.
IV. Implementation of a harmonised procedure for slag extraction.
V. Analysing the slag composition by ICP-OES in combination with X-ray diffraction (XRD)/REM, identifying formed slag-phases.
VI. By the addition of the respective metal-oxide (Fe_3O_4, Cr_2O_3, or MnO_2) to the produced initial slag from the InduMelt, 50 g of a Fe-, Cr-, or Mn-containing slag sample can be obtained.
VII. Smelting of the final Fe-, Cr-, or Mn-containing slag sample (50 g) in the elevator furnace with characteristic metal-concentrations according to the results from FactSage™ at 1873 K in a MgO-crucible. Detailed considerations especially of low metal concentrated slags should include the determination of the melting point supported by a ternary system. Moreover, a minimum metallic amount needs to be defined, guaranteeing the formation of reduced metal droplets. Furthermore, a separation into a metal- and mineral-phase should be feasible.

VIII. Sample extraction after smelting in the elevator furnace, which should be also standardized. If more amount of material to be treated is used as in comparison to the experiment in this thesis, the bottom and cap could be cut-off with a diamond saw. Then, the slag could be gained easily with hammer and chisel, followed by grain-size adjustment, which should be identical for all samples. Therefore, with the help of a jaw-crusher a grain-size of preferably between 1 – 3 mm should be targeted, optimizing the gas distribution within the bulk during treatment.

IX. Analysis of the slag-composition after smelting in the elevator furnace by ICP-OES and XRD/REM to determine the phases of Fe-, Cr-, and Mn-species.

X. Carbon-addition, which is stoichiometrically calculated + excess carbon of 20%.

XI. Melting behaviour evaluation of the carbon-slag mixture in a heating microscope.

XII. Optical assessment of reduced mixtures after the heating microscope application. SEM-analysis for a first DRM estimation can be implemented.

XIII. Carbo-thermal reduction of the slag-carbon mixture in a graphite crucible at 1873 K under argon gas purging in the elevator furnace:

- The crucible is equipped with a cap, also made of graphite with a central hole, so that gaseous compounds can be removed via the flue.
- The application of a graphite crucible is a good replica of the surface of a piece of graphite, which is intended to represent the InduRed reactor principle even more closely. Thus, the huge contact area between MgO and sample is eliminated. Furthermore, graphite is resistant against thermal shock, which allows a wide range of options in terms of cooling- and heating-rates.
- Optional: Quenching the hot liquid samples in a water-bath after reaching the holding time at the maximum reduction temperature. This allows the reproduction of current up-to-date treatment of slags.

XIV. Harmonised procedure for sampling, including the separation into a mineral- and metal phase, whereas different approaches need to be considered between iron rich- and chromium/manganese-rich samples:

- Iron rich sample:
  - Are there cooled metal droplets recognizable? Yes – first rough manual separation supported with a magnet.
  - Mineral phase crushing in a jaw-crusher resulting in a further treatment with mortar and pestle. Subsequently, the remaining metal inside the powder should be magnetically separated.

- Cr- and Mn-rich sample:
  - Are there cooled metal droplets recognizable? Yes – first rough manual separation.
  - If the analysis reveals a size of recoverable metal droplets in the remaining mineral phase, these could be recovered via density separation.

XV. Analysis of metal- and mineral phase:
- ICP-OES/X-ray fluorescence analysis for elemental composition of metal- and mineral phase.
- REM/XRD for the metal phase, identifying phosphide-species.

XVI. Evaluation of different vital parameters:
- DRM of Fe, Cr, and Mn.
- Phosphorus partition between mineral phase and metal.
- Phosphide species identification within the metal product.

These experiments should identify differences between iron, chromium, and manganese in terms of the phosphide formation tendencies by considering each metal separately. However, a different behaviour can be expected if an alloy of iron-, chromium-, and manganese during carbo-thermal reduction is formed, which should be examined afterwards. Moreover, manganese evaporation experiments, conducted in the InduMelt plant should also be planned for further investigations.

As it can be seen, there is still a lot of knowledge to be gained about the carbo-thermal treatment of basic oxygen furnace slag. Outcomes of the experimental part in the course of this thesis enables a firm basis for follow-up experiments.

7 References

[1] Remus Rainer, Miguel A. Aguado-Monsonet, Serge Roudier, Luis Delgado Sancho. Best available techniques (BAT) reference document for iron and steel production: Industrial emissions directive 2010/75/EU (integrated pollution prevention and control). Luxembourg: Publications Office of the European Union; 2013.

[2] worldsteel Association. World Steel in Figures 2021. [October 06, 2021]; Available from: https://www.worldsteel.org/en/dam/jcr:976723ed-74b3-47b4-92f6-81b6a452b86e/World%2520Steel%2520in%2520Figures%25202021.pdf.

[3] worldsteel Association. Energy use in the steel industry. [December 04, 2021]; Available from: https://www.worldsteel.org/en/dam/jcr:b9199058-236a-408c-83fe-4d24a207fdf1/worldsteel%2520Energy%2520use%2520report_2014.pdf.

[4] worldsteel Association. Steel - the permanent material in the circular economy. [December 04, 2021]; Available from: https://www.worldsteel.org/en/dam/jcr:7e0dc90a-3efe-41bc-9fb4-85f9e873dfc7/Steel+-+The+Permanent+Material+in+the+Circular+Economy.pdf.

[5] Naidu TS, Sheridan CM, van Dyk LD. Basic oxygen furnace slag: Review of current and potential uses. Minerals Engineering 2020;149:106234.

[6] worldsteel Association. Steel industry co-products: Fact sheet. [December 04, 2021]; Available from: https://www.worldsteel.org/en/dam/jcr:1b916a6d-06fd-4e84-b35d-c1d911d18df4/Fact_By-products_2018.pdf.

[7] worldsteel Association. Steel industry co-products: Public policy paper. [December 04, 2021]; Available from: https://www.worldsteel.org/en/dam/jcr:3d1e2c1e-e306-4bac-a364-3672af7e30b9/Co%2520Products%25202020.pdf.

[8] Barui S, Mukherjee S, Srivastava A, Chattopadhyay K. Understanding Dephosphorization in Basic Oxygen Furnaces (BOFs) Using Data Driven Modeling Techniques. Metals 2019;9(9):955.

[9] Cappel J, Weinberg M, Urban W. Dephosphorization Strategies and Modeling in Oxygen Steelmaking 2014.

[10] Basu S. Studies on dephosphorisation during steelmaking. Doctoral Thesis. Stockholm; 2007.

[11] Chen Y-L, Lin C-T. Recycling of Basic Oxygen Furnace Slag as a Raw Material for Autoclaved Aerated Concrete Production. Sustainability 2020;12(15):5896.

[12] European Commission. Removal of Phosphorus from BOF-slag (PSP-BOF). Luxembourg; 2018.

[13] Christoph Ponak HR. Phosphorus removal and metal recovery from BOF-slags; Available from: https://www.k1-met.com/fileadmin/user_upload/Publications/Success_stories/2018SuccessStory_EN_RA_1.pdf.

[14] Christoph Ponak. Carbo-thermal reduction of basic oxygen furnace slags with simultaneous removal of phosphorus via the gas phase. Dissertation. Leoben; 2019.

[15] Blengini GA, El Latunussa C, Eynard U, Torres de Matos C, Wittmer DMAG, Georgitzikis K et al. Study on the EU's list of critical raw materials (2020): Final report. Luxembourg: Publications Office of the European Union; 2020.

[16] Draxler M, Schenk J, Bürgler T, Sormann A. The Steel Industry in the European Union on the Crossroad to Carbon Lean Production—Status, Initiatives and Challenges. Berg Huettenmaenn Monatsh 2020;165(5):221–6.

[17] worldsteel Association. Steel and raw materials. [December 04, 2021]; Available from: https://www.worldsteel.org/en/dam/jcr:16ad9bcd-dbf5-449f-b42c-b220952767bf/fact_raw+materials_2018.pdf.

[18] Yildirim IZ, Prezzi M. Chemical, Mineralogical, and Morphological Properties of Steel Slag. Advances in Civil Engineering 2011;2011:1–13.

[19] Juckes LM. The volume stability of modern steelmaking slags. Mineral Processing and Extractive Metallurgy 2003;112(3):177–97.

[20] Teir S, Eloneva S, Fogelholm C-J, Zevenhoven R. Dissolution of steelmaking slags in acetic acid for precipitated calcium carbonate production. Energy 2007;32(4):528–39.

[21] V. Kumar, S. Kumar, J. Prasad, K.K. Keshari, S. Ghosh and A. K. Bhakat. Feasibility Study of Dephosphorization of Slag generated from Basic Oxygen Furnace of an integrated Steel Plant. International Journal of Metallurgical Engineering 2017;6(2):31–5.

[22] Chaurand P, Rose J, Briois V, Olivi L, Hazemann J-L, Proux O et al. Environmental impacts of steel slag reused in road construction: a crystallographic and molecular (XANES) approach. Journal of hazardous materials 2007;139(3):537–42.

[23] Tuo Wu, Jintao Gao, Yanling Zhang, Fang Yuan. Thermodynamic prediction of chromium reduction behaviour from slag. 5th International Slag Valorisation Symposium (Leuven) 2017:165–8.

[24] Lecture 5: Physico-chemical properties of slag. [October 15, 2021]; Available from: https://nptel.ac.in/content/storage2/courses/113104059/lecture_pdf/Lecture%205.pdf.

[25] Schenk Johannes. Eisen- und Stahlmetallurgie I: Vorlesungsskriptum Sommersemester 2019. Leoben: Lehrstuhl für Eisen- und Stahlmetallurgie - Montanuniversität Leoben; 2019.

[26] Ajay Kumar Shukla, Brahma Deo. Mathematical Modeling of Phosphorus Prediction in BOF Steelmaking Process: A Fundamental Approach to Produce Low Phosphorus Steels and Ensure Direct Tap Practices. [October 05, 2021]; Available from: https://mme.iitm.ac.in/shukla/Poster%20Ajay%20Kumar%20Shukla.pdf.

[27] Surupa S. Pig Iron: Meaning and Impurities | Metals | Industries | Metallurgy. [October 16, 2021]; Available from: https://www.engineeringenotes.com/metallurgy/iron/pig-iron-meaning-and-impurities-metals-industries-metallurgy/20784.

[28] Kovtun O, Karbayev M, Korobeinikov I, Srishilan C, Shukla AK, Volkova O. Phosphorus Partition Between Liquid Crude Steel and High-Basicity Basic Oxygen Furnace Slags. steel research int. 2021;92(8):2000607.

[29] N. Assis A, A. Tayeb M, Sridhar S, J. Fruehan R. Phosphorus Equilibrium Between Liquid Iron and CaO-SiO2-MgO-Al2O3-FeO-P2O5 Slags: EAF Slags, the Effect of Alumina and New Correlation. Metals 2019 2019;9(2):116.

[30] Tabuchi, S., Sano, N. Thermodynamics of phosphate and phosphide in CaO-CaF2 melts. Metall Mater Trans B 15 1984:351–6.

[31] Ahindra Ghosh, Amit Chatterjee. Ironmaking and Steelmaking: Theory and Practice. New Dehli: PHI Learning Private Limited; 2008.

[32] Yüksel İ. A review of steel slag usage in construction industry for sustainable development. Environ Dev Sustain 2017;19(2):369–84.

[33] İ. Akın Altun, İsmail Yılmaz. Study on steel furnace slags with high MgO as additive in Portland cement. Cement and Concrete Research 2002(0008-8846):1247–9.

[34] EUROSLAG. Statistics 2016. [December 04, 2021]; Available from: https://www.euroslag.com/wp-content/uploads/2019/01/Statistics-2016.pdf.

[35] Liu C, Guo M, Pandelaers L, Blanpain B, Huang S, Wollants P. Metal Recovery from BOF Steel Slag by Carbo-thermic Reduction. Berg Huettenmaenn Monatsh 2017;162(7):258–62.

[36] Tossavainen M, Engstrom F, Yang Q, Menad N, Lidstrom Larsson M, Bjorkman B. Characteristics of steel slag under different cooling conditions. Waste management (New York, N.Y.) 2007;27(10):1335–44.

[37] M. Legret, P. Chaurand, A. Benard, Y. Capowiez, D. Deneele, J. Reynard et al. A multidisciplinary approach for the assessment of the environmental behaviour of Basic Oxygen Furnace slag used in road construction. EUROSLAG 2010 2010.

[38] Sun Y, Zhang Z, Liu L, Wang X. Heat Recovery from High Temperature Slags: A Review of Chemical Methods. Energies 2015;8(3):1917–35.

[39] Barati M, Esfahani S, Utigard TA. Energy recovery from high temperature slags. Energy 2011(36):5440–9.

[40] Bisio G. Energy recovery from molten slag and exploitation of the recovered energy. Energy;1997(22):501–9.

[41] Harald Raupenstrauch. Innovationsscheck Plus: Arbeitsbericht - ChemGran Schlackenveredelung. Montanuniversität Leoben 2015.

[42] Ruth Bialucha, Thomas Wetzel, Thomas Merkel. Verwendung von Stahlwerksschlacken in Landschaftsbaumaßnahmen und Lärmschutzparks: TK Verlag Karl Thomé-Kozmiensky; 2014.

[43] J. N. Murphy, T. R. Meadowcroft, P. V. Barr. Enhancement of the cementitious properties of steelmaking slag. Canadian Metallurgical Quarterly 1998:315–31.

[44] Mia Tossavainen, Eric Forssberg. Leaching behaviour of rock material and slag used in road construction - a mineralogical interpretation. Steel Research 2000:442–8.

[45] Plunkett ER. Handbook of Industrial Toxicology. Chemical Publishing Co. 1976:108–9.

[46] Roland Jöbstl. Anforderungen an die umweltfreundliche Entsorgung von Stahlwerksschlacken am Beispiel der LD-Schlacken: TK Verlag Karl Thomé-Kozmiensky; 2013.

[47] voestalpine AG. LD-Schlacke: Daten und Fakten. [December 04, 2021]; Available from: https://www.voestalpine.com/group/static/sites/group/.downloads/de/konzern/2013-weissbuch-ld-schlacke.pdf.

[48] Kostorz G. Phase transformations in materials. Weinheim, New York, Chichester: Wiley-VCH; 2001.

[49] Massachusetts Institute of Technology. Ellingham diagrams. [November 01, 2021]; Available from: https://web.mit.edu/2.813/www/readings/Ellingham_diagrams.pdf.

[50] Ho-Sang Sohn, Zhao-Ping Chen, Woo-Gwang Jung. Reduction kinetics of manganese oxide in basic oxygen furnace type slag. Steel Research 2000(71):145–52.

[51] M. Allibert, H. Gaye, J. Geiseler, D. Janke, B.J. Keene, D. Kirner, M. Kowalski, J. Lehmann, K.C. Mills, D. Neuschütz, R. Parra, C. Saint-Jours, J. Spencer, M. Susa, M. Tmar and E. Woermann. Slag Atlas: 2nd Edition. Düsseldorf: Verlag Stahleisen GmbH; 1995.

[52] Takayuki Futatsuka, Kiyoteru Shitogiden, Takahiro Miki, Tetsuya Nagasaka, Mitsutaka Hino. Dissolution Behavior of Nutrition Elements from Steelmaking Slag into Seawater. ISIJ International 2003;44(4):753–61.

[53] Jiang Diao, Bing Xie, Yonghong Wang, Xu Guo. Recovery of Phosphorus from Dephosphorization Slag Produced by Duplex High Phosphorus Hot Metal Refining. ISIJ International 2012;52(6):955–9.

[54] Liu C, Huang S, Wollants P, Blanpain B, Guo M. Valorization of BOF Steel Slag by Reduction and Phase Modification: Metal Recovery and Slag Valorization. Metall and Materi Trans B 2017;48(3):1602–12.

[55] Sung-Mo Jung, Young-Ju Do J-HC. Reduction behavior of BOF type slags by solid carbon. steel research international 2006;77(5).

[56] Windisch S, Ponak C, Mally V, Raupenstrauch H. Phosphorrückgewinnung aus Klärschlammaschen mit dem RecoPhos-Prozess. Österr Wasser- und Abfallw 2020;72(9-10):421–8.

[57] Christoph Ponak, Valentin Mally, Stefan Windisch, Alexandra Holzer, Harald Raupenstrauch. Phosphorus Gasification during the Reduction of basic Oxygen Furnace Slags in a Novel Reactor Concept. IAAM - VBRI Press 2020;11(7).

[58] Christoph Ponak, Stefan Windisch, Valentin Mally, Harald Raupenstrauch (eds.). Recovery of Manganese, Chromium, Iron and Phosphorus from Basic Oxygen Furnace Slags; 2019.

[59] Felix Robert Breuer M. Improvement of the Utilization Versatility of High Chromium, Manganese and Phosphorus Basic Oxygen Furnace Slags by Carbo-thermal Reduction. Master Thesis. Leoben; 2021.

[60] Distowski H, Hofmann T. Ullmann's Encyclopedia of Industrial Chemistry. 19th ed. Berlin: VCH:505; 1985.

[61] Schlesinger ME. The thermodynamic properties of phosphorus and solid binary phosphides. Chemical Reviews 2002;102(11):4267–301.

[62] Assis AN, Tayeb MA, Sridhar S, Fruehan RJ. Phosphorus Equilibrium Between Liquid Iron and CaO-SiO2-MgO-Al2O3-FeO-P2O5 Slag Part 1: Literature Review, Methodology, and BOF Slags. Metall and Materi Trans B 2015;46(5):2255–63.

[63] Li P, Zhang J. Retraction: A Prediction Model of Phosphorus Distribution between CaO–SiO2–MgO–FeO–Fe2O3–P2O5 Slags and Liquid Iron. ISIJ Int. 2014;54(4):756–65.

[64] Nakase K, Matsui A, Kikuchi N, Miki Y. Effect of Slag Composition on Phosphorus Separation from Steelmaking Slag by Reduction. ISIJ International 2017;57(7):1197–204.

[65] You Z. Critical Evaluation and Thermodynamic Modeling of High Alloy Fe-Mn-Al-Si-C-P; 2020.

[66] You Z, Jung I-H. Thermodynamic optimization of the Mn–P and Fe–Mn–P systems. Calphad 2021;72:102226.

[67] A. I. Zaitsev, Z. V. Dobrokhotova, A. D. Litvina and B. M. Mogutnov. Thermodynamic Properties and Phase Equilibria in the Fe-P System. J. CSFT 1995(91(4)):703–12.

[68] Shin DJ, Gao X, Ueda S, Kitamura S. Measurement of the Activity Coefficients of P and Mn in Carbon-Saturated Fe-P-Mn-C Alloy. Metall and Materi Trans B 2019;50(2):825–33.

[69] Do K-H, Nam H-S, Jang J-M, Kim D-S, Pak J-J. Thermodynamic Interaction between Chromium and Phosphorus in High Cr Containing Liquid Iron. ISIJ International 2017;57(8):1334–9.

[70] V. H. Schenck, E. Steinmetz, H. Gitizad. Die Phosphoraktivität im flüssigen Eisen und ihre Beeinflussung durch Nickel, Mangan und Chrom. Arch. Eisenhüttenwes 1968(39):597–602.

[71] K. Yamada EK. Mass spectrometric determination of Activities of Phosphorus in liquid Fe-P-Si, Al, Ti, V, Cr, Co, Ni, Nb and Mo-Alloys. Tetsu-to-Hagané 1979(65):273.

[72] Frohberg, Martin G., Elliott, John F., Hadrys, Helmut G. Beitrag zur Thermodynamik von Mehrstofflösungen am Beispiel homogener Eisen-Chrom-Phosphor-Kohlenstoff-Schmelzen. Archiv für das Eisenhüttenwesen 1968(39):585.

[73] Y. Kanzaki, F. Tsukihashi, N. Sano. The solubility of CaO.Cr2O3 in the CaO-CaF2 system associated with dephosphorization of Fe-Cr-C melts. Tetsu-to-Hagané 1994(80):13.

[74] TAKIGUCHI Shin-ichi SN. Phosphorus Distribution between Fe-Cr-C Melts and CaO Bearing Fluxes. Tetsu to hagane 1988(74):809.

[75] HARA T, TSUKIHASHI F, SANO N. Phosphorus Partition between Fe-Cr-C Melts and BaO-BaF2 Fluxes and the Activity of BaO. Tetsu to hagane 1990(76):352.

[76] A.I Zaitsev, N.E. Shelkova, A.D. Litvina, B.M. Mogutnov. Thermodynamic properties and phase equilibria in the Cr-P system. Journal of Phase Equilibria 1998(19):191–9.

[77] Zhu Y, Wu S, Wang X. Nano CaO grain characteristics and growth model under calcination. Chemical Engineering Journal 2011;175:512–8.

[78] Outotec, Research center Antti Roine. HSC Chemistry.

[79] Qu Y, Yang Y, Zou Z, Zeilstra C, Meijer K, Boom R. Thermal Decomposition Behaviour of Fine Iron Ore Particles. ISIJ Int. 2014;54(10):2196–205.

[80] P. Norby HF. Experiment title: Thermal decomposition of chromium (VI) oxide; high resolution in-situ powder diffraction studies of mixed valence chromium oxides; Available from: http://ftp.esrf.eu/pub/UserReports/21930_A.pdf.

[81] Alexander Vladimir Blagus. Carbothermal reduction of manganese oxides by coke and its blends with polymeric materials. Doctoral thesis. Sydney; 2013.

[82] Andreas Schönberg. Thermal stability of C3P. Leoben; 2022.

[83] Outotec. HSC Chemistry 7.1.

[84] F.W. Dorn H. Zur Reduktion von Calciumphosphat bei der Phosphor-Herstellung. Chemie Ingenieur Technik 1970;42 Jahrgang(19).

[85] Sun G, Li B, Guo H, Yang W, Li S, Guo J. Thermodynamic Study on Reduction of Iron Oxides by H2 + CO + CH4 + N2 Mixture at 900 °C. Energies 2020;13(19):5053.

[86] Mori T, Yang J, Kuwabara M. Mechanism of Carbothermic Reduction of Chromium Oxide. ISIJ Int. 2007;47(10):1387–93.

[87] Kazemi M, Du Sichen. Effect of Experimental Conditions on Cementite Formation During Reduction of Iron Ore Pellets. Metall and Materi Trans B 2016;47(6):3519–26.

[88] H. Sun, K. Mori, V. Sahajwalla, and R. D. Pehlke. Carbon solution in liquid iron and iron alloys. High Temperature Materials and Processes 1997;17(4):258–70.

[89] Kononov R, Ostrovski O, Ganguly S. Carbothermal Reduction of Manganese Oxide in Different Gas Atmospheres. Metall and Materi Trans B 2008;39(5):662–8.

[90] El-Geassy AA, Halim KSA, Bahgat M, Mousa EA, El-Shereafy EE, El-Tawil AA. Carbothermic reduction of Fe2O3/C compacts: comparative approach to kinetics and mechanism. Ironmaking & Steelmaking 2013;40(7):534–44.

[91] A. P. Luz, S. Ribeiro, V. G. Domiciano, M. A. M. Brito, V. C. Pandolfelli. Slag melting temperature and contact angle on high carbon containing refractory substrates. Ceramica 2011;57:140–9.

[92] Ko-ichiro Ohno, Masashi Kaimoto, Takayuki Maeda, Koki Nishioka, Masakata Shimizu. Effect of slag melting behaviour on metal-slag separation temperature in pwdery iron, slag and carbon mixture. ISIJ International 2011;51(8):1279–84.

[93] Wu W, Meng H, Liu L, Yuan T, Bai Y, Yan Z. Slag Melting Characteristic of Slag Forming and Slag Splashing for BOF Less Slag Smelting. J. Iron Steel Res. Int. 2012;19(7):20–5.

[94] GESTIS-Stoffdatenbank. Datenblatt Aceton; Available from: https://gestis.dguv.de/data?name=011230.

[95] Elliott R, Coley K, Mostaghel S, Barati M. Review of Manganese Processing for Production of TRIP/TWIP Steels, Part 1: Current Practice and Processing Fundamentals. JOM 2018;70(5):680–90.

[96] Takehiro D, Noriyoshi A, Kazuyuki O, Kazuhiro H, Takashi K. Attack on Magnesia Crucible by Molten Iron. Materials Transactions 1993;34(5):460–6.